

**SIMULATION AND DEVELOPMENT OF THE RADIAL
TIME PROJECTION CHAMBER FOR THE BONUS12
EXPERIMENT IN CLAS12**

by

Nathan M Dzbenksi
M.S. May 2016, Old Dominion University

A Dissertation Submitted to the Faculty of
Old Dominion University in Partial Fulfillment of the
Requirements for the Degree of

DOCTOR OF PHILOSOPHY

PHYSICS

OLD DOMINION UNIVERSITY
May 2020

Approved by:

Gail Dodge (Director)

Ian Balitsky (Member)

Balsa Terzic (Member)

Stefen Bultmann (Member)

Holly Gaff (Member)

ABSTRACT

SIMULATION AND DEVELOPMENT OF THE RADIAL TIME PROJECTION CHAMBER FOR THE BONUS12 EXPERIMENT IN CLAS12

Nathan M Dzbenksi
Old Dominion University, 2020
Director: Dr. Gail Dodge

TODO: To be updated later!

Copyright, 2020, by Nathan M Dzbenksi, All Rights Reserved.

ACKNOWLEDGEMENTS

TODO: Thanks to everyone...

TABLE OF CONTENTS

	Page
LIST OF TABLES	viii
LIST OF FIGURES	xii
Chapter	
toc	1
1. INTRODUCTION	1
1.1 QUANTUM PHYSICS AND THE STANDARD MODEL IN A NUT-SHELL	1
1.2 THE TROUBLE WITH UNDERSTANDING THE NUCLEON	4
1.3 SCATTERING EXPERIMENTS AND BONUS12	5
1.4 INCLUSIVE DEEP INELASTIC SCATTERING DATA ANALYSIS OF RUN GROUP A DATA	5
2. PHYSICS FORMALISM	7
2.1 NUCLEON STRUCTURE	7
2.2 ELECTRON-SCATTERING KINEMATICS	10
2.3 ELASTIC SCATTERING	14
2.4 RESONANCE REGION	18
2.5 DEEP INELASTIC SCATTERING	20
2.6 PARTONS AND BJORKEN-SCALING	21
2.7 NUCLEON STRUCTURE-FUNCTION RATIO F_N^2/F_P^2	24
2.8 MODELS AND PREDICTIONS	26
2.9 DIFFICULTIES IN EXTRACTING F_2^N/F_2^P FROM DEUTERIUM ..	29
2.10 SPECTATOR TAGGING	30
2.10.1 IMPULSE APPROXIMATION	32
2.10.2 MINIMIZING FINAL STATE INTERACTIONS	33
3. THE BONUS12 EXPERIMENT	36
3.1 CONTINUOUS ELECTRON BEAM ACCELERATOR FACILITY ..	36
3.2 CEBAF LARGE ACCEPTANCE SPECTROMETER	37
3.2.1 TORUS MAGNET	38
3.2.2 CHERENKOV COUNTERS	39
3.2.3 DRIFT CHAMBERS	40
3.2.4 FORWARD TIME OF FLIGHT	40
3.2.5 ELECTROMAGNETIC CALORIMETER	41
3.2.6 SOLENOID MAGNET	42
3.2.7 CENTRAL TIME OF FLIGHT	42
3.3 BONUS12 RTPC	42

3.3.1	COMPONENTS AND THEIR PURPOSE	43
3.3.2	BONUS12 RTPC DRIFT-GAS MONITORING SYSTEM	45
3.3.3	CONSTRUCTION AND INTEGRATION	47
4.	SIMULATION AND DEVELOPMENT	49
4.1	GEANT4 MONTE CARLO (GEMC)	49
4.2	GARFIELD++	50
4.3	BONUS12 RTPC SIMULATIONS	50
4.3.1	GEOMETRY & MATERIALS	51
4.3.2	EVENT GENERATOR	53
4.3.3	DRIFT ELECTRONS	55
4.3.4	GAS OPTIMIZATION	57
4.3.5	DRIFT EQUATIONS	61
4.4	DMS SIMULATIONS	63
4.4.1	GEOMETRY	63
4.4.2	ELECTRIC FIELD	65
4.4.3	DRIFT VELOCITY	67
5.	DATA ANALYSIS	69
5.1	CLAS12 OFFLINE SOFTWARE	69
5.2	CALIBRATION	71
5.3	FIDUCIAL CUTS	73
5.4	KINEMATIC CUTS	74
5.5	BINNING AND ACCEPTANCE	82
5.6	FARADAY CUP AND INTEGRATED LUMINOSITY	83
5.7	CROSS SECTION	86
6.	RESULTS	88
6.1	RGA CROSS SECTION	88
6.2	BONUS12	90
6.2.1	DMS	90
6.2.2	RTPC	93
APPENDICES		
VITA		100

LIST OF TABLES

Table	Page
I Lund file header	54
II Lund particles	55
III Summary of calibrations done for Run Group A.....	72
IV Summary of binning in x and y	83

LIST OF FIGURES

Figure	Page
1 The 17 fundamental particles of The Standard Model of Particle Physics.	2
2 The Feynman diagram of neutron decay.	9
3 Feynman diagram of an electron scattering from a proton.	12
4 Scattering process on a quasi-static differential cross section.	13
5 The contributions of higher order diagrams.	16
6 Feynman diagram of deep inelastic electron scattering from a proton.	20
7 The transition from inelastic scattering to deep inelastic scattering of a virtual photon and the quark within a nucleon.	22
8 Comparison of CJ15 PDFs $xf(x, Q^2)$ for different flavors ($f = u, d, \bar{d} + \bar{u}, \bar{d}\bar{u}, s$ and $g/10$) at a scale $Q^2 = 10 \text{ GeV}^2$, with 90% CL uncertainty bands. Note the combined logarithmic/linear scale along the x-axis.[1] . . .	25
9 Model dependence of F_2^n/F_2^p . [2]	27
10 Measured values of F_2^p vs Q^2 for different values of x . [1]	28
11 Variations of the F_2^A/F_2^D ratio from unity indicating various nuclear binding effects. [3][4]	29
12 Impulse approximation (a) and final state interaction diagrams (b).	31
13 (a) The Deep Inelastic Scattering ratio n_D^{FSI}/n_D with n_D^{FSI} and n_D , calculated <i>vs.</i> the momentum $p_s \equiv \mathbf{p}_s $ of the spectator nucleon emitted at different angles θ_s . The full lines correspond to the Q^2 - and z -dependent debris-nucleon effective cross section σ_{eff} , whereas the dashed lines correspond to a constant cross section $\sigma_{\text{eff}} = 20 \text{ mb}$. (b) The Deep Inelastic Scattering ratio n_D^{FSI}/n_D with n_D^{FSI} and n_D , calculated <i>vs.</i> the emission angle θ_s of the spectator, for different values of the spectator momentum. Calculations were performed at $Q^2 = 5 \text{ (GeV/c)}^2$ and $x = 0.2$ for the both graphs.	34
14 CEBAF upgraded for the 12 GeV era.	36
15 The CEBAF Large Acceptance Spectrometer at 12 GeV (CLAS12).	38

16	The High Threshold Cerenkov Counter.	39
17	Exploded view of a sector of the Electromagnetic Calorimeter (EC) for CLAS12. [5]	41
18	The Central Time of Flight Detector.	42
19	Cross section of the RTPC showing a proton traversing the detector with ionization electrons drifting toward the readout pad board.	43
20	Design of the RTPC with only one-quarter of the translation boards attached.	44
21	Design concept of the Drift-gas Monitoring System (DMS) for the BONuS12 Experiment.	45
22	Monitoring output of the DMS.	46
23	Assembly station for the RTPC.	47
24	BONuS12 RTPC geometry implemented in GEMC	52
25	CLAS12 Solenoid Field Map (V.Lagerquist)	56
26	Magnetic field strength versus z for values of r	57
27	Drift angle vs drift time for various gas mixtures	58
28	Diffusion in drift angle vs diffusion in drift time for various gas mixtures .	59
29	Drift time versus drift angle for He:CO ₂ using various potentials.	60
30	Plots of drift electron properties.	62
31	Parameters a and b for drift angle (a_ϕ and b_ϕ) and drift time (a_t and b_t). .	62
32	Simulations of electric field within the DMS. In the profile plots in (b) and (c), the cathode and anode's locations are denoted as blue and red lines respectively. The sources and PMT's location and subsequent electron beams are pictured as green dotted lines.	66
33	Simulations electric field profile within the sensitive region of the DMS with various electrode diameters and distances.	66
34	Simulated drift time for electrons beginning at both the near and far sources from the anode.	67

35	1D distributions of the U, V, and W sectors of the PCAL. The uncut histograms are on the top and the bottom histograms contain the cuts: $U < 30$ cm, $30 < V < 390$ cm, and $30 < W < 390$ cm. All plots are normalized to account for any mismatch in total statistics. Red lines are from RGA data and black lines are for the Monte-Carlo (MC) data.	73
36	2D histograms of the uncut PCAL hits on the left and the 2D histogram containing the fiducial cuts.	74
37	v_z before and after all described cuts. Red lines are from RGA data and black lines are for the Monte-Carlo (MC) data.	75
38	Slicing and fitting of the sampling fraction to create a 5σ cut.	75
39	Kinematics variables before cuts. Red lines are from RGA data and black lines are for the Monte-Carlo (MC) data.	77
40	Kinematics variables after all described cuts. Red lines are from RGA data and black lines are for the Monte-Carlo (MC) data.	77
41	E' and EC energies before cuts. Red lines are from RGA data and black lines are for the Monte-Carlo (MC) data.	78
42	E' and EC energies after all described cuts. Red lines are from RGA data and black lines are for the Monte-Carlo (MC) data.	78
43	E' vs. θ and W vs. x_B before cuts.	79
44	E' vs. θ and W vs. x_B after all described cuts.	79
45	Q^2 vs. W and Q^2 vs x_B before cuts.	80
46	Q^2 vs. W and Q^2 vs x_B after all described cuts.	80
47	$E_{EC_{tot}}$ vs E_{PCAL} and Sampling fraction before cuts.	81
48	$E_{EC_{tot}}$ vs E_{PCAL} and Sampling fraction after all described cuts.	81
49	Binning in the x, y space.	82
50	83
51	84
52	84
53	Accumulated charge vs. file for Run 5036.	85

56	Plots of inclusive DIS differential cross section vs x_B for various values of y	87
59	Graph of the ratio of the differential cross section ratio for RGA data over Model data vs x_B for various values of y	89
60	DMS drift time histograms for CH1 (left) and CH2 (right) on Run 11953.	91
61	DMS drift velocity vs. time graph during Run 11953.	91
62	DMS drift velocity for channel 1 vs. run.	92
63	DMS drift velocity for channel 2 vs. run.	92
64	DMS gas pressure vs. run.	93
65	DMS drift velocity over all RGF runs.	93
66	Two examples of reconstructed hits in an event in the RTPC using Version 27 of the reconstruction software in an Cartesian x, y space for Run 11637 (a 2.14 GeV run). [<i>Courtesy D. Payette.</i>]	94
67	Two examples of reconstructed hits in an event in the RTPC using Version 26 of the reconstruction software in an Cartesian x, y space for Run 12240 (a 10.4 GeV run). [<i>Courtesy D. Payette.</i>]	94
68	The time shift (t_{shift}), momentum, and theta (θ) of the reconstructed protons in Run 11637.	95
69	On the left: 2D distributions of the calculated momentum (“mom_predicted” in the plot) on the x -axis and reconstructed momentum (“mom_measured” in the plot) for protons on the y -axis in Run 11637. On the right: The difference between the predicted and measured values of the momentum for Run 11637.	96
70	On the left: 2D distributions of the calculated theta (“theta_predicted” in the plot) on the x -axis and reconstructed theta (“theta_measured” in the plot) for protons on the y -axis in Run 11637. On the right: The difference between the predicted and measured values of theta for Run 11637.	97

CHAPTER 1

INTRODUCTION

Throughout human history we have been driven to understand the world around us. It is surely one of the characteristics that defines us as a species. Coupling that curiosity with our ability to create and construct incredible machines has allowed us to probe some of the most elusive parts of our Universe. From the Hubble Telescope taking images of the earliest moments of our Universe to the Large Hadron Collider probing the most fundamental particles that we currently know, we have been wildly successful at fulfilling that drive to understand.

Despite that success, there are many issues that continue to elude us. We currently have no tangible explanation for the asymmetry between matter and anti-matter. In the very early Universe there were equal amounts of matter and anti-matter, yet today our visible Universe seems to be comprised primarily of matter and not anti-matter. Another puzzle is that of dark matter and dark energy, which are collectively believed to make up 96% of our Universe, are phenomena we know almost nothing about. Even the matter that we do know about, we know surprisingly little about its structure and composition.

Atoms make up much of that visible Universe. Since the early 1900's we have known these atoms to be made of protons, neutrons and electrons. The discovery of protons and electrons essentially occurred in the late 19th Century, but the neutron was not discovered until 1932 by Sir James Chadwick. The neutron was not just found later than the electron and proton, we also know much less about it. The electron is well-known in the physics community to be a near point-like particle made of no constituent particles, but the proton and neutron have been proven to be made of more fundamental particles.

1.1 QUANTUM PHYSICS AND THE STANDARD MODEL IN A NUTSHELL

Knowing exactly what makes up these protons and neutrons relies on knowledge of the Standard Model of Particle Physics, sometimes referred to as just the Standard Model. This model, developed in stages throughout the latter half of the 20th

Century, essentially lays out the existence of all possible fundamental¹ particles in the Universe.

There are 17 particles in the Standard Model (outlined in Fig. 1). These 17 can first be broken down into two subgroups called bosons and fermions. Bosons follow what is known as Bose-Einstein statistics, which essentially states that they can occupy the same space at the same time. In the language of quantum physics, two bosons can be described by the same quantum numbers. These bosons, with a slight exception for the Higgs boson, are all considered force carriers. Photons are the force carriers for the electromagnetic force. Gluons carry the strong force. W and Z bosons are the force carriers for the weak force. The Higgs boson is a bit different in that it is not necessarily a force carrier. Its existence is tied to the breaking of electroweak symmetry² and it gives fermions their mass.

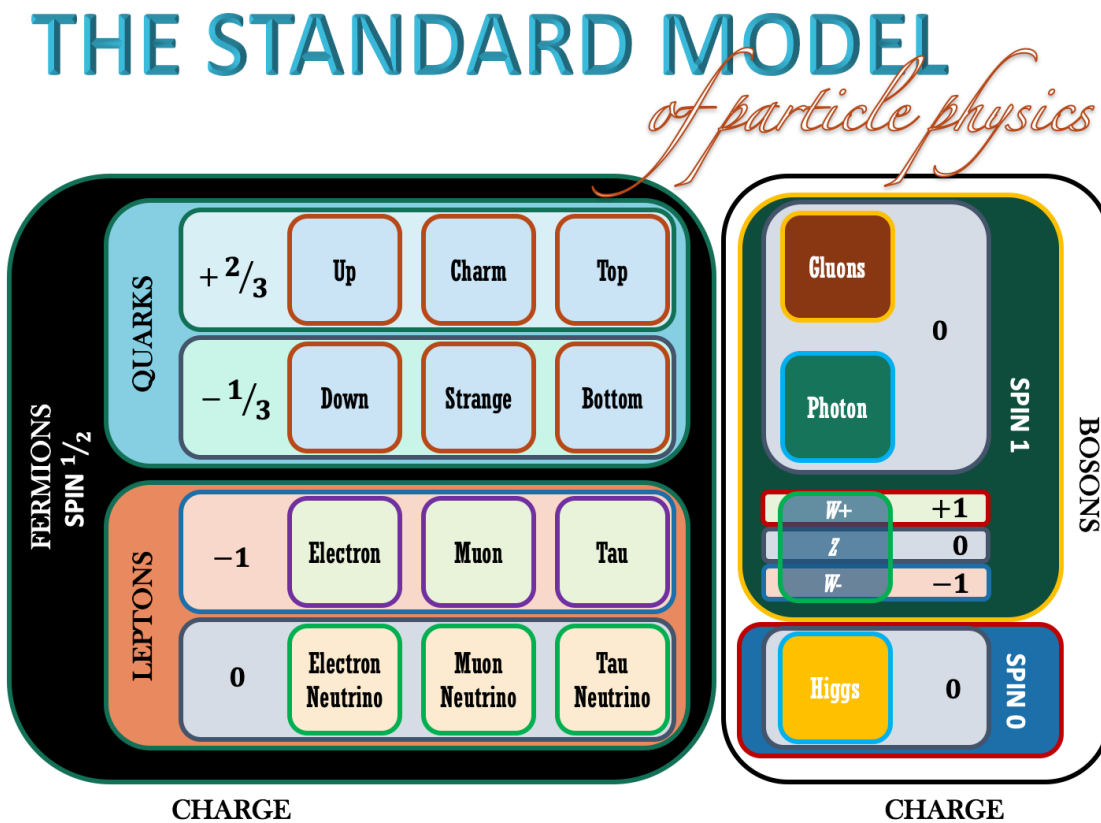


Fig. 1: The 17 fundamental particles of The Standard Model of Particle Physics.

¹The word “fundamental” here means that they are not made of constituent particles.

²In the early Universe, the electromagnetic and weak forces were one force. As the Universe began to cool, the symmetry that kept these two forces together broke. The Higgs boson essentially facilitated that breaking.

The other subgroup is fermions, which are 12 particles³ that obey a Fermi-Dirac statistical rule called the Pauli Exclusion Principle. Developed by Enrico Fermi, Paul Dirac and Wolfgang Pauli, this rule states that fermions cannot occupy the same place at the same time. Again in quantum physics language, no two fermions can be described by the same quantum numbers. There are two types of fermions in the Standard Model: 6 quarks and 6 leptons. Leptons, which include electrons, pions, tau and their associated neutrinos, cannot combine together alone to make larger structures. Quarks, on the other hand, do combine to make larger structures, like protons, neutrons, atoms, molecules, people and light posts (obviously with the contribution of some leptons). Quarks also obey the exclusion principle, which is why - with the Coulomb repulsion of atomic electrons - walking into a light post hurts. You both cannot be in the same place at the same time.

Quantum numbers, the characteristics that help define the differences between fermions and bosons, are what describe a quantum system. More precisely, quantum numbers are the eigenvalues of operators that commute with the Hamiltonian. These quantum numbers can describe quantities like angular momentum, spin or parity. The namesake to these numbers and this entire field of physics comes from the fact that these quantities exist in discrete steps (*e.g.* integer or half-integer steps), and are thus quantized.

One of those quantized observables is called spin. Because these fundamental particles are so incredibly small, they are considered point-like. Therefore many of these quantum numbers are simply mathematical constructs that tend to correspond to something physical we are familiar with. The spin quantum number is no exception. Fundamental fermions, as seen in Fig. 1, have spin 1/2, while fundamental bosons have integer spin of 0 or 1. Two, three or more quarks combine by way of gluons (*i.e.* the strong force). Two quarks combine to make particles called mesons⁴ (*e.g.* pions and kaons) and their spin states combine to form an overall integer 0 or 1, which also makes them bosons. Three quarks combine to make particles called baryons⁵ (*e.g.* protons and neutrons), which have spin 1/2 or 3/2 making them fermions as well. The collective group of quarks, mesons, and baryons are known as hadrons⁶.

³Each of these fermions also has an associated anti-particle, which has the same mass but opposite electric charge. For example, an anti-electron (known as a positron) also has a mass of 0.511 MeV/ c^2 but a charge of +1.

⁴The word meson comes from the Greek word μεσοσ (“mesos”) meaning medium.

⁵Baryon comes from the a Greek word βαρυσ (“varys”) meaning heavy.

⁶Hadron comes from the Greek word αδροσ (“adros”) meaning massive or large. Point-like quarks

Charge is another important quantized observable. When three quarks combine to make something like a proton or neutron, their charges also combine. A proton, for example, is made of two up quarks⁷ (each with charge $+2/3$) and a down quark (charge $-1/3$), so its overall charge is $+1$. A neutron is made of two down quarks and an up quark, so its charge is zero.

1.2 THE TROUBLE WITH UNDERSTANDING THE NUCLEON

Protons and neutrons make up the nucleus of an atom so they are called nucleons. These nucleons are not just made of three stationary quarks, but are very dynamic and busy particles. These three quarks that define whether it is a proton or neutron are called valence quarks. However, there are also quark-antiquark pairs that are in a constant state of creation and annihilation, called sea quarks. Then there are gluons which are carriers of the strong force binding quarks together. All of these particles have momenta and collectively define the structure of the nucleon. One issue in particle physics has been defining this structure, including the size of these nucleons and the momentum distribution of those fundamental particles that exist within it.

There has been a lot of effort exploring the structure and momentum distribution of the proton, yet there are some major puzzles that still exist. One of the most famous has to do with the proton spin called the “proton spin crisis.” This crisis refers to our collective inability to explain how all of the particles that exist in the proton conspire together to always give the proton spin $1/2$. Less famous puzzles include knowing the proton radius, where its mass comes from, and what the momentum distribution is of its fundamental constituent particles.

All of these puzzles also exist for the neutron, except with even less understanding. Whereas protons are easily confined to form targets for experiments, neutrons are not. Free neutrons decay in about 15 minutes, and because they do not have electric charge, cannot be easily confined. One new experiment that will be performed to confirm or reject theories related to the structure of the neutron and the momentum distribution of its constituents, is called the Barely Off-shell Nucleon Structure Experiment at 12 Giga-electron Volts (or BONuS12).

can combine to make a particles much heavier than the combined quarks themselves.

⁷Quark names are essentially meaningless. There is no physical characteristics that warrant a quark being called up or strange. They were simply given a name that stuck.

1.3 SCATTERING EXPERIMENTS AND BONUS12

In order to probe the enigmas of particles that are on the order of 50 trillion times smaller than a grain of sand, particle and nuclear physicists often use scattering experiments. These experiments accelerate particles to known energies and collide them with a target. The collision of accelerated particles on a target causes them both to scatter and, in some cases, fragment. The scattered particles resulting from the collision then enter particle detectors where information like energy, position, momentum, and time are gathered by exploiting various physics processes. With this information physicists can extract information related to the structure of nucleon or the momentum distribution of the fundamental constituents within it.

The Thomas Jefferson National Accelerator Lab (JLab) in Newport News, Virginia, contains an electron accelerator used for scattering experiments meant to explore nuclear and subatomic matter. Here is where, in 2005, the first BONuS Experiment ran in JLab's Experimental Hall B. The goal of that experiment was to explore the structure of the neutron by investigating the momentum distribution of the quarks and gluons inside. The results of the experiment made progress in reducing uncertainties in the quantities that describe neutron structure, which helped to begin confirming or denying some theories that exist attempting to describe these characteristics.

Jefferson Lab, in 2012, began an energy upgrade to bring the electron beam energy to 12 GeV, and with that came the development of an upgraded BONuS Experiment (called BONuS12). Just like the BONuS6 Experiment (*i.e.* the original BONuS Experiment that ran at 6 GeV), it is designed to explore a larger range in the momentum distribution of its fundamental constituent particles. Changes were made to improve the overall coverage of the detector.

1.4 INCLUSIVE DEEP INELASTIC SCATTERING DATA ANALYSIS OF RUN GROUP A DATA

Throughout the rest of this work we will primarily discuss BONuS12, the physics necessary to understand its goals and operation, and the efforts made to make the BONuS12 experiment operational before its Spring 2020 run. As a part of that BONuS12 development comes the need to confirm that data coming in from Hall B experiments at JLab make sense and is calibrated correctly.

While the BONuS12 RTPC will detect scattered protons, the scattered electron

will enter the existing detectors in Hall B, so understanding that electron data is important. For that, a portion of this work will be dedicated to analyzing data from one of the first experiments that ran after the start of the 12 GeV physics era at JLab (*i.e.* Run Group A). The process known as inclusive deep inelastic scattering will be examined since we know much about it. The word *inclusive* means that in the scattering of an electron off a nucleon or atom, we detect and analyze only the the electron, which includes all possible particles created in the process. In particular, we will look at what is known as the cross section of the process from the data and compare it to simulations that use well known values of that cross section. This will expand our understanding This will hopefully provide evidence that the detectors within Experimental Hall B, where the BONuS12 Experiment will run, are working effectively and are calibrated correctly.

CHAPTER 2

PHYSICS FORMALISM

The idea that matter is made of elementary particles has been around since about the 6th Century B.C.E., but it was not until 2400 years later in 1808 [6] that the first publication came out by John Dalton describing small particles called atoms. Between 1879 [7] and 1897 [8] works that discovered the existence of electrons started to be published and taken seriously. By 1914, Rutherford [9] and others established that there was a dense structure at the center of atoms that had a positive charge surrounded by the lighter-mass electrons on the outside. In 1913, the positively charged *nucleus* of the hydrogen atom was confirmed by Rutherford [10], which he named *proton*. It was not until 1932 that James Chadwick discovered the neutron.

Alongside the discoveries of these subatomic particles was the development of theories explaining their behavior. Electrons began to be understood as both a particle and a wave, depending on which way you try to observe it. Then it was realized all particles can act this way. Max Plank developed the idea that energy radiated from atomic systems did so only in discrete quantities or *quanta*. In 1905, Einstein [11] proclaimed that light is made of particles called photons, which was consistent with Plank's *quantum* hypothesis. Throughout the early 1900's this concept of quantum mechanics was developed.

In this journey through understanding the quantum world came the realization that the four fundamental forces in nature (*i.e.* gravity, electromagnetic, strong and weak nuclear) are fields that interact with quantum particles, which were also considered fields. For the electromagnetic force, this became known as quantum electrodynamics (QED) developed around the 1950-1960's. The interactions of particles with the strong nuclear force were described by a theory called quantum chromodynamics (QCD) developed around the late 1970's. This chapter will, in effect, follow this history with a slant toward its relevance in the BONuS12 Experiment.

2.1 NUCLEON STRUCTURE

The proton and neutron are the two components that make up a group called nucleons since they make up the nucleus of an atom. They both interact through

all four forces (*i.e.* strong nuclear, weak nuclear, electromagnetic, and gravitational). As mentioned in the Introduction, they are both fermions. Because they are both made up of three quarks, they are also both baryons.

The quarks that make up these nucleons (all baryons, in fact) and that are responsible for the nucleon's quantum numbers are called *valence quarks*. The proton is made of two *up* valence quarks and one *down* valence quark, denoted by *uud*. The neutron is made up of two down valence quarks and an up valence quark, or *udd*. Of course, there are also *sea quarks* made of $q\bar{q}$ pairs, where $q\bar{q}$ is any variety of quark-antiquark pair. However, the strong interaction which binds all of these quarks together acts the same no matter the quark flavor.¹ Therefore, the quark model does not predict any distinctions between protons and neutrons. In fact, from the view of the strong force, they are the identical particle in different states.² Yet, protons and neutrons are clearly not identical particles.

There are obvious differences between the two nucleons. One important difference between nucleons is their stability when not bound to each other. The proton is a stable particle on its own, with a lifetime of more than 2.1×10^{29} years. The neutron, however, has a lifetime of about 882 seconds (or about 15 minutes). The proton is the only nucleon that can exist in a nucleus on its own, such as in the hydrogen atom. The obvious difference in the two nucleons is their electric charge. The charge of the proton is +1 in units of electron charge, while the neutron is neutral (*i.e.* charge = 0). This charge arises from their valence quark content. The up quark has a charge equal to $q_u = +2/3$ and the down quark has a charge of $q_d = -1/3$, so for the proton with *uud* quarks,

$$2q_u + q_d = 2(+2/3) + (-1/3) = +1, \quad (1)$$

and for the neutron with *ddu* quarks,

$$2q_d + q_u = 2(-1/3) + (+2/3) = 0. \quad (2)$$

¹The word *flavor* is used to describe a type of quark. Remember there are 6 *flavors* of quarks: up, down, top, bottom, strange, and charm.

²There is a symmetry of the strong interaction in neutrons and protons called isospin (also referred to as isotopic or isobaric spin). Isospin is a dimensionless quantity that does not describe a physical “spin” of the particle. It does, however, offer a description of the two different states of nucleons. In particular, the projection of isospin along the z-axis (I_z or I_3) provides insight into the difference between protons and neutrons, which are otherwise almost identical particles. Protons have $I_z = 1/2$ and neutrons have $I_z = -1/2$.

The spatial charge distribution of quarks is well known for both nucleons. The momentum distribution of those quarks inside the nucleon is not as well known, especially for the neutron. The same is true for the overall structure of the nucleons, again more so for the neutron.

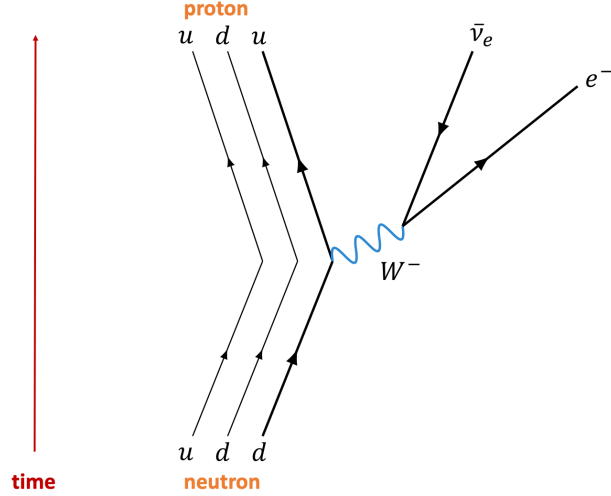


Fig. 2: The Feynman diagram of neutron decay.

The discrepancy of knowledge between the proton and the neutron is the last major difference of the nucleons we will discuss here, because it goes directly toward the principle goal of the BONuS12 Experiment. We know much more about the structure of the proton and momentum distribution of the quarks inside the proton for the reason discussed in the last paragraph. That is, protons can exist outside of nuclei while neutrons soon decay via the weak interaction

$$n \longrightarrow p + e^- + \bar{\nu}_e, \quad (3)$$

as seen in Fig. 2 as a Feynman diagram. Feynman diagrams were developed by physicist Richard Feynman to display particle interactions that occur in a relatively simplistic manner. Moving from the bottom to the top in the diagram of Fig. 2, we see a down quark within the neutron change states to an up quark mediated by the W^- boson, which then decays to an electron (e^-) and electron antineutrino ($\bar{\nu}_e$). This neutron decay occurs in 15 minutes. That decay coupled with the fact that the neutron has no electric charge makes isolating neutrons to create a target for scattering experiments extremely difficult. Yet, scattering experiments are the primary means by which physicists study the structure of particles. Therefore, studying

the structure of the neutron is inherently made difficult by this lack of free neutron target.

2.2 ELECTRON-SCATTERING KINEMATICS

To study the structure and physics of particles, nuclear and particle physicists use scattering experiments. There are two ways of creating a scattering experiment. One way is to accelerate a light particle (an electron, for example) and direct it toward a stationary target, which is the method used at Jefferson Lab in Newport News, Virginia. The other way is to accelerate two particles in opposite directions and then direct the two toward each other, which is the method used at the Large Hadron Collider (LHC) at CERN in Geneva, Switzerland. The physics or kinematics³ of both scattering experiments is essentially the same.

When the scattering particle and target collide, some of the momentum and energy of the scattering particle is transferred to that target particle. Nuclear and particle physicists express that energy and momentum as a four-momentum. Classical momentum is a vector, which means it has a magnitude and direction. That direction is typically expressed in three dimensions (for the familiar Cartesian coordinate system that would be along the x, y, and z-axis). Therefore a momentum can be expressed as $\mathbf{p} = (p_x, p_y, p_z)$, where \mathbf{p} is the momentum vector bold-faced to indicate that it is a vector. Because in particle physics, the particles travel close to the speed of light, we have to deal with special relativity. For the purposes of this work, special relativity essentially forces us to consider not just three-dimensional space, but four dimensional space-time with different reference frames for any non-accelerating moving objects. This drives us to require there be a four-dimensional space-time momentum $p = (p_0, p_1, p_2, p_3)$, where $p_1 = p_x$, $p_2 = p_y$, and $p_3 = p_z$ in Cartesian coordinates. The new term p_0 is equal to E/c , where E is the energy of the particle and c is the speed of light.

If we take this four-momentum

$$p_\mu = \left(\frac{E}{c}, p_x, p_y, p_z \right), \quad (4)$$

³The word kinematics refers to the mechanics of the particles without concern for the forces that caused the motion. Essentially, we are not concerned with *how* the particles were accelerated, just that they have a particular energy at the time of collision.

where μ is just an index indicating a particular particle, and square it, we have

$$p^\mu p_\mu = -\frac{E^2}{c^2} + p_x^2 + p_y^2 + p_z^2 = -\frac{E^2}{c^2} + \mathbf{p}^2. \quad (5)$$

This quantity is invariant under a Lorentz transformation (meaning it remains the same no matter the non-accelerating reference frame) and is equal to the Lorentz scalar $-m^2 c^2$, which means

$$-\frac{E^2}{c^2} + p^2 = -m^2 c^2. \quad (6)$$

Multiplying both sides of Eq. 6 by $-c^2$ and rearranging a little gives us

$$E^2 = p^2 c^2 + m^2 c^4, \quad (7)$$

which if we take the square root of both sides results in

$$E = \sqrt{(pc)^2 + (mc^2)^2}. \quad (8)$$

In the rest frame of the particle (*i.e.* the frame where the particle is considered to have no momentum, thus $p = 0$), this equation reduces to something that should be familiar:

$$E = mc^2. \quad (9)$$

This rough derivation provides a little insight to the power and purpose of using four-momentum. We will use this notation extensively throughout the rest of this work.

The other useful notation to understand is called natural units, where $c = \hbar = 1$. Under these units, Eq. 7 becomes

$$E^2 = p^2 + m^2. \quad (10)$$

While this offers much in the way of simplicity when working with complex equations, the disadvantage is that we lose information regarding dimensional analysis of the equation. Nevertheless, for the most part, we will use natural units in this work.

Consider an electron with four-momentum k scattering off of a nucleon with momentum p . The Feynman diagram for such an interaction is in Fig. 3, where k' and p' are the final momentum of the scattered electron and nucleon respectively. Here, q is the momentum of the virtual photon⁴ (typically denoted by γ^*) that mediates

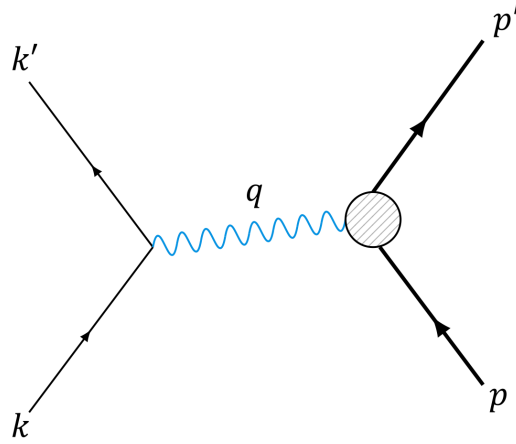


Fig. 3: Feynman diagram of an electron scattering from a proton.

the interaction. That virtual photon momentum, $q = k' - k$, is the momentum lost by the scattered electron.

There are some other important quantities to consider for electron scattering. The first is the square of that four-momentum transfer

$$q^2 = (k' - k)^2 = 2m_e^2 - 2(EE' - |\mathbf{p}||\mathbf{p}'| \cos \theta), \quad (11)$$

where m_e is the mass of the electron, E is the energy of the incident electron, E' is the energy of the scattered electron, $|\mathbf{p}|$ is the magnitude of the three-momentum of the incident nucleon, $|\mathbf{p}'|$ is the magnitude of the scattered nucleon's three-momentum, and θ is the scattering angle of the electron. When we use the trigonometric identity $1 - \cos \theta = 2 \sin^2 \frac{\theta}{2}$ and take the electron mass to be zero (*i.e.* $|p| = E$), we get

$$q^2 \approx -4EE' \sin^2 \frac{\theta}{2}. \quad (12)$$

As a convention to make the quantity positive, we use $Q^2 = -q^2$, which will be used throughout the rest of this work. Another variable we need in order to analyze these electron scattering kinematics is the variable ν , which is the energy transfer of the electron to the nucleon via γ^* (*i.e.* the virtual photon) and is defined by

$$\nu = \frac{\mathbf{p} \cdot \mathbf{q}}{M}. \quad (13)$$

⁴The term “virtual” here may be misleading. It does not imply that the photon does not really exist. It refers to the short-lived exchange of the electromagnetic force.

Here, p is the four-momentum of the incident nucleon and M is the nucleon mass. In the laboratory frame, the nucleon is at rest (*i.e.* $p = (M, \mathbf{0})$)⁵, and $q = (E - E', \mathbf{q})$, so the energy transferred by the virtual photon to the nucleon in the laboratory frame would be

$$\nu = E - E'. \quad (14)$$

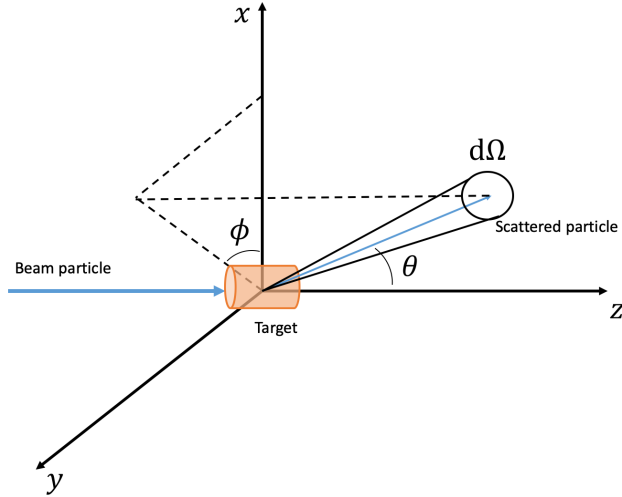


Fig. 4: Scattering process on a quasi-static differential cross section.

Whenever we deal with collisions of particles, there is a probability associated with the reaction between that projectile and target depicted in Fig. 4. That probability is called the *cross section* and with it often comes a wealth of knowledge about the dynamics of the interaction itself. In many reactions we deal with what is known as the *differential cross section*, which reflects the fact that the probability of a reaction depends on the spatial or kinematic quantities. This differential cross section is the probability of particles scattered into a bit of the solid angle $d\Omega$. Mathematically, the differential cross section for a spinless particle scattered from a static point charge can be written[12] as

$$\frac{d\sigma}{d\Omega} = \frac{\alpha^2}{4E^2 \sin^4 \frac{\theta}{2}}, \quad (15)$$

where α is known as the fine-structure constant equal to $e^2/4\pi \approx 1/137$, E is the energy of the incident electron, and θ is the scattering angle of the electron in the laboratory frame. Eq. 15 is known as the Rutherford Formula and is the simplest

⁵Just like other three-dimensional vectors, when bolded, $\mathbf{0}$ represents $(0,0,0)$.

theoretical scattering case. If we include the electron spin, we get

$$\frac{d\sigma}{d\Omega} = \frac{\alpha^2 \cos^2 \frac{\theta}{2}}{4E^2 \sin^4 \frac{\theta}{2}}, \quad (16)$$

which is known at the *Mott* cross section (we will from now on denote this particular cross section by $(\frac{d\sigma}{d\Omega})_{\text{Mott}}$). If we next introduce the mass of the point-like target M , that target particle will recoil, and so we get a scattered electron energy of

$$E' = \frac{E}{1 + \frac{2E}{M} \sin^2 \frac{\theta}{2}}, \quad (17)$$

and the Mott cross section becomes

$$\begin{aligned} \frac{d\sigma}{d\Omega} &= (\frac{d\sigma}{d\Omega})_{\text{Mott}} \cdot \frac{E'}{E} \left[1 - \frac{q^2}{2M^2} \tan^2 \frac{\theta}{2} \right] \\ &= \frac{\alpha^2 \cos^2 \frac{\theta}{2}}{4E^2 \sin^4 \frac{\theta}{2}} \cdot \frac{E'}{E} \left[1 - \frac{q^2}{2M^2} \tan^2 \frac{\theta}{2} \right]. \end{aligned} \quad (18)$$

As that target mass M increases, this equation reduces to the Mott cross section.

We are beginning to approach a more realistic mathematical description of scattering, so we must discuss the various types that exist. In Fig. 3 if both particles remain intact in their ground state after the collision, it is called *elastic scattering*. Like pool balls, they essentially bounce off each other, of course through the exchange of that virtual photon. Inelastic scattering is when an internal excitation occurs in one or both particles. We need to understand these types of scattering in more depth to understand the BONuS12 Experiment.

2.3 ELASTIC SCATTERING

When the momentum transfer, or more specifically Q^2 , is low, there is a higher probability that the lepton (at JLab, that lepton is an electron) essentially bounces off of the target particle (typically a nucleon) in what is known as elastic scattering. Whatever momentum is transferred does not force the nucleon into excited states (called resonances) or break it apart entirely (deep inelastic scattering). In a situation like Fig. 3 when scattering elastically

$$k + p \longrightarrow k' + p'. \quad (19)$$

Here k and p are the incident electron and nucleon four-momenta respectively, and k' and p' are the scattered electron and nucleon respectively. In this elastic case,

$$M_N = M'_N \quad \text{and} \quad m_e = m'_e \quad (20)$$

where M_N is the mass of the nucleon and m_e is the mass of the electron.

Because the nucleon target not point-like, we cannot simply use the Mott Equation (Eq. 16) to calculate the cross section of this elastic-scattering process. If we scatter electrons from some particle with a charge distribution $\rho(r)$ (r distance away from the charge source), like a proton, the scattering amplitude (following [13]) is modified by a form factor

$$F(q^2) = \int d^3r e^{i\mathbf{q}\cdot\mathbf{r}} \rho(r). \quad (21)$$

This particular form factor in Eq. 21 is an integral over volume of that charge distribution times the plane-wave representation of the particle. $F(q^2)$ is the Fourier transform of the charge distribution. As the name suggests this form factor provides insight into the composite structure of that particle. When this form factor is squared, it serves as a multiplier to the Mott cross section, giving us an expression for the elastic scattering cross section

$$\frac{d\sigma}{d\Omega} = \left(\frac{d\sigma}{d\Omega} \right)_{\text{Mott}} [F(q^2)]^2. \quad (22)$$

This gives us a useful description of elastic electron-proton scattering.

The last thing to do regarding the elastic scattering cross section is to expand the expression into the kinematic variables we can measure. We accomplish this by defining a scattering probability amplitude \mathcal{M} such that in the lab frame

$$\frac{d\sigma}{d\Omega} = \frac{1}{64\pi^2} \left(\frac{1}{M_p + 2E \sin^2 \frac{\theta}{2}} \right)^2 |\mathcal{M}_{fi}|^2, \quad (23)$$

where we neglect the small electron mass, M_p is the mass of the proton, E is the incident electron energy, and θ is the scattering angle of the electron in the lab frame. The term $|\mathcal{M}_{fi}|^2$ is shorthand for

$$|\mathcal{M}_{fi}|^2 = |\langle f | \mathcal{M} | i \rangle|^2, \quad (24)$$

where \mathcal{M} is the scattering probability amplitude. If the polarizations are not observed, this must be averaged over initial spin states and summed over the final spin states of $|\mathcal{M}|^2$. Mathematically, using s and S for initial spin states of the electron and proton respectively and s' and S' for final spin states, it can be expressed as

$$|\mathcal{M}_{fi}|^2 = \frac{1}{2} \frac{1}{2} \sum_{s,S} \sum_{s',S'} |\mathcal{M}|^2. \quad (25)$$

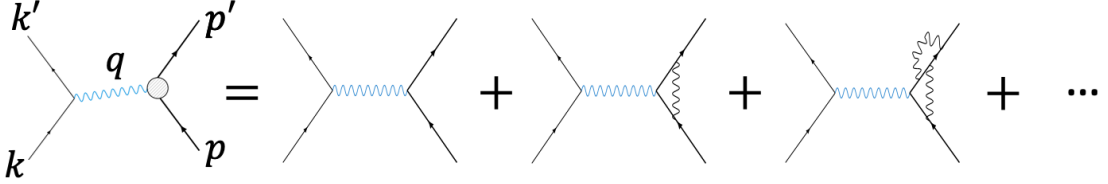


Fig. 5: The contributions of higher order diagrams.

The scattering probability amplitude cannot be known exactly because of the processes beyond the first order (tree level) that could occur in Fig. 3 at the proton- γ^* vertex blob (these contributions can be seen in Fig. 5). However, we can handle the mathematical description of these processes by expressing the scattering probability amplitude matrix in terms of the leptonic and hadronic tensors

$$|\mathcal{M}|^2 = \frac{e^4}{Q^4} \ell_{\mu\nu} W^{\mu\nu}. \quad (26)$$

The leptonic tensor $\ell_{\mu\nu}$ is associated with the coupling of the virtual photon to the electron (more generally the coupling of the exchange boson to the lepton), and for unpolarized scattering can be expressed as

$$\ell_{\mu\nu} = \bar{u}(k', s') \gamma^\mu u(k, s) \bar{u}(k, s) \gamma^\nu u(k', s'). \quad (27)$$

The term $u(k)$ is the Dirac spinor. For the electron (a spin-1/2 fermion), there are two spin states (*i.e.* up or down) so there are two associated spinors that could exist here

$$u_\uparrow(k) = \begin{pmatrix} 1 \\ 0 \\ \frac{k_z}{E+m} \\ \frac{k_x+ik_y}{E+m} \end{pmatrix} \text{ and } u_\downarrow(k) = \begin{pmatrix} 0 \\ 1 \\ \frac{k_x-ik_y}{E+m} \\ \frac{-k_z}{E+m} \end{pmatrix}, \quad (28)$$

where m is the lepton mass, $k_{x,y,z}$ are the momentum components of the initial lepton. In Eq. 27, γ^μ are the gamma matrices. When summed and averaged over spins, the leptonic tensor (following [14, ?]) becomes

$$\begin{aligned} \ell_{\mu\nu} &= \text{Tr} \left[\frac{\not{k}' + m}{2m} \gamma^\mu \frac{\not{k} + m}{2m} \gamma^\nu \right] \\ &= \frac{1}{m^2} \text{Tr}(\not{k}' \gamma^\mu \not{k} \gamma^\nu + m^2 \gamma^\mu \gamma^\nu) \\ &= 2(k'^\mu k^\nu + k^\mu k'^\nu - g^{\mu\nu} k' \cdot k). \end{aligned} \quad (29)$$

Thus far we have from Eq. 26

$$|\mathcal{M}|^2 = \frac{e^4}{Q^4} 2(k'^\mu k^\nu + k^\mu k'^\nu - g^{\mu\nu} k' \cdot k) W^{\mu\nu}, \quad (30)$$

where $g^{\mu\nu}$ is the metric tensor.

We must now take a look at the hadronic tensor $W^{\mu\nu}$, which is more complicated because we must take into account the proton's structure. In fact, the hadronic tensor cannot be known exactly. It can, however, be expanded to the second order as

$$W^{\mu\nu} = \langle p | J^\nu | p' \rangle \langle p' | J^\mu | p \rangle, \quad (31)$$

which depends on the J^μ current matrix elements. That current between two nucleon states (following [13])

$$\langle p | J^\mu(0) | p' \rangle = \bar{U}(p') \left[F_1(Q^2) \gamma^\mu + F_2(Q^2) \frac{i\sigma^{\mu\nu}}{2M_N} \right] U(p) \quad (32)$$

gives rise to two form factors, $F_1(Q^2)$ which is called the Dirac form factor and $F_2(Q^2)$ called the Pauli form factor. Here $\sigma^{\mu\nu} = \frac{i}{2}[\gamma^\mu, \gamma^\nu]$ and we denote the difference between the lower-case $u(k, s)$ electron spinors from Eq. 27 and upper-case $U(p)$ nucleon spinors. If we introduce the more physically interesting Sach's electric and magnetic form factors respectively

$$G_E(Q^2) = F_1(Q^2) + \frac{Q^2}{4M_N^2} F_2(Q^2)$$

$$G_M(Q^2) = F_1(Q^2) + F_2(Q^2),$$

then the hadronic tensor can be written as

$$\begin{aligned} W^{\mu\nu} &= 2(p'^\mu p^\nu + p'^\nu p^\mu - g^{\mu\nu}(pp' - M_N^2)) G_M^2 \\ &\quad - 2F_2 G_M (p + p')^\mu (p + p')^\nu + F_2^2 \frac{M_N^2 + p \cdot p'}{2M_N^2} (p + p')^\mu (p + p')^\nu \\ &= (-q^\mu q^\nu + g^{\mu\nu} q^2) G_M^2 + (p + p')^\mu (p + p')^\nu \frac{G_E^2 + \tau G_M^2}{1 + \tau} \\ &= g^{\mu\nu} q^2 G_M^2 + 4p^\mu p^\nu \frac{G_E^2 + \tau G_M^2}{1 + \tau} + \dots, \end{aligned} \quad (33)$$

where we define $\tau = Q^2/4M_N^2$ to simplify the expression. Because of current conservation, the terms containing factors of q^μ are omitted with the ellipses, since they do not contribute to the cross section.

Substituting our expressions for the leptonic and hadronic tensors for elastic scattering in the lab frame and contracting them, we arrive at

$$\frac{d\sigma}{d\Omega} = \left(\frac{d\sigma}{d\Omega} \right)_{\text{Mott}} f_{\text{rec}} \left[\frac{G_E^2(Q^2) + \tau G_M^2(Q^2)}{1 + \tau} + 2\tau G_M^2 \tan \frac{\theta}{2} \right], \quad (34)$$

where $\left(\frac{d\sigma}{d\Omega} \right)_{\text{Mott}}$ comes from Eq. 16 (*i.e.* the Mott cross section) and f_{rec} is the recoil factor equal here to E'/E . As Q^2 gets very high, τ increases and the magnetic form factor $G_M(Q^2)$ dominates. Eq. 34 gives a more physical description of the elastic scattering cross section in terms of kinematic variables that can be measured through scattering experiments.

One more kinematic variable that needs to be introduced offers insight into cases when scattering enters into inelastic regimes. The invariant mass squared W^2 (not to be confused with the hadronic tensor $W^{\mu\nu}$) of the photon-nucleon system, is defined mathematically as

$$W^2 = (q + p)^2 = M_N^2 + 2M_N\nu - Q^2, \quad (35)$$

where $\nu = E - E'$ is the energy transferred from the electron to the nucleon via virtual photon (γ^*). In the elastic scattering case, $W^2 = M_N^2$, because Q^2 and thus ν are small (*i.e.* $E \ll M_N$). As Q^2 increases, instead of simply bouncing off of the nucleon, the energy transferred to the nucleon begins changing the state of the quarks within the nucleon.

2.4 RESONANCE REGION

Changing the state of a quark within the nucleon results in excited states of that nucleon, called *resonances*. The region where resonances occur is $M_N^2 < W^2 < 4 \text{ GeV}^2$, and is called the *resonance region*. There are 6 families of resonances that depend on the characteristics of the resonant particles. Particles containing only u and d quarks, whose isospin $I = \frac{1}{2}$, are denoted by N . The Δ family of resonances also have only u and d quarks, but have $\frac{3}{2}$ isospin. When $I = 0$ and the particle contains u , d and one c , s , or b quark, it is called a Λ resonance. The Σ resonance also has u , d plus one c , s , or b quark, but with $I = 1$. When only one u or d quark exists with two c , s , or b quarks with $I = \frac{1}{2}$, it is a Ξ resonance. Finally, when $I = 0$ and only c , s , or b quarks are present, it is known as an Ω resonance[15].

Unlike the ground state of nucleons, these excited states are extremely short lived (on the order of 10^{-23} seconds). After their short life, these resonances decay into

more stable hadrons. Detection of these hadrons is what provides proof of the existence of resonant states. For example, a common resonance $\Delta^0(1232)$, which is the lowest lying resonance with a mass of 1.232 GeV[15], predominately decays via the strong interaction into a pion (π^0) and a neutron (n) or to $\pi^- p$. The entire interaction begins at the first step of creating an excited state

$$p + e^- \longrightarrow \Delta^0 + e' \quad (36)$$

then decays into

$$\Delta^0 \longrightarrow \pi^0 + n. \quad (37)$$

However, because these resonances are so short-lived, it is convention to express the entire interaction as

$$p + e^- \longrightarrow e'^- + \pi^0 + n.$$

$$p + e^- \longrightarrow e'^- + \pi^- + p. \quad (38)$$

One reason for this convention is that there are many resonances that can produce the same final state(*i.e.* π^0 and n in our example). Knowing exactly what resonance produced a particular final state can be difficult. In the example of Eq. 38, the Δ^0 has the same quark makeup as the neutron (*i.e.* *udd*), but is much heavier. Measuring the invariant mass of the resulting particles is one of the few ways to understand what resonance occurred.

Similar to elastic scattering, interactions with resonances can be described using form factors. The analogous cross section (following the treatment of [16]) is

$$\frac{d\sigma}{d\Omega} = \left(\frac{d\sigma}{d\Omega} \right)_{\text{Mott}} f_{\text{rec}} \left(\frac{|G_E|^2 + \tau^* |G_T|^2}{1 + \tau^*} + 2\tau^* |G_T|^2 \tan^2 \frac{\theta}{2} \right) R(W), \quad (39)$$

where f_{rec} is the recoil factor of the proton, τ^* is the analogous kinematic quantity of τ from elastic scattering, G_E and G_T are the resonance longitudinal and transverse form-factors respectively, and $R(W)$ is called the resonance line shape. In inelastic scattering of resonances

$$f_{\text{rec}} = \frac{E'}{E} \left[\frac{1}{1 - \frac{(W_R^2 - M_N^2)}{2M_N E}} \right], \quad (40)$$

and

$$R(W) = \frac{2\pi^{-1} W_R M_N \Gamma_R}{(W^2 - W_R^2)^2 + W_R^2 \Gamma_R^2}. \quad (41)$$

The quantities W_R and Γ_R refer to the resonance mass and width respectively. If the resonance width is small enough (*i.e.* when $W_R = M_N$ and $W_R\Gamma_R \rightarrow 0$), $R(W)$ becomes a δ -function and the resonance cross section reduces to that of an elastic cross section.

At low Q^2 , we can describe interactions by constituent quarks models. At high Q^2 we enter a region best described with perturbative quantum chromodynamics (pQCD). We will discuss more about pQCD in a later section. The resonance region is an important bridge between these two regimes. Determining resonance form factors allows us to describe the resonance transition the same way elastic form factors describe elastic interactions.

2.5 DEEP INELASTIC SCATTERING

Once the energy transferred to the nucleon (Q^2) becomes large enough, the probability of creating excited (resonance) states decreases and there becomes a higher probability of the virtual photon “elastically” scattering off a quark inside the nucleon. This is known as *deep* inelastic scattering. This happens at roughly $W > 2$ MeV and $Q^2 > 1$ GeV 2 . In this regime we can probe the inner structure of the nucleon.

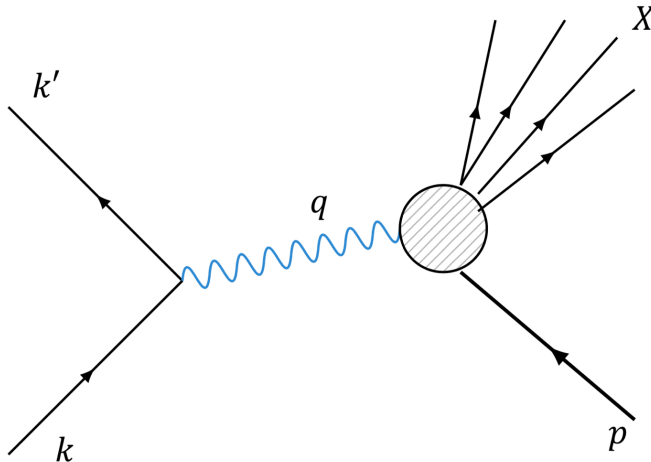


Fig. 6: Feynman diagram of deep inelastic electron scattering from a proton.

However, because the energy transfer is so high, the proton often breaks apart in the interaction

$$ep \longrightarrow e'X, \quad (42)$$

where X denotes all possible particles that might emerge from the proton-electron collision. The Feynman diagram also must be altered from Fig. 3 to Fig. 6, where X again represents all possible emerging particles. The deep-inelastic scattering cross section can be written (following [13]) as

$$\frac{d^2\sigma}{dE'\Omega} = \frac{4\alpha^2 E'^2}{q^4} \left[W_2(\nu, Q^2) \cos^2 \frac{\theta}{2} + 2W_1(\nu, Q^2) \sin^2 \frac{\theta}{2} \right], \quad (43)$$

where W_1 and W_2 are called inelastic structure functions. These structure functions are the analogs to the form factors in Eq. 34 for elastic scattering. There is much more to discuss about deep-inelastic scattering, but first we must discuss how to treat scattering off quarks (or more broadly, partons) within a nucleon with an approach called *scaling*.

2.6 PARTONS AND BJORKEN-SCALING

The way we probe inside nucleons is with the exchange of small wavelength (large Q^2) virtual photons, which interacts with partons inside the nucleon. This can be handled using the inelastic structure functions W_1 and W_2 , which are functions of the energy lost by the electron due to nucleon recoil (*i.e.* ν) and the negative four-momentum squared of the virtual photon (*i.e.* Q^2). When the virtual photon has a small enough wavelength (large enough Q^2), the nucleon that was once described by Eq. 34 starts to look more like a free Dirac particle and the cross section (following [13]) becomes

$$\frac{d\sigma}{dE'd\Omega} = \frac{4\alpha^2 e_q^2 E'^2}{q^4} \left(\cos^2 \frac{\theta}{2} - \frac{q^2}{2m^2} \sin^2 \frac{\theta}{2} \right) \delta \left(\nu + \frac{q^2}{2m} \right). \quad (44)$$

Remarkably, this is the equation for the electron elastic scattering cross section from a structureless particle[13]. Here e_q is the fractional charge of that structureless particle and m is that particle's mass. This particle inside the nucleon was eventually called a quark.

In this case, where the virtual photon elastically scatters off of a quark within the nucleon described by Eq. 44, the nucleon structure functions become

$$2W_1^{\text{point}} = \frac{Q^2}{2m^2} \delta \left(\nu - \frac{Q^2}{2m} \right) \quad (45)$$

and

$$W_2^{\text{point}} = \delta \left(\nu - \frac{Q^2}{2m} \right). \quad (46)$$

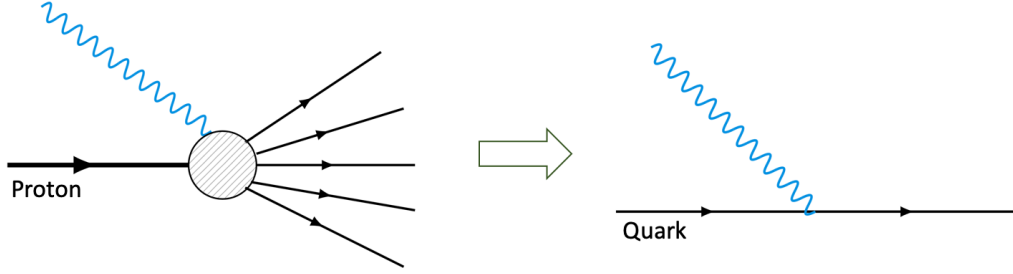


Fig. 7: The transition from inelastic scattering to deep inelastic scattering of a virtual photon and the quark within a nucleon.

Here, thus in Eq. 44, there exists the delta function that conserves energy in the interaction. Fig. 7 shows the resulting diagram when we take the right side of Fig. 6 (the left side of Fig. 7) and begin to probe a single quark inside the nucleon (the right side of Fig. 7). This reduction is representative of the electron elastically scattering off a quark in the nucleon.

If we take Eq. 45 and 46, using the identity $\delta(x/a) = a\delta(x)$, we can write

$$2mW_1^{\text{point}}(\nu, Q^2) = \frac{Q^2}{2m\nu} \delta\left(1 - \frac{Q^2}{2m\nu}\right)$$

$$\nu W_2^{\text{point}}(\nu, Q^2) = \delta\left(1 - \frac{Q^2}{2m\nu}\right). \quad (47)$$

These equations for the structure functions are now dimensionless and depend on only the ratio $Q^2/2m\nu$, which is both important and useful. That usefulness is as follows: when Q^2 is high enough, the virtual photon begins to elastically scatter off of structureless (point) particles within the nucleon and can be described using the dimensionless structure functions

$$MW_1(\nu, Q^2) \xrightarrow[\text{large } Q^2]{} F_1(x_B)$$

$$\nu W_2(\nu, Q^2) \xrightarrow[\text{large } Q^2]{} F_2(x_B). \quad (48)$$

Here x_B is introduced as the Bjorken- x scaling variable defined as

$$x_B = \frac{Q^2}{2M\nu}, \quad (49)$$

which describes the momentum fraction of a quark or gluon within a nucleon. Up to this point, we have only discussed interactions between the virtual photon and the quarks within the nucleon, but that virtual photon can also interact with gluons that exists in the nucleon. Collectively, these quarks and gluons in the nucleon are known as partons. The Bjorken- x scaling variable can describe the momentum fraction of any parton within a nucleon.

The relationship between the structure functions $F_1(x_B)$ and $F_2(x_B)$ (known as the Callan-Gross relation) is

$$2x_B F_1(x_B) = F_2(x_B) = \sum_i e_i^2 f_i(x_B). \quad (50)$$

In the right side of this expression we have a sum over partons (the parton index is i) of the square of that parton's charge (e_i^2) times $f_i(x_B)$, known at the parton distribution function (or PDF)

$$f_i(x_B) = \frac{dP_i}{dx_B}, \quad (51)$$

describes the probability P_i that a struck parton i carries a fraction (x_B) of the nucleon's momentum.

Because $F_2(x_B)$ offers a straightforward interpretation in terms of quarks, the F_2 structure function is the more important term here to examine experimentally and is of interest in the BONuS12 Experiment. For deep-inelastic electron-proton scattering, the $F_2^p(x_B)$ structure function is

$$\frac{1}{x_B} F_2^p(x_B) = \left(\frac{2}{3}\right)^2 [u^p(x_B) + \bar{u}^p(x_B)] + \left(\frac{1}{3}\right)^2 [d^p(x_B) + \bar{d}^p(x_B)] \quad (52)$$

$$+ \left(\frac{1}{3}\right)^2 [s^p(x_B) + \bar{s}^p(x_B)], \quad (53)$$

where p superscript denotes that we are dealing with the proton structure, and the PDF $f_i(x_B)$ is replaced with the first letter of the quark name (*e.g.* the up quark and antiquark PDF's are denoted as $u^p(x_B)$ and $\bar{u}^p(x_B)$ respectively). The contributions of quarks heavier than the strange quark have been assumed to be negligible here. The neutron structure function $F_2^n(x)$, where we have dropped the B in x_B , is

$$\frac{1}{x} F_2^n(x) = \left(\frac{2}{3}\right)^2 [u^n(x) + \bar{u}^n(x)] + \left(\frac{1}{3}\right)^2 [d^n(x) + \bar{d}^n(x)] \quad (54)$$

$$+ \left(\frac{1}{3}\right)^2 [s^n(x) + \bar{s}^n(x)]. \quad (55)$$

This looks similar to the F_2^p structure function because the proton and neutron are together part of an isospin doublet. When particles are members of an isospin doublet, they can transform into each other under an $SU(2)$ transformation

$$\begin{pmatrix} p \\ n \end{pmatrix} \xrightarrow{SU(2)} \exp\left(-\frac{i}{2}\theta_a\sigma_a\right) \begin{pmatrix} p \\ n \end{pmatrix},$$

where p and n are proton and neutron states, and σ_a are the Pauli matrices. This transformation means that the quark contents of the proton and neutron are related.

2.7 NUCLEON STRUCTURE-FUNCTION RATIO F_N^2/F_P^2

We can exploit this relation between quark contents of protons and neutrons to study the structure of nucleons, in particular the neutron structure. That relationship between quark contents means

$$\begin{aligned} u^p(x) &= d^n(x) \equiv u(x), \\ d^p(x) &= u^n(x) \equiv d(x), \\ s^p(x) &= s^n(x) \equiv s(x). \end{aligned} \tag{56}$$

(57)

The probability of finding a u quark in a proton is the same as the probability of finding a d quark in a neutron. Each nucleon consists not only of u_v and d_v quarks that determine the quantum numbers of the nucleon (called *valence* quarks, hence the subscript v), but many quark-antiquark pairs in a constant state of creation and annihilation (known as *sea* quarks). In the first order approximation, we can assume that the lighter quark-antiquark pairs $u_s\bar{u}_s$, $d_s\bar{d}_s$, and $s_s\bar{s}_s$ contribute to this “sea” and we can neglect contributions from the heavier quark-antiquark pairs $c_s\bar{c}_s$ and so on.

This approximation of the nucleon structure results in adding the sea quarks to the contributions of each quark type. That is

$$\begin{aligned} u(x) &= u_v(x) + u_s(x), \\ d(x) &= d_v(x) + d_s(x), \end{aligned} \tag{58}$$

$$u_s(x) = \bar{u}_s(x) = d_s(x) = \bar{d}_s(x) = s_s(x) = \bar{s}_s(x) = S(x), \tag{59}$$

where we now use $S(x)$ for all sea quark contributions. If we combine this relationship with our expressions for the proton and neutron structure functions Eqs. 52 and 54,

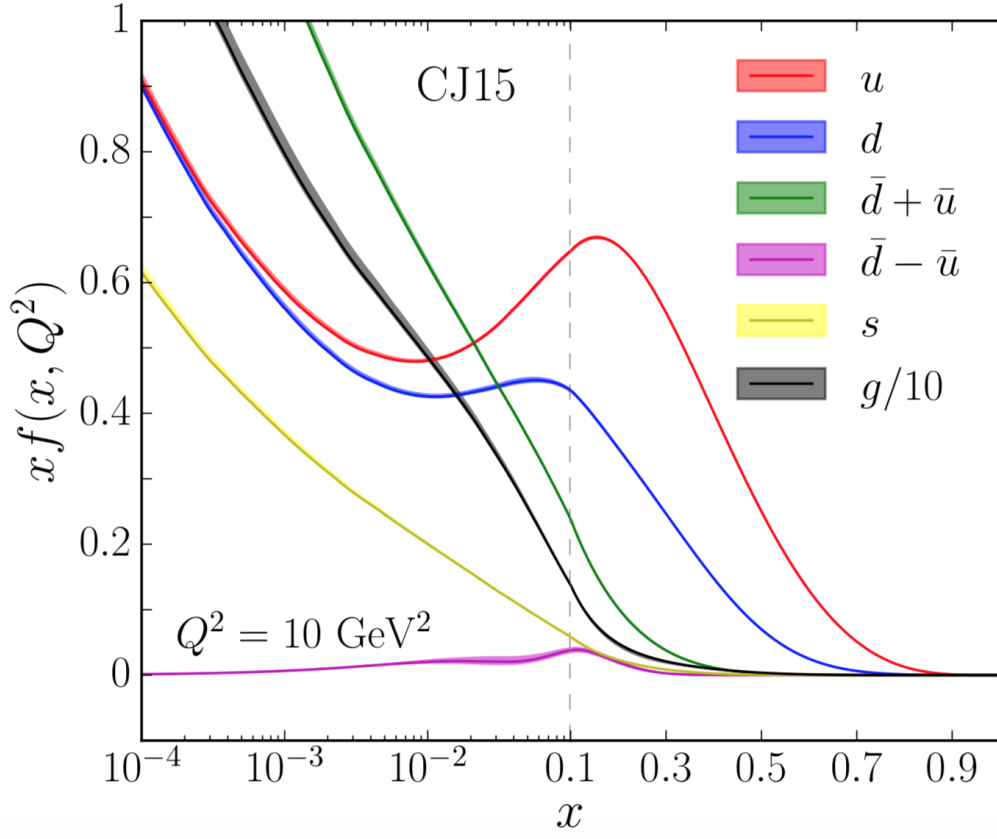


Fig. 8: Comparison of CJ15 PDFs $xf(x, Q^2)$ for different flavors ($f = u, d, \bar{d} + \bar{u}, \bar{d}\bar{u}$, s and $g/10$) at a scale $Q^2 = 10 \text{ GeV}^2$, with 90% CL uncertainty bands. Note the combined logarithmic/linear scale along the x-axis.[1]

respectively, we get

$$\frac{1}{x} F_2^p = \frac{1}{9}[4u_v + d_v] + \frac{4}{3}S \quad (60)$$

and

$$\frac{1}{x} F_2^n = \frac{1}{9}[u_v + 4d_v] + \frac{4}{3}S, \quad (61)$$

where the $\frac{4}{3}$ comes from summing over all six sea quark distributions. In the low x limit (*i.e.* $x \rightarrow 0$), the ratio of F_n^2/F_2^p goes to unity, or

$$\frac{F_2^n}{F_2^p} \xrightarrow{x \rightarrow 0} 1. \quad (62)$$

However, as we approach $x \rightarrow 1$ that ration becomes

$$\frac{F_2^n}{F_2^p} \xrightarrow{x \rightarrow 1} \frac{u + 4d}{4u + d}, \quad (63)$$

where u and d are the valance *up* and *down* quarks and $S \rightarrow 0$. We can see in Fig. 8 that as $x > 0.3$, the u and d quarks dominate, so Eq. 63 neglects the sea-quark contributions as well as *strange* and larger mass sea-quark contributions. We can rearrange Eq. 63 to get the d/u ratio

$$\frac{d}{u} \approx \frac{4F_2^n/F_2^p - 1}{4 - F_2^n/F_2^p}, \quad (64)$$

which provides important insight into the parameterizations of PDFs at large x .

2.8 MODELS AND PREDICTIONS

If SU(6) symmetry were exact, then the u and d quarks within the proton would be identical with the exceptions of charge and flavor. The wave function of a proton polarized in the $+z$ direction [17] would be

$$\begin{aligned} p \uparrow = & \frac{1}{2}u \uparrow (ud)_{S=0} + \frac{1}{\sqrt{18}}u \uparrow (ud)_{S=1} - \frac{1}{3}u \downarrow (ud)_{S=1} \\ & - \frac{1}{3}d \uparrow (uu)_{S=1} - \frac{\sqrt{2}}{3}d \downarrow (uu)_{S=1}, \end{aligned} \quad (65)$$

where the subscript are the spins of the diquark pairs. The quark distribution in this case would be the same for both u and d quarks, which implies $u = 2d$ for all x . This leads to the F_2 structure function and d/u ratios

$$\frac{F_2^n}{F_2^p} = \frac{2}{3}, \quad \frac{d}{u} = \frac{1}{2}. \quad (66)$$

This is known as the SU(6) quark model. This symmetry, however, is broken in nature as there is a nonzero difference between quark masses as well as a measured value of the F_2^n/F_2^p ratio far below 2/3.

There are a few explanations out there for SU(6) symmetry breaking. Close [18] and Cartlitz [19] observed the correlation between large- x behavior of F_2^n/F_2^p and the mass splitting of the nucleon and Δ baryons. They assumed that the stuck nucleon breaks into a single quark which interacts with the virtual photon and a diquark pair. When $x \rightarrow 1$, the $S = 1$ state term becomes small compared to the $S = 0$ state term. This suppression of the $S = 1$ diquark state can explain the symmetry breaking and leads to the first term in Eq. 65 to dominating. Therefore at $x \approx 1$, F_2^p is essentially given by the single u quark distribution and so

$$\frac{F_2^n}{F_2^p} = \frac{1}{4}, \quad \frac{d}{u} = 0. \quad (67)$$

Isgur [20] [21] describes this d -quark suppression by a color hyperfine interaction arising from a one-gluon exchange. In the lowest order, the Hamiltonian of the hyperfine-perturbed quark model for the color-magnetic hyperfine interaction between two quarks is proportional to $S_i \cdot S_j$, where S_i is the spin vector of quark i . This means that if the spins are parallel, the force is repulsive, and if the spins are anti-parallel then the force is attractive. Therefore, $S = 1$ is suppressed and $d/u = 0$ as $x \rightarrow 1$.

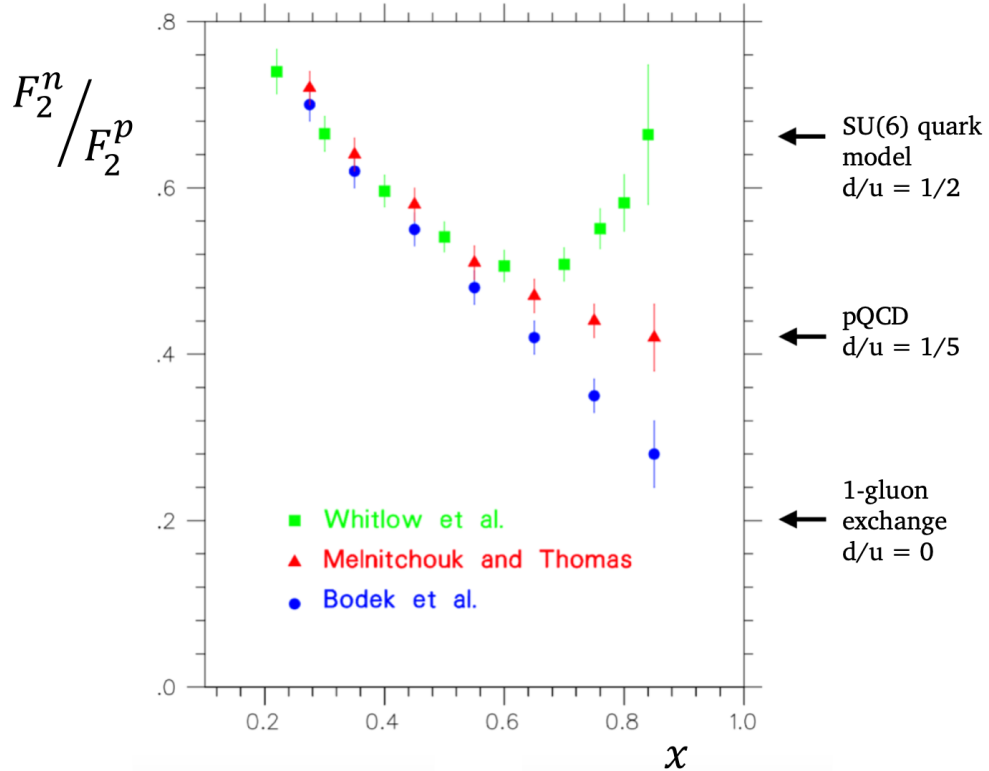


Fig. 9: Model dependence of F_2^n/F_2^p . [2]

The last model that will be introduced here that proposed to explain the SU(6) symmetry breaking is based on perturbative QCD first from Farrar and Jackson [22]. They put forward that at $x \approx 1$, the hadronic structure functions could be calculated to the lowest order perturbation theory to $O(m^2/q^2)$, where the incoming quarks could be thought of as “free”. The valence quark wave function that dominates here is the diquark spin projection $S_z = 0$. When the spins of two quarks are aligned, scattering is suppressed by a factor of $(1 - x)$ less than anti-aligned quarks. That is, $S_z = 0$ diquark states dominate when $x \rightarrow 1$. The u quark having the same helicity as the proton is 5 times as likely as the d having the same helicity as the proton.

This results in

$$\frac{F_2^n}{F_2^p} = \frac{3}{7}, \quad \frac{d}{u} = \frac{1}{5}. \quad (68)$$

More recently, Brodsky [23] used a hard gluon exchange model based on quark counting rules leading to the same conclusion.

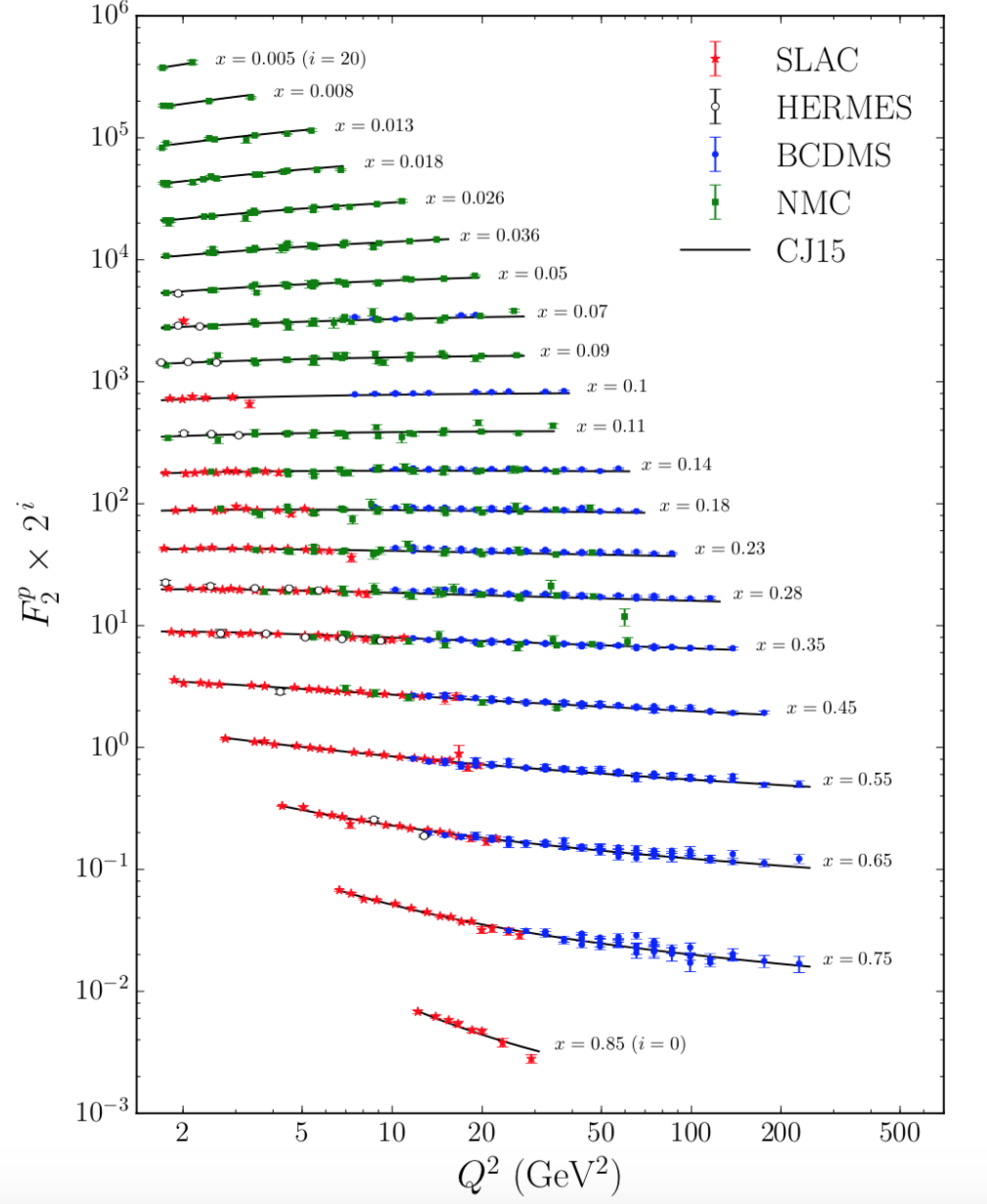


Fig. 10: Measured values of F_2^p vs Q^2 for different values of x . [1]

All of these predictions can be summarized in Fig. 9, which makes it obvious that the value of F_2^n/F_2^p is very much model dependent. It is the goal of the BONuS12

experiment to measure this ratio in a model independent way. In order to do this, we need to know the values of both F_2^p and F_2^n to high precision. Much is known about the F_2^p structure function because it can be extracted from electron scattering from protons in hydrogen targets. Fig. 10 shows the multiple experiments and kinematic ranges where F_2^p has been measured. The trouble with Eq. 63 and Eq. 64 is our knowledge of the F_2^n structure function.

2.9 DIFFICULTIES IN EXTRACTING F_2^N/F_2^P FROM DEUTERIUM

There are no free neutron targets to conduct scattering experiments from like there is for protons in hydrogen targets. Free neutrons decay in about 15 minutes and are electrically neutral, which means they cannot be confined using magnets. Therefore, the F_2^n structure function must be extracted from scattering experiments using targets like Helium-3 (two protons and a neutron), Helium-4 (two protons and two neutrons), and deuterium (one proton and one neutron). The BONuS12 Experiment uses a deuterium target.

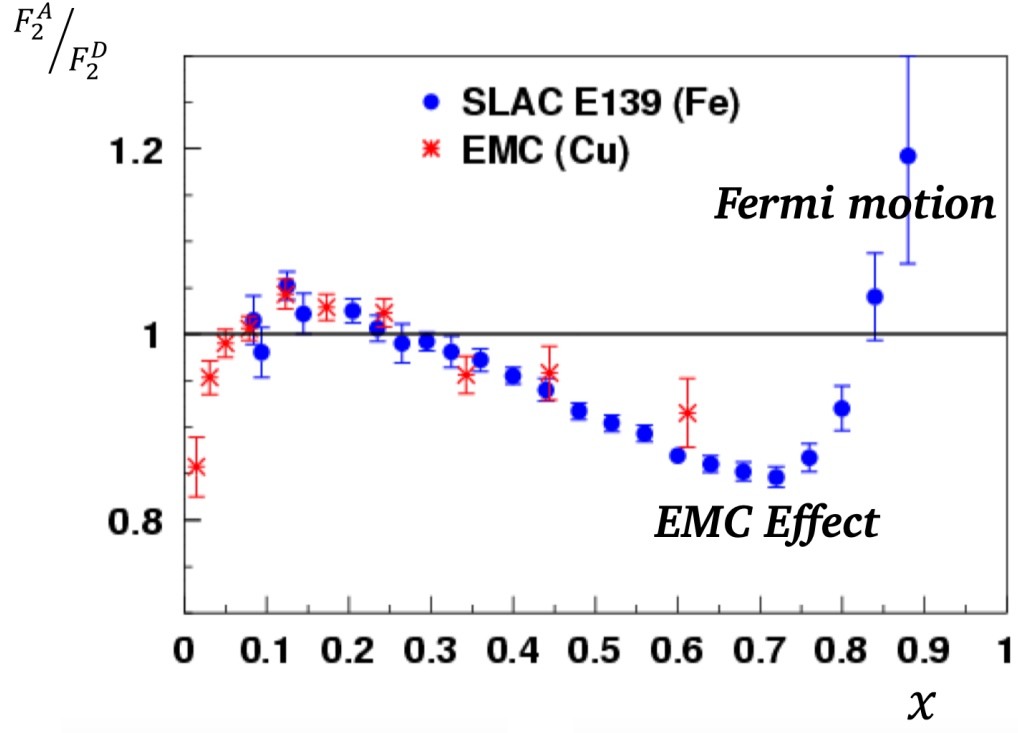


Fig. 11: Variations of the F_2^A/F_2^D ratio from unity indicating various nuclear binding effects. [3][4]

The trouble with using any nuclear target with two or more nucleons to study the structure of a single nucleon is that those nucleons do not behave as they do when they are free. Early DIS experiments by the Electron Muon Collaboration (EMC) in CERN found that the ratio F_2^A/F_2^D (superscript A denotes the mass number of a nuclear target and D denotes deuterium) was not unity for all values of x . Fig. 11 shows that deviation for experiments done on iron and copper nuclei. This deviation indicates that quark distributions are different for free and bound nucleons.

Because the EMC first discovered this phenomena, the deviation between $0.2 < x < 0.8$ was dubbed the EMC effect. The other contributors are known as shadowing ($x < 0.1$), anti-shadowing ($0.1 < x < 0.2$) and $x > 0.8$ is believed to be due to Fermi motion. Just like partons in a nucleon, nucleons in a nucleus are not stationary. Fermi motion refers to the motion of nucleons within a nucleus.

There are many models attempting to explain the EMC effect (for a detailed review, see [24]), but none have been proven experimentally. The EMC effect is not proportional to A (this was proven with scattering from ${}^4\text{He}$) or average nuclear density (ruled out by scattering from ${}^9\text{Be}$). However, a model of Q^2 rescaling pointing to increased quark confinement, which could explain the EMC effect[24].

2.10 SPECTATOR TAGGING

The goal of the BONuS12 Experiment and other experiments concerned with measuring the structure of neutrons is to do so without significant model dependence at high- x or involvement of bound-nucleon issues. To do this effectively, since the neutron of interest is bound within a nucleus, BONuS12 uses a method called spectator tagging. In particular, since the electron (e) is meant to scatter from the neutron within deuterium (D) in the interaction

$$eD \longrightarrow e' p_s X, \quad (69)$$

the proton (p_s) needs to be a spectator to the reaction. That is, the proton plays no role in the interaction, thereby not interacting with any of the debris (X) coming from the struck neutron.

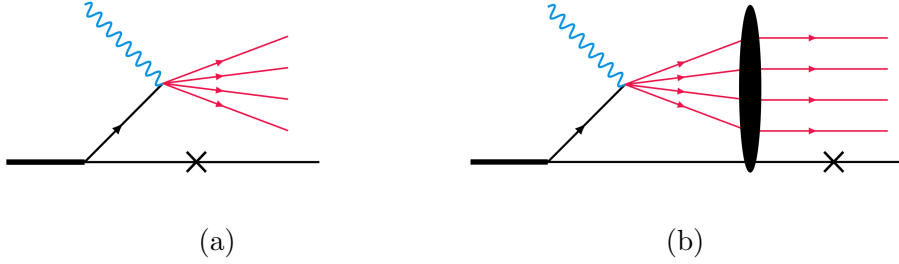


Fig. 12: Impulse approximation (a) and final state interaction diagrams (b).

The cross section of the reaction given in Eq. 69 [25] is

$$\frac{d\sigma}{dxdQ^2d^3p_s/E_s} = \frac{4\pi\alpha_{em}^2}{xQ^4} \left(1 - y - \frac{x^2y^2M_N^2}{Q^2} \right) \times \left[F_L^D + \left(\frac{Q^2}{2q^2} + \tan^2\left(\frac{\theta}{2}\right) \right) \frac{\nu}{M_N} F_T^D + \left(\frac{Q^2}{2q^2} + \tan^2\left(\frac{\theta}{2}\right) \right)^{1/2} F_{TL}^D \cos\phi + F_{TT}^D \cos(2\phi) \right], \quad (70)$$

where α_{em} is the electromagnetic coupling constant, $y = \nu/E_e$, $\nu = E_e - E'_e$, M_N is the mass of the nucleon, ϕ is the azimuthal angle of the recoiling nucleon, and $F_{L,T,LT,TT}$ are nuclear structure functions. These structure functions depend on Q^2 , x , p_s^\perp , and $\alpha_s = \frac{E_s - p_s^z}{M_D}$, which is the light-cone momentum fraction of the deuteron carried by the spectator.

For practical considerations, one must integrate over ϕ to get (following [25])

$$\frac{d\sigma}{dxdQ^2d^3p_s/E_s} = \frac{4\pi\alpha_{em}^2}{xQ^4} \left(1 - y - \frac{x^2y^2M_N^2}{Q^2} \right) \left[F_{2D}^{SI} + 2\tan^2\left(\frac{\theta}{2}\right) \frac{\nu}{M_N} F_{1D}^{SI} \right], \quad (71)$$

where

$$F_{2D}^{SI}(x, Q^2, \alpha_s, p_s^\perp) = F_L^D + \frac{Q^2}{2q^2} \frac{\nu}{M_N} F_T^D \quad (72)$$

and

$$F_{1D}^{SI}(x, Q^2, \alpha_s, p_s^\perp) = \frac{F_T^D}{2}. \quad (73)$$

The assumption in Eq. 69 is that the reaction occurs when the momentum of the spectator proton is less than 700 MeV/c [25], where the virtual photon interacts with only one of the bound nucleons. Particles produced from the reaction can interact in the final state with the spectator nucleon. Two diagrams contribute to the cross section: the impulse approximation when the particle debris from the struck nucleon does not interact with the other nucleon (Fig. 12a), and the case where rescattering

occurs of the recoil nucleon with the other products of the deep inelastic scattering (DIS) interaction (Fig. 12b), called final-state interactions.

2.10.1 IMPULSE APPROXIMATION

The ideal interaction for studying the structure of the neutron from DIS from deuterium is the impulse approximation (IA). In the IA, the recoil nucleon is a spectator of the virtual photon γ^* scattering off the bound nucleon N . Using the Feynman rules, the IA amplitude is

$$A_{IA}^\mu = \langle X | J_{em}^\mu(Q^2, \nu, p_s) \frac{\not{p}_D - \not{p}_s + m}{M_N^2 - t} \bar{u}(p_s) \Gamma_D, \quad (74)$$

where $J_{em}^\mu(Q^2, \nu, p_s)$ represents the electromagnetic DIS operator of the electron scattering off the bound nucleon, $t = (p_D - p_s)^2$, and Γ_D is the covariant $D \rightarrow pn$ transition vertex.

If we take the recoil nucleon in Fig. 12a on the mass shell and using [25]

$$\not{p}_D - \not{p}_s + m \approx \sum_{\text{spins}} u(p_D - p_s) \bar{u}(p_D - p_s), \quad (75)$$

we can factorize Eq. 74 into two parts: (1) the DIS current of the bound nucleon (*i.e.* $J_{X,N}^\mu = \langle X | J_{em}^\mu(Q^2, \nu, p_s) u(p_D - p_s) \rangle$), and (2) the wave function of the deuteron. This factorization provides us with nuclear DIS structure functions through convolution of bound nucleon structure functions (F_{1D}^{eff} and F_{2D}^{eff}) and the nuclear spectral function S , which (following [25]) are

$$\begin{aligned} F_{2D}^{SI}(x, Q^2, \alpha_s, p_s^\perp) &= \frac{S(\alpha_s, p_s^\perp)}{n} \frac{M_N \nu}{pq} \\ &\times \left[(1 + \cos \delta)^2 \left(\alpha + \frac{pq}{Q^2} \alpha_q \right)^2 + \frac{1}{2} \frac{(p_s^\perp)^2}{M_N^2} \sin^2 \delta \right] F_{2D}^{\text{eff}}(\tilde{x}, Q^2, \alpha_s, p_s^\perp), \\ F_{1D}^{SI}(x, Q^2, \alpha_s, p_s^\perp) &= \frac{S(\alpha_s, p_s^\perp)}{n} \left[F_{1D}^{\text{eff}}(\tilde{x}, Q^2, \alpha_s, p_s^\perp) + \frac{(p_s^\perp)^2}{2pq} F_{2D}^{\text{eff}}(\tilde{x}, Q^2, \alpha_s, p_s^\perp) \right], \end{aligned} \quad (76)$$

where $\sin^2 \delta = Q^2 / \mathbf{q}^2$. In the virtual-nucleon (VN) approximation $n = M_D / 2(M_D - E_s)$ and in the light-cone (LC) approximation $n = 2 - \alpha_s$. The modified Bjorken- x is given in the lab frame by

$$\tilde{x} \approx \frac{Q^2}{2M\nu(2 - \alpha)}. \quad (77)$$

The nuclear spectral function S gives us the probability of finding an interacting nucleon with momentum (α, p^\perp) in the target and a recoil nucleon with momentum

(α_s, p_s^\perp) in the final state of the reaction. In the IA, $\alpha + \alpha_s = 2$ and $\mathbf{p}^\perp = -\mathbf{p}_s^\perp$. Putting this all together, we can use Eq. 76 in 70 to get

$$\begin{aligned} \frac{d\sigma}{dx dQ^2 d^3 p_s / E_s} = & \frac{4\pi\alpha_{em}^2}{x Q^4} \left(1 - y - \frac{x^2 y^2 M_N^2}{Q^2}\right) \frac{S(\alpha_s, p_s^\perp)}{n} \\ & \times \left(\frac{M_N \nu}{pq} \left[(1 + \cos \delta)^2 \left(\alpha + \frac{pq}{Q^2} \alpha_q \right)^2 + \frac{1}{2} \frac{(p_s^\perp)^2}{M_N^2} \sin^2 \delta \right] \right. \\ & \times F_{2D}^{\text{eff}}(\tilde{x}, Q^2, \alpha_s, p_s^\perp) + 2 \tan^2 \left(\frac{\theta}{2} \right) \frac{\nu}{M_N} \\ & \left. \times \left[F_{1D}^{\text{eff}}(\tilde{x}, Q^2, \alpha_s, p_s^\perp) + \frac{(p_s^\perp)^2}{2pq} F_{2D}^{\text{eff}}(\tilde{x}, Q^2, \alpha_s, p_s^\perp) \right] \right), \end{aligned} \quad (78)$$

where $\alpha_q = (\nu - |\mathbf{q}|)/M_N$.

2.10.2 MINIMIZING FINAL STATE INTERACTIONS

The IA is an ideal case, particularly for the BONuS12 Experiment, where we desire no interaction between the spectator proton and the hadronic debris created from the γ^* -neutron interaction within the deuteron. We want to minimize any possibility of final state interactions to ensure that the proton we measure has not participated in the reaction.

For any process where final state interactions (FSI) may occur, like the BONuS12 Experiment, it is important to understand and describe quantities relevant to the process. The central quantity describing FSI processes is the distorted momentum distribution [26]

$$n_D^{\text{FSI}}(\mathbf{p}_s, \mathbf{q}) = \frac{1}{3} \frac{1}{(2\pi)^3} \sum_{\mathcal{M}_D} \left| \int d\mathbf{r} \Psi_{1, \mathcal{M}_D}(\mathbf{r}) S(\mathbf{r}, \mathbf{q}) \chi_f^+ \exp(-i\mathbf{P}_s \mathbf{r}) \right|^2, \quad (79)$$

where ξ_f is the spin function of the spectator nucleon and $S(\mathbf{r}, \mathbf{q})$ is the S -matrix describing the FSI between the hadronic debris and the spectator. This S -matrix is

$$S(\mathbf{r}, \mathbf{q}) = 1 - \theta(z) \frac{\sigma_{\text{eff}}(z, Q^2, x)(1 - i\alpha)}{4\pi b_0^2} \exp\left(-\frac{b^2}{2b_0^2}\right), \quad (80)$$

where σ_{eff} is the time-dependent cross section and α is the ratio of real to imaginary part of the forward amplitude. When FSI do not occur $\sigma_{\text{eff}} = 0$, and the usual deuteron momentum distribution is recovered

$$n_D(|\mathbf{p}_s|) = \frac{1}{3} \frac{1}{(2\pi)^3} \sum_{\mathcal{M}_D} \left| \int d\mathbf{r} \Psi_{1, \mathcal{M}_D}(\mathbf{r}) \chi_f^+ \exp(-i\mathbf{P}_s \mathbf{r}) \right|^2. \quad (81)$$

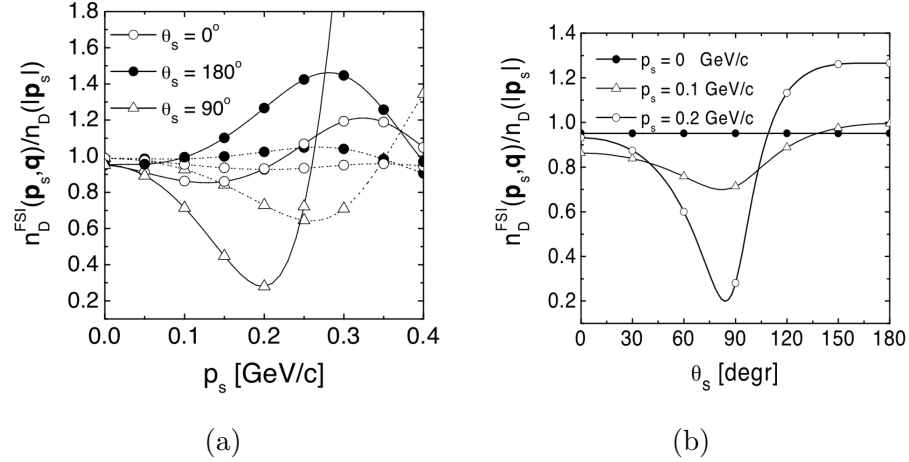


Fig. 13: (a) The Deep Inelastic Scattering ratio n_D^{FSI}/n_D with n_D^{FSI} and n_D , calculated *vs.* the momentum $p_s \equiv |\mathbf{p}_s|$ of the spectator nucleon emitted at different angles θ_s . The full lines correspond to the Q^2 - and z -dependent debris-nucleon effective cross section σ_{eff} , whereas the dashed lines correspond to a constant cross section $\sigma_{\text{eff}} = 20 mb. (b) The Deep Inelastic Scattering ratio n_D^{FSI}/n_D with n_D^{FSI} and n_D , calculated *vs.* the emission angle θ_s of the spectator, for different values of the spectator momentum. Calculations were performed at $Q^2 = 5$ (GeV/c) 2 and $x = 0.2$ for the both graphs.$

To minimize any FSI that may occur in a process like Eq. 69, we look toward the ratio of the distorted n_D^{FSI} to deuteron n_D momentum distributions. When that ratio goes to unity, final state interactions do not exist. Fig. 13a shows that ratio as a function of the spectator proton momentum (p_s) for various angles (*i.e.* $\theta_s = 0^\circ$, 90° , and 180°). The solid lines correspond to Q^2 and z -dependent debris-nucleon effective cross section σ_{eff} , whereas the dashed lines are for the constant cross section $\sigma_{\text{eff}} = 20 \text{ mb}$. From this we see that for momenta below 100 MeV/c, all lines begin to converge to unity.

The plot of the n_D^{FSI}/n_D ratio versus spectator proton scattering angle (θ_s) in Fig. 13b contains lines for three different values of spectator momenta (*i.e.* $p_s = 0$, 100, 200 MeV/c). This plot shows us that for momenta below 100 MeV/c, angles above 100° minimize FSI. Therefore, in order to minimize FSI in the semi-inclusive (*i.e.* detecting some, but not all, particles after the interaction) DIS reaction that occurs in the BONuS12 Experiment, spectators protons with momenta below 100 MeV/c at angles above 100° are detected in coincidence with the scattered electron: $D(e, e', p_s)X$. This allows us to utilize the IA to extract the F_2^n structure function and thus the F_2^n/F_2^p structure function ratio.

CHAPTER 3

THE BONUS12 EXPERIMENT

The BONuS12 Experiment will be conducted at the Thomas Jefferson National Laboratory (JLab) in Newport News, Virginia. JLab was founded in 1984 with the intent of studying the structure of nuclear matter. The unique accelerator that was built at JLab, called the Continuous Electron Beam Accelerator Facility (CEBAF), allowed for the realization of that intent by providing the ability to probe atomic nuclei at the quark level. In order to understand the BONuS12 Experiment, we must first understand CEBAF and the Hall B spectrometer that the BONuS12 RTPC will be installed in. Then we will discuss the RTPC design, components, and construction.

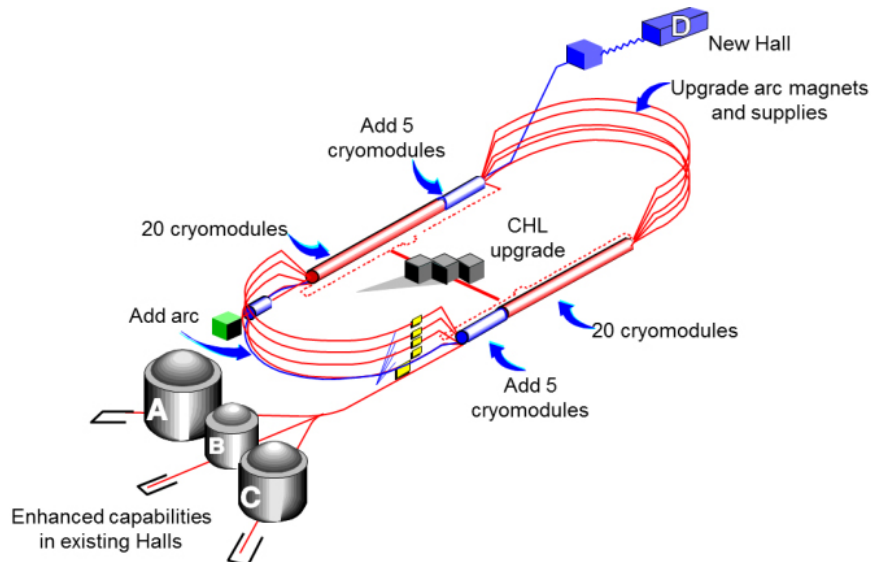


Fig. 14: CEBAF upgraded for the 12 GeV era.

3.1 CONTINUOUS ELECTRON BEAM ACCELERATOR FACILITY

The construction of the Continuous Electron Beam Accelerator Facility (CEBAF) was completed in 1994. It originally consisted of two antiparallel linear accelerators (LINACs) connected by nine recirculation arcs that accelerated electrons to an energy of 6 GeV at a current of up to 300 μ A. In 2004, JLab began an energy upgrade

that would allow CEBAF to supply electrons up to 12 GeV. The same framework used for the 6 GeV accelerator would be used for the 12 GeV era. That is, each pass around the accelerator would increase the energies, which was 1-1.2 GeV/pass during the 6 GeV era [27] and 2.2 GeV/pass after the 12 GeV upgrade. Originally, that meant 5 passes would produce 6 GeV electrons before they were fed into the three existing experimental halls (*i.e.* Hall A, Hall B, and Hall C). In addition to the energy upgrade that increases the energy, a new experimental hall was built (*i.e.* Hall D). That leads to 5 passes creating around 10.5 GeV electron beam to Halls A, B and C. Hall D received electrons from 5.5 passes around the accelerator creating the 12 GeV electron beam energy. As Fig. 14 shows, the upgrade consisted of addition 5 additional cryomodules, an additional recirculation arc, increased capacity of the Central Helium Liquefier (CHL), and improvements in the curving magnet.

The electrons are accelerated in CEBAF by way of the LINACs. These LINACs contain a set of superconducting Niobium accelerating cavities with a magnetic field that oscillates at a frequency of 1.5 GHz. Electrons are injected in bunches into the accelerator with an energy of 45 MeV at the same frequency as the cavities every 0.7 ns. These electrons then circulate around, increasing in energy each pass by the LINACs. Once the desired energy for a given hall is reached, every 2.1 ns magnetic fields inside the arcs force the electrons into specific central trajectories that guides them into that hall. The beam is considered "continuous" because of the high operating frequency at which CEBAF can operate up to its maximum capacity at 200 μ A.

3.2 CEBAF LARGE ACCEPTANCE SPECTROMETER

Once the electrons are accelerated to a desired energy, they are received by the halls, where they enter each hall's spectrometer. A spectrometer is just an instrument (or collection of instruments) that measure and analyze a range (or spectrum) of processes or reactions. Because BONuS12 will operate in Hall B, here we will focus on the components and operation of Hall B's spectrometer, called the CEBAF Large Acceptance Spectrometer at 12 GeV (or CLAS12). As the name suggests, CLAS12 is an evolution of CLAS6 (or just CLAS as it was known before talk of the energy upgrade), which was the original spectrometer built for Hall B.

CLAS12 (see Fig. 15) consists of two major groups of detectors, which together allow for detection and identification of particles over a large scattering angle, thus

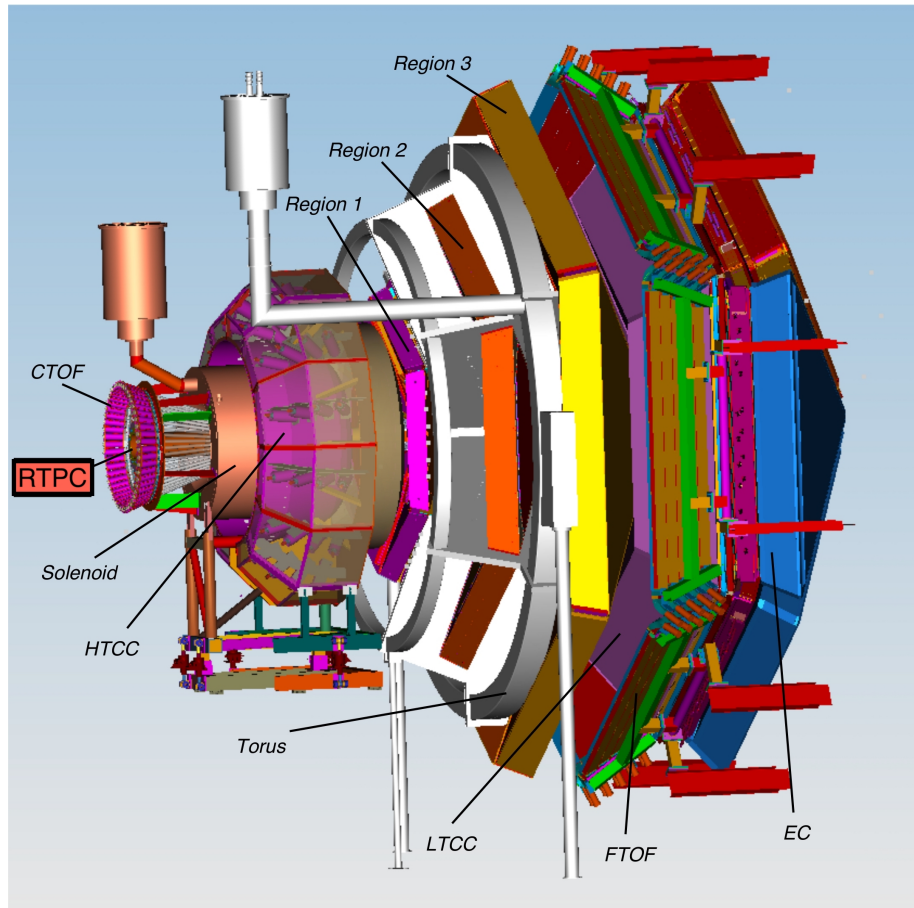


Fig. 15: The CEBAF Large Acceptance Spectrometer at 12 GeV (CLAS12).

the “Large Acceptance” in the name CLAS12. The Forward Detector (FD) covers scattering angles of between 5-40 degrees, and consists of a torus magnet, Cherenkov counters, a time of flight detector, drift chambers and electromagnetic calorimeter. The other group of detectors is known as the Central Detector (CD), and covers scattering angles between 40-125 degrees. The CD consists of a solenoid magnet, time of flight detector and finally, the BONuS12 RTPC. We will discuss each of these detectors, with a bit more focus on the RTPC.

3.2.1 TORUS MAGNET

The torus magnet is comprised of six superconducting coils arranged symmetrically around the beamline to create a azimuthally-symmetric magnetic field up to 3.5 T. The coils are cooled to an operating temperature of 4.5 K by liquid helium.

The shape of the coils was designed to create a field that increases near the center, which provides the desired resolution as a function of θ .

The purpose of the magnetic field is to curve the tracks of charged particles without changing their azimuthal (ϕ) angle. This curvature allows for the increased capability of particle identification. Its open structure allows for long path lengths for both charged and neutral particles, which also contributes to particle identification through time-of-flight measurements.

3.2.2 CHERENKOV COUNTERS

When a charged particle moves through a dielectric¹ with a speed greater than the phase velocity of light in that medium, electromagnetic radiation (*i.e.* light) is emitted. This is known as Cherenkov radiation. By changing the refractive index of that medium, the threshold for emission of that light is modified. This effect allows for the distinction of particles otherwise having the same energy and momentum. By using a material with a specific refractive index, a heavier particle may not produce Cherenkov light, but a lighter particle may.

CLAS12 contains two detectors that exploit this Cherenkov effect. The High Threshold Cherenkov Counter (HTCC seen exploded in Fig. 16) is between the solenoid and the first region of the Drift Chambers. It discriminates electrons and pions by being filled with CO₂. This gas has an index of refraction $n = 1.00041$, which forces pion above 4.6 GeV to produce light. If the particle has an energy below this threshold and it produces light, it is an electron.

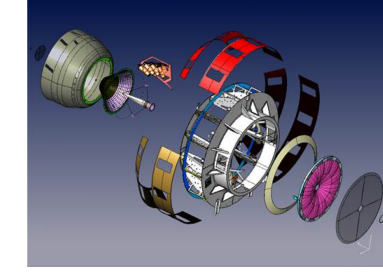


Fig. 16: The High Threshold Cherenkov Counter.

The other Cherenkov detector is the Low Threshold Cherenkov Counter (LTCC), which sits between Region 3 of the Drift Chambers and the Forward Time of Flight detector. It is filled with C₄F₁₂, which allows for the discrimination of pions and kaons at the 2.6 GeV where only pions produce Cherenkov light.

¹A dielectric is any insulator that can be polarized when an electric field is applied.

3.2.3 DRIFT CHAMBERS

There are three regions of Drift Chambers (DC) that collectively allow for the reconstruction of charged particle trajectories. The first region is located in front of the Torus Magnet out the reach of the field. Region 2 is between the coils in the high field region. The third region is after the Torus, but feels a small magnetic field from the coils. Each region is made of six triangular sectors, which are made of small wires and filled with a gas mixture that exploits the process of ionization.

Within the sectors of the DC there are hundreds of wires, half of which are positive and the other half negative. When a charged particle travels through the gas mixture (90% Argon 10% CO₂ for the case of the CLAS12 DC), it knocks off electrons from the gas molecules as it passes. This process is known as *ionization*. In the DC, these ionization electrons that are created as charged particles pass through are accelerated to the nearest positive wire from the electric field created by the negative-positive wire pairs. The ion created is accelerated toward the nearest negative wire by the same electric field.

Using the signals created by the electron-ion pairs as the charged particle travels through the regions of the DC allows for the reconstruction of that particle's path. This information lends itself to the reconstruction of the particle momentum as well as its vertex (*i.e.* where the particle collision occurred). This information will be vital in BONuS12 for identifying the electron created in the $eD \rightarrow e' p_s X$ process.

3.2.4 FORWARD TIME OF FLIGHT

Two charged particles having the same momentum will travel at different speeds depending on their mass. The Forward Time of Flight detector (FTOF) will measure the time of arrival of those charged particles emerging from the target. Primarily, the FTOF will help separate between pions and kaons for energies below 3 GeV. Higher energies are handled by the Cherenkov counters. Because higher momentum particles scatter at lower angles, the FTOF was constructed to have better timing resolution at lower angles. That resolution can be as small as 80 ps at the more forward angles and 150 ps at larger angles (*i.e.* over 35 degrees).

The FTOF is made of six sectors of plastic scintillators coupled to double-sided PMT readout. Within each sector, there are three arrays of counters. Panel 1a, which covers 5 to 35 degrees in θ contains 23 counters. Panel 1b also covers angles

between 5 and 35 degrees and contains 62 counters. Finally, Panel 2 has 5 counters covering only angles between 35 and 45 degrees.

3.2.5 ELECTROMAGNETIC CALORIMETER

Electromagnetic calorimeters measure the energy of particles traveling through it that interact via the electromagnetic interaction. The EC in CLAS12 contains three layers. The preshower calorimeter (PCAL) is the first layer and is used to identify two close gammas, which will help discriminate between neutral pions and single gammas. The next two layers are the inner and outer electromagnetic calorimeters (IC and OC, respectively). Both are used collectively with the PCAL to identify electrons, photons, $\pi^0 \rightarrow \gamma\gamma$, and neutrons.

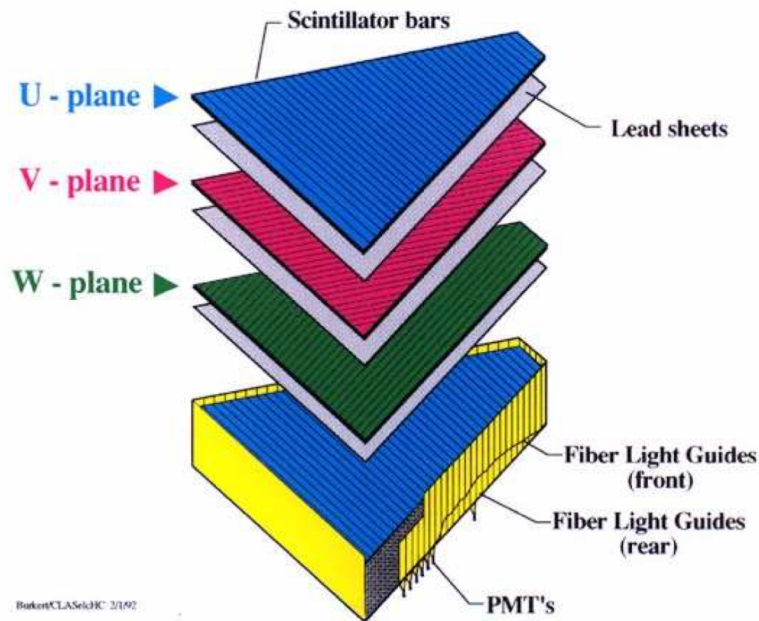


Fig. 17: Exploded view of a sector of the Electromagnetic Calorimeter (EC) for CLAS12. [5]

The requirements of the EC are to identify the electrons with energies above 0.5 GeV, and measurements of photons above 0.2 GeV helping to reconstruct π^0 and η particles through their neutral decays. The EC can also provide photon/neutron separation by utilizing TOF information available.

Each layer of the EC is comprised of six triangular sectors. Each sector is made of alternating layers of scintillators strips and lead sheets. The spatial-coordinate

readout comes from the three planes (U, V, and W) seen in the exploded view of one sector in Fig. 17, which each contain 36 scintillator strips that run parallel to one side of the nearly equilateral triangular sectors. Strips are rotated by 120° in each successive layer, which allows for effective translation to x, y, and z coordinates.

3.2.6 SOLENOID MAGNET

The solenoid magnet and the remaining two detectors to follow (*i.e.* the Central Time of Flight and Radial Time Projection Chamber) are all members of the group known as the Central Detector. The Solenoid is a super-conducting magnet cylindrical in shape that surrounds the beam line. It is capable of producing a field of up to 5 T along the beam line. Charged particles experiencing this field curve in a helical trajectory, which allows for reconstruction of those trajectories and discriminates between charged and neutral particles.

The other purpose of the solenoid is to shield the Forward Detector from electron-electron collisions, called Møller electrons. Because the field is strongest closest to the target, most Møller electrons originating from the beam line are isolated by the solenoid's field to small polar angles (θ) where none of the FD materials exist. The other means of protection from these Møllers comes from a shield around the beam line located just after the Central Detector as well as a shield just in front of a small detector called the Forward Tracker, which for the BONuS12 Experiment will be turned off.

3.2.7 CENTRAL TIME OF FLIGHT

The Central Time of Flight (Fig. 18), just as the FTOF, measures the time of flight of particles originating at the reaction vertex. It is made of 48 scintillator bars that form a barrel and spans polar angles of 35° to 125° that surround the target with full azimuthal coverage. The scintillators are coupled on each end by magnetic-field-sensitive PMTs, which are positioned out of the solenoids field by long light guides. The resulting CTOF operates with a time resolution of 60 ps, which was the requirement for particle identification.

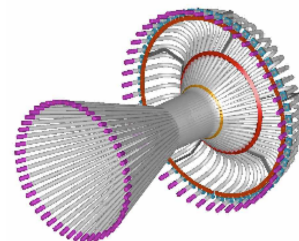


Fig. 18: The Central Time of Flight Detector.

3.3 BONUS12 RTPC

During Run Group F (RGF) in Hall B at JLab all of the detectors just described will be present in addition to one more that will be located inside the solenoid magnet whose outer limits end just before the CTOF. That detector is the BONuS12 Radial Time Projection Chamber (or RTPC). Its purpose is detect protons by way of ionization electrons created as protons pass through the RTPC.

3.3.1 COMPONENTS AND THEIR PURPOSE

Accelerated electrons that enter Hall B hit the RGF target. That target measures 3 mm radially is filled with gaseous deuterium at 7 atm pressure surrounded by a 65 μm thick Kapton wall. When an electron collides with the neutron in a deuteron atom, it continues in the forward direction into the Forward Detector of CLAS12. That collision also results in the ejection of a proton that drifts radially outward into the RTPC.

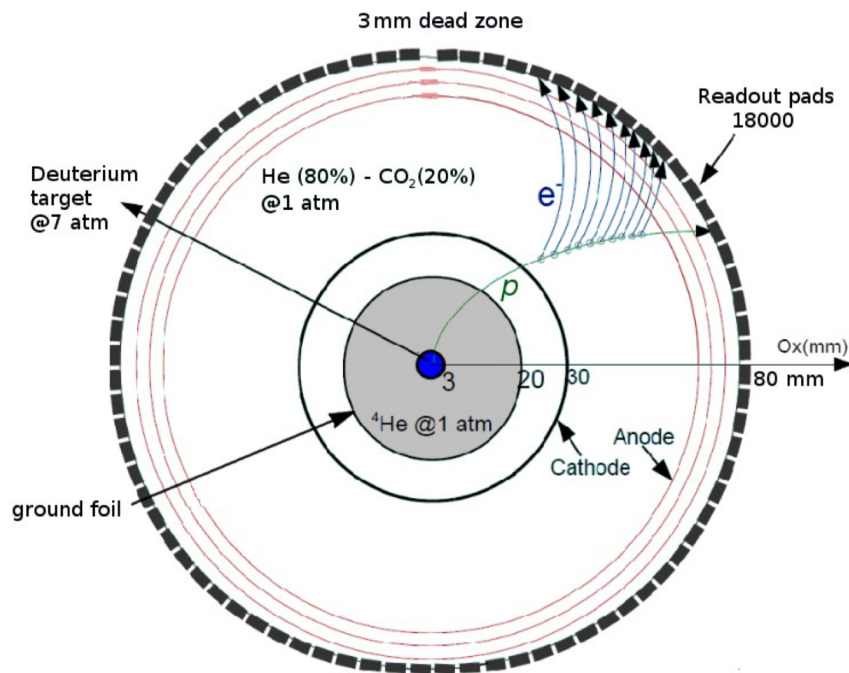


Fig. 19: Cross section of the RTPC showing a proton traversing the detector with ionization electrons drifting toward the readout pad board.

That proton is guided toward the outer edge of the RTPC by way of an electric field created within it. That field is established with a ground foil at 2 cm and a

cathode foil at 3 cm (see Fig. 19). The cathode foil is given a high negative potential and the ground foil is inherently at zero potential. This potential difference creates that electric field through the active region of the RTPC, which begins at the cathode foil and ends at the first Gaseous Electron Multiplier (GEM) foil.

This active region is where the proton will create ionizations along its path outward. This region is filled with a gas mixture of 80% Helium and 20% CO₂, which was chosen for its fast drift times and minimal drift angle (more about this in Section 4.3.4). Because of the magnetic field created by the solenoid, the proton curves in one direction as it moves outward while the ionization electrons it creates curve in the opposite direction due to their opposite charge.

Every time an ionization electron is created, it is also driven by the electric field toward the outer edge of the RTPC where readout pad board waits for its arrival. However, because a single electron cannot be easily readout, that electron will encounter three layers of GEM foils at 7 cm, 7.3 cm and 7.6 cm. Those GEMs are used to amplify the number electrons from one to something significant enough to register on the electronics. Each GEM has a gain of about 100, which means that through three GEM layers, one electron could become 10,000 after exiting the last layer.

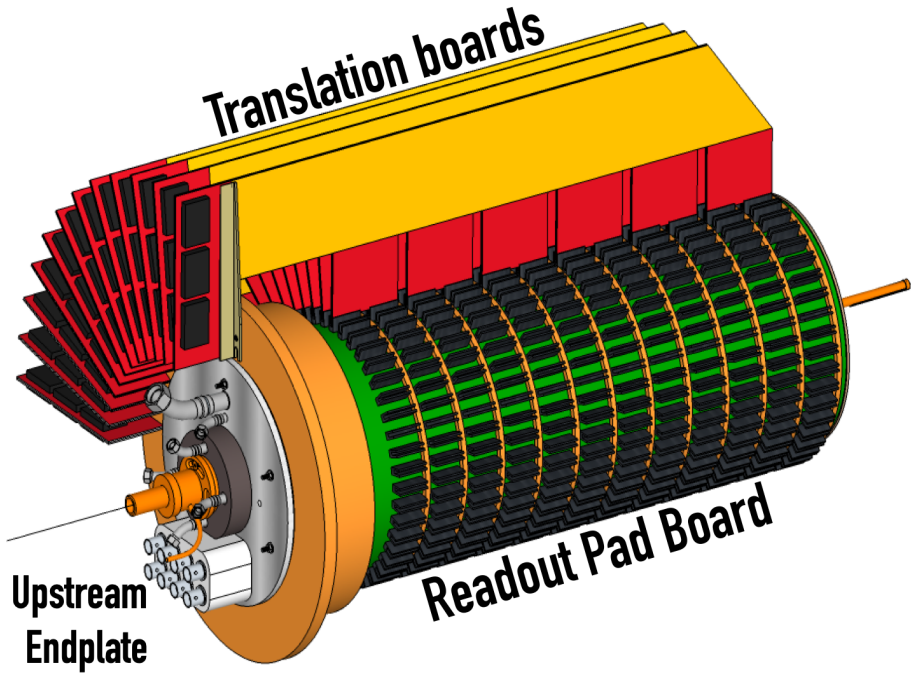


Fig. 20: Design of the RTPC with only one-quarter of the translation boards attached.

Once this avalanche of electrons has been created by the GEMs, their final destination is the read out pad board at 8 cm. The pad board has 180 pads around ϕ by 96 pads in z totaling 17,280 readout pads. These pads, coupled to translation boards that act as current-limiting adapter boards, read the signal that the electron avalanche makes. The electronics then drives the signal to the data acquisition system, which stores the data for analysis.

3.3.2 BONUS12 RTPC DRIFT-GAS MONITORING SYSTEM

The drift velocity of electrons in the RTPC is very sensitive to fluctuations in the gas-mixture and potential, as well as the temperature and pressure of the gas in the active region (see 4.3.4). Therefore, a system was designed that monitors the drift velocity of electrons in the gas mixture of the active region in the RTPC. To achieve this, a small drift chamber was designed whose gas mixture would come from downstream of the RTPC.

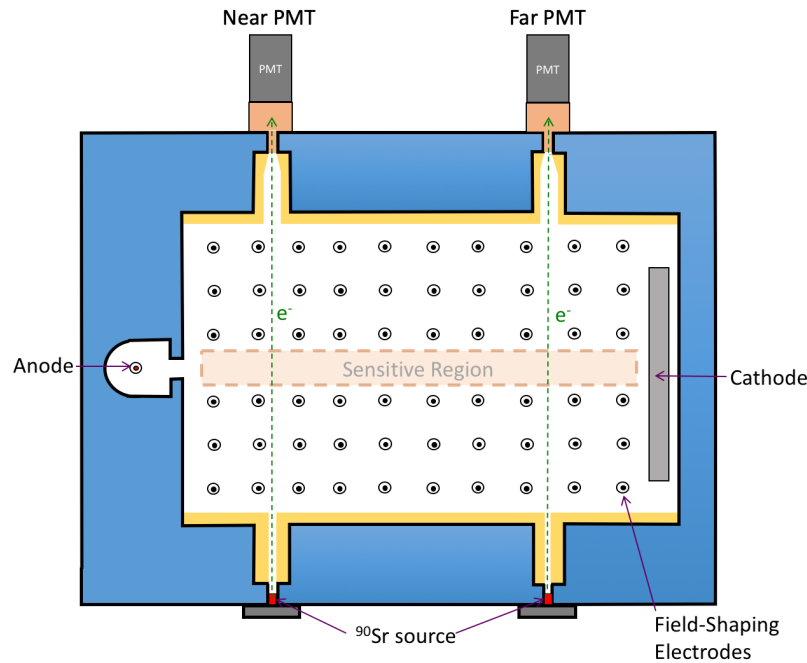


Fig. 21: Design concept of the Drift-gas Monitoring System (DMS) for the BONuS12 Experiment.

Since the purpose of this Drift-gas Monitoring System (DMS) is to measure the drift velocity within the gas mixture, the focus of the DMS design was measuring that velocity through a near-constant electric field. The design concept (seen in Fig.

21) is a drift chamber where two sources at a known distance between them emits β electrons up to associated scintillator/photomultiplier tubes (PMTs). When these electrons travel through the gas, they create ionization electrons along their path. Within a sensitive region in the center of the DMS, those ionization electrons are guided to an anode wire behind a small slit in a grounded plate by an electric field.

The electric field that guides the ionization electrons to the anode is created by a cathode with a high negative potential, an anode with a high positive potential, and field-shaping electrodes that have potentials stepped down by equal amounts from a voltage-divider circuit. This ensures the field within that sensitive region is uniform, so no unwanted acceleration of electrons occurs between the two sources.

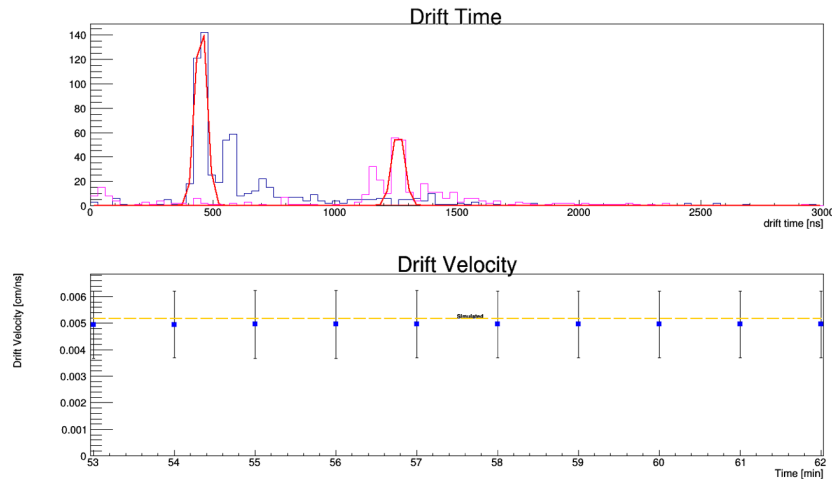


Fig. 22: Monitoring output of the DMS.

When a source β electron is detected by either PMT, a Time-to-Digital Converter (TDC) looks for an associated ionization electron at the anode. When a signal on the anode is seen, the TDC adds that drift time to a histogram. As enough statistics populate the histogram, two peaks are formed from the drift of electrons from the two sources and then a difference in the two times can be calculated. Given the known distance between the sources and the time difference between the two peaks, the drift velocity is calculated. Then the drift velocity is plotted versus elapsed time, giving a means to monitor that velocity (see Fig. 22 for those plots from DMS testing).

3.3.3 CONSTRUCTION AND INTEGRATION

The construction of the BONuS12 RTPC began at Hampton University in Hampton, Virginia around 2017. Because of the cylindrical shape of the detector, mandrels were used widely in the shaping of the detector components. The ground foil, cathode foil, the three layers of GEM foils, and pad board were all assembled using mandrels. Fig. 23 is a drawing of the assembly station for the RTPC, which includes an actuator that removes wrapped foils from the mandrel and places them into the detector on the assembly station.

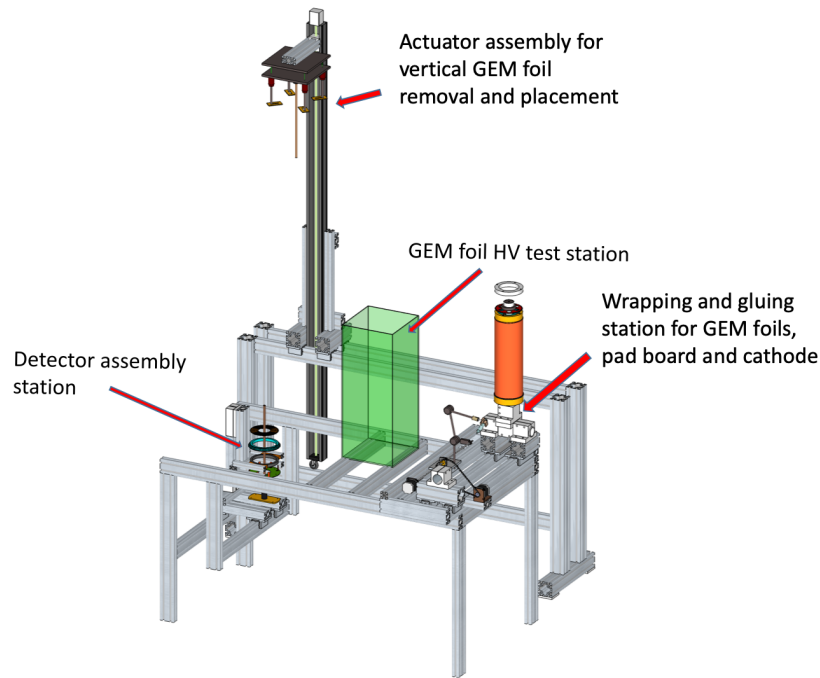


Fig. 23: Assembly station for the RTPC.

The first assembled detector was delivered to JLab in November 2019. The Drift-gas Monitoring was also delivered to JLab in November 2019. Both are undergoing testing in the Experimental Equipment Lab (EEL) with the full array of components that will be installed in the Experimental Hall (*i.e.* RTPC, gas panel including the DMS, DAQ, etc). Once that testing is complete, in late January 2020 the BONuS12 RTPC will be installed in Hall B. Run Group F, of which the BONuS12 Experiment is a part, will also require the installation of three layers of the Forward Micromegas Tracker, switching the Forward Tagger to the FTOff Møller Shield, as well as cabling for all of those installed detectors. Once this is complete, cosmic ray testing will

begin. This will allow for the first data stream of the RTPC from within the CLAS12 Data Acquisition System whilst inside the hall. Then on 12 February 2020, Run Group F will begin and BONuS12 will begin taking data.

CHAPTER 4

SIMULATION AND DEVELOPMENT

The simulation and development of the BONuS12 experiment has been ongoing essentially since the original BONuS6 experiment in the early 2000's. The goal of BONuS has always been to detect low momentum spectator protons in coincidence with scattered electrons at high Bjorken-x. This is the purpose of the simulation and development (*i.e.* to optimize a detector that will result in high statistics in the relevant kinematic range).

This chapter will focus on the methods used in that detector optimization in preparation for the BONuS12 experimental run. It will cover simulations done to improve geometry, determine electron drift time, and understand energy loss through detector components. The chapter will also go over the construction of the detector. Finally, the process of reconstruction will be covered, which is the way we ultimately determine the kinematics of each event in order to recover the structure functions we are interested in.

4.1 GEANT4 MONTE CARLO (GEMC)

Much of the simulations done in preparation for and during CLAS12 experiments use the Geant4 Monte Carlo (GEMC) software developed by Maurizio Ungaro at Jefferson Lab. GEMC, as the name indicates, uses a toolkit called Geant4. Geant4 was developed by CERN. It was released as a successor in the GEANT software toolkit series, first released in 1998. Since then Geant4 has involved an international collaboration of contributors and maintainers with applications ranging from nuclear physics to medical physics.

The purpose of the Geant4 toolkit is to simulate the passage of particles through matter. This can mean anything from particles going through biological material (*e.g.* simulating the effects of radiation on human tissue) to simulating particles moving through detectors, which will clearly be of much interest to us here. In order to understand how the BONuS12 experiment simulations were conducted with GEMC, first we must become a little more familiar with Geant4.

Geant4 uses the object-oriented programming language C++ in various facilities to exploit its features. The first defining characteristic of this toolkit is its ability to define geometry, or physical layout, of an experiment. This lets us consider how this geometry effects the particles moving through the materials in the experiment. The path that these particles takes as well as the interactions with the materials they pass through is another facility in Geant4 known as tracking.

The Geant4 Monte Carlo (GEMC) is a C++ framework that utilizes Geant4 and the Monte Carlo method of randomized sampling in order to obtain particle behavior through materials. At a very basic level, GEMC can define particle momenta and angles as well as detector geometry and material in order to understand the particle's behavior in that material. One can define a variety of output variables of interest in these simulations like total energy deposited, position, or momentum. There is much more that can be done with this simulation platform that will be discussed through the following sections. First, we must go over one more tool that was used for simulations called Garfield++.

4.2 GARFIELD++

While Geant4 and GEMC both deal well with the simulation of particles' interaction with matter, the particles of interest in the BONuS12 experiment also go through gases and will be under the influence of electric and magnetic fields. For a more specialized simulation of charged particles in such gases with electric and magnetic fields, we use a toolkit called Garfield++, which was developed at CERN. This is extended version of the original Garfield platform that incorporates MagBoltz in the C++ language. MagBoltz solves the Boltzmann transport equations for electrons in gas mixtures under the influence of electric and magnetic fields. This allows Garfield++ to simulate electrons traveling in a gaseous medium under the influence of electric and magnetic fields. The other programs utilized to create a mesh of the RTPC and solve the electromagnetic equations inside the RTPC are GMSH and ElmerSolver, respectively. These packages and their purpose will be described more in the discussion of drift electrons as well as gas-mixture optimization.

4.3 BONUS12 RTPC SIMULATIONS

Throughout the next section, we will focus on the simulations that shed light on particle behaviors in the detector, drove optimization efforts, and offered insight

about expected results. We'll go over all the tools that were used for the simulations and how each one was utilized and implemented. Computer simulations are immensely powerful and tend to be much less expensive than physical exploration and experimentation. We'll discuss how the packages already presented can come together to simulate the entire BONuS12 Experiment from the RTPC to its inclusion in the CLAS12 detector.

4.3.1 GEOMETRY & MATERIALS

The first thing to do when simulating the BONuS12 RTPC in GEMC is to define its geometry and materials. This is done via Perl file, where one can use predefined materials from Geant4 (*e.g.* G4_KAPTON for Kapton, G4_Cu for copper, etc.) or define your own materials. Geometries are defined both in Geant4 and GEMC by solid types like "tube", "box", "sphere", etc. Since the BONuS12 RTPC is made of several different cylinders, most of the geometry definitions are of type "tube". Therefore, we specify the dimensions in terms of r , ϕ and z . For example, the drift volume is defined in the code by

```
$detector{"name"} = "sensitive_drift_volume";
$detector{"mother"} = "rtpc";
$detector{"description"} = "Sensitive drift volume";
$detector{"color"} = "ff88994";
$detector{"type"} = "Tube";
$detector{"dimensions"} = "$rmin*mm $rmax*mm $z_half*mm $phistart*deg
$pspan*deg";
$detector{"material"} = $mate;
$detector{"style"} = 1;
$detector{"sensitivity"} = "rtpc"; ## HitProcess definition
$detector{"hit_type"} = "rtpc"; ## HitProcess definition
print_det(\%configuration, \%detector);
```

where the material (`$mate`) is made of 80% ${}^3\text{He}$ and 20% CO_2 in this case (defined elsewhere) and `$rmin= 30.0`, `$rmax= 70.0`, `$z_half= 192.0`, `$phistart= 0.0`, `$pspan= 360.0`. One defines the units within the declaration of `$detector{"dimensions"};` `$rmin*mm` would be 30.0 mm, for example. There are other variable names that you see within the detector attributes above that are important to understand. The

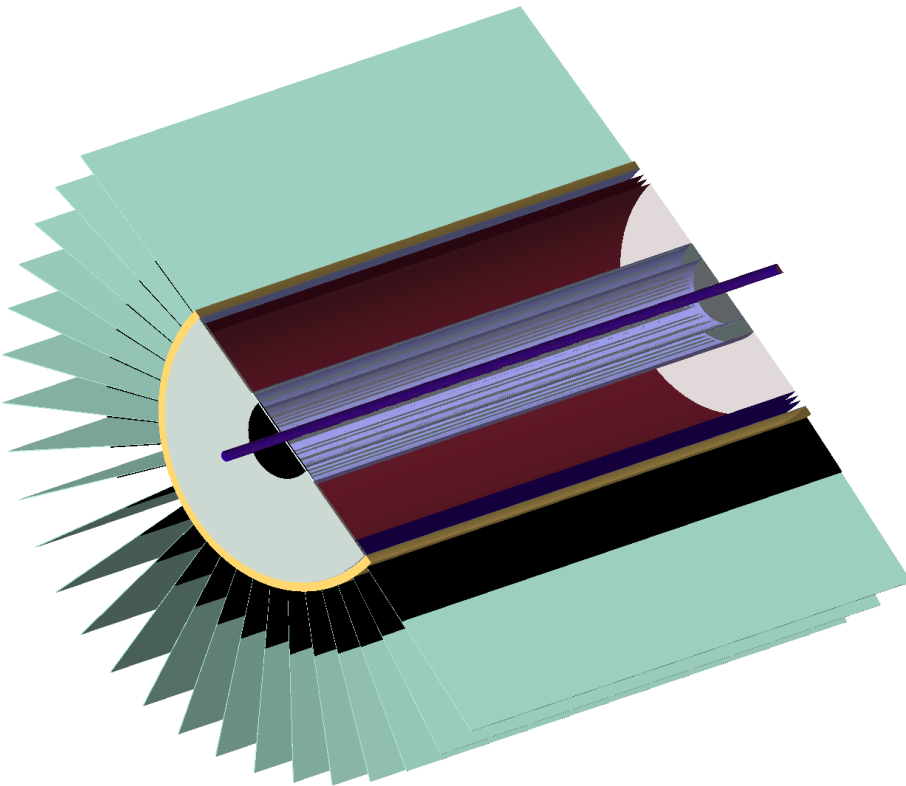


Fig. 24: BONuS12 RTPC geometry implemented in GEMC

variable `style` describes whether the type is a solid (`style = 1`) or wire frame (`style = 0`). The `sensitivity` variable directs GEMC to add the output of this region to the correct bank in the output file. In order to define what particle-interaction output variables appear in the output file for the given volume, we use the `hit_type` variable. Hit type will be covered more in Section 4.3.3 when we discuss what to do when ionization occurs in the drift region.

Not all of the RTPC details can be implemented into GEMC, so we only include the important components in the GEMC simulation. Those components include the main detector parts like the target, ground and cathode foils, GEM foils, and readout pad-board. Then there are the components that had to be included in order to understand their effect on the particles that may be traveling through them (*e.g.* down-stream end plate, electronics and translation boards, support ribs and spines,

etc). Most of these secondary components had to be simplified in order to save time during the simulation process. For example, a cylindrical volume of average density was included outside of the readout pad-board. This density included a proportional amount of the support ribs and spines, electronics, and air. The final geometry can be seen in Fig. 24, which shows half of the RTPC in order to see the internal structure.

Once the geometry is set up for the RTPC, it must be inserted within the CLAS12 detectors in GEMC. The file that brings all these detectors together in GEMC is an XML (*i.e.* extended markup language) file called a *gcard*. This file is where one defines not only which detectors to include in the simulation, but also what variables to include in the output file and what the incoming particle beam should be (*e.g.* momentum, angle, spread, etc.). For example, if one desired 10.6 GeV/c electrons to travel at 0° scattering angle θ and 0° around ϕ , with a spread of ± 10 MeV/c in momentum, $\pm 10^\circ$ in θ and $\pm 180^\circ$ in ϕ , the code would be:

```
<option name="BEAM_P" value="e-, 10.6*GeV, 0.0*deg, 0.0*deg"/>
<option name="SPREAD_P" value="10*MeV, 10*deg, 180.0*deg"/>
<option name="BEAM_V" value="(0, 0, 0)cm"/>
<option name="SPREAD_V" value="(0.3, 20)cm"/>
```

Notice that in this code snippet, the vertex of the particle `BEAM_V` is set to zero and there is a spread on that vertex `SPREAD_V` of $0 \text{ cm} \leq r \leq 0.3 \text{ cm}$ and $-20.0 \text{ cm} \leq z \leq 20 \text{ cm}$), which spans the diameter and length of the BONuS12 RTPC target.

This method of generating particles makes use of GEMC's internal event generator. The particles that can be generated make use of the Geant4 particle bank. The trouble with this internal generator is that we don't have access to multiple particles that we may want to examine (*i.e.* secondary particles). For that we have to look toward another method of generating particles and how to import that file into GEMC.

4.3.2 EVENT GENERATOR

For the purpose of our GEMC simulations in BONuS12, we are primarily concerned with the reaction $eD \rightarrow e'pX$ and so we need a means of generating such events. For that we use an external particle generator called Pythia. Pythia is a program for generating high-energy physics events, which is precisely what we need. It uses theory and models on collisions between particles like e^- , e^+ , p and \bar{p} (*i.e.*

anti-proton) to generate output in a file format name Lund, after the University where the program was developed.

TABLE I: Lund file header

Column	Quantity
1	Number of particles
2	Mass number of the target
3	Atomic number of the target
4	Target polarization
5	Beam Polarization
6	Beam particle type
7	Beam energy (GeV)
8	Interacted nucleon ID (proton or neutron)
9	Process ID
10	Event weight

This Lund output file format has very specific variables that we can take advantage of in GEMC. The first line of this Lund file contains header information for the particles to follow from the collision simulation. This header contains 10 different columns, listed in Table I. The items in bold are used by GEMC. Given the number of particles listed under column 1, there will be a list below the header with particle details for each (see Table II). That is, if there is a 5 listed under the first column in the header, then below the header will be 5 lines for each of the particles. For a simulation with multiple events, subsequent events appear after the last particle of the previous beginning again with the header line.

For the BONuS12 experiment, the event generator created a Lund file with various electron-proton deep-inelastic collisions that we must run through GEMC. To do this, instead of utilizing the GEMC internal event generator, we include the following line of code

```
<option name="INPUT_GEN_FILE" value="LUND, even_gen.lund"/>
```

in the gcard that we use to give direction to GEMC. This file will serve to instruct GEMC how many particles are in each event and the type of particle, its momentum and its vertex. For our purposes in BONuS12, we have Lund files with primary

TABLE II: Lund particles

Column	Quantity
1	Index
2	Lifetime [nanoseconds]
3	Type (1 is active)
4	particle ID
5	Index of the parent
6	Index of the first daughter
7	momentum x [GeV]
8	momentum y [GeV]
9	momentum z [GeV]
10	Energy of the particle [GeV]
11	Mass of the particle [GeV]
12	vertex x [cm]
13	vertex y [cm]
14	vertex z [cm]

electron-proton events that also have a number of additional protons that serve as background. The number of these background protons can vary, but the intent is always to best represent what we would expect to see. Once we run this file through GEMC with all the other variables defined that have been previously discussed, we need to take a look at what happens in the simulation when these protons travel through the RTPC.

4.3.3 DRIFT ELECTRONS

When protons travel through the sensitive region of the RTPC, they ionize the gas creating what are known as ionization electrons. Because of the electric field within that sensitive region, those ionization electrons drift toward the outer edge of the RTPC to the readout electronics. The other thing that happens to protons traveling through the RTPC is that they bend in a helical pattern because of the magnetic field. The ionization electrons that are created also bend, but in the opposite direction of

the protons because they are oppositely charged.

By how much these charged particles bend when moving through the magnetic field created by the solenoid magnetic depends, in part, on the magnitude of that field throughout their path. Therefore, it is very important to get an accurate map (*i.e.* the magnitude and direction of the field at small steps in space around the magnet) of that magnetic field. This is important for both the generation of simulated data and the reconstruction of real data. For the simulated data, the field map will define the path of both protons and ionization electrons within GEMC. For the real data, it will play a role in the reconstruction of kinematics from events.

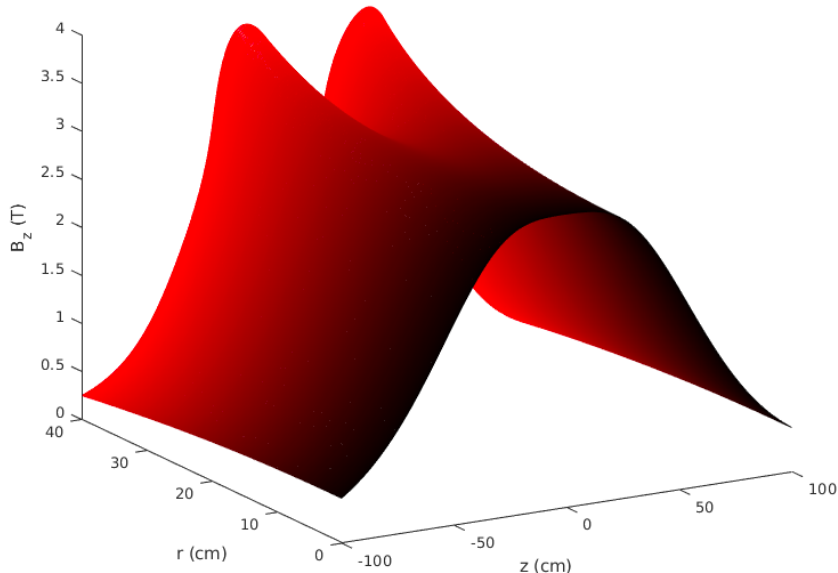


Fig. 25: CLAS12 Solenoid Field Map (V.Lagerquist)

The field map for the solenoid magnet in CLAS12, in which the BONuS12 RTPC will reside, is mapped in steps of z and r (symmetric in ϕ) by Victoria Lagerquist at Old Dominion University (see Fig. 25). Within the sensitive region of the RTPC (*i.e.* $3 \text{ cm} \leq r \leq 7 \text{ cm}$), the map looks like Fig. ?? in steps of z within the RTPC. The map itself takes as input course measurements of the B-field inside the solenoid and finds a more finely-structured field to use in other applications. One of those applications is the simulation of protons traveling through the RTPC.

While GEMC does an acceptable job simulating the proton tracks, Garfield++

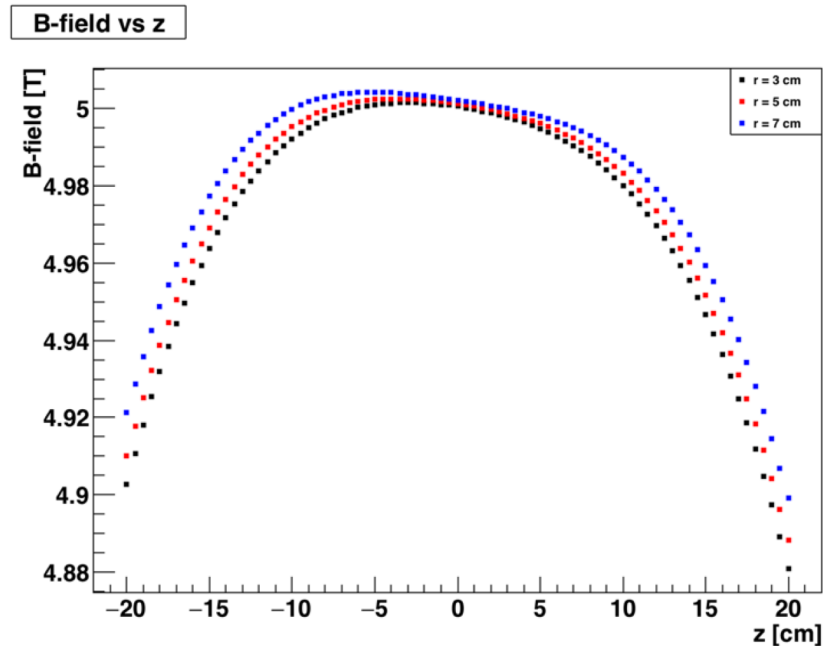


Fig. 26: Magnetic field strength versus z for values of r .

has a more specialized capacity to simulate the ionization electrons (also called drift electrons) created by the protons as they interact with the gas mixture as well as the electric and magnetic fields that are present in the sensitive region of the RTPC. The available build of Garfield++ does not allow for a magnetic field map to be imported, so it had to be written in as a custom feature.

By starting electrons at different values of r throughout the sensitive region (*i.e.* $3 \text{ cm} \leq r \leq 7 \text{ cm}$) and using known values of the electric and magnetic fields, Garfield++ calculated the time it takes that electron to reach the outer edge of the RTPC (*i.e.* 8 cm) as well as the change of angle that it makes. By defining more than one electron for Garfield++ to simulate, we can fit the results to a Gaussian to find the mean and sigma. Those means serve as points in the figures to follow of drift time and drift angle and the sigmas define the diffusion that occurs. As we will see in the coming sections, these drift times and drift angles are of crucial importance to the BONuS12 experiment.

4.3.4 GAS OPTIMIZATION

One of the first uses for the drift time and drift angle from Garfield++ is to

optimize the gas mixture that will be used in the sensitive region of the RTPC. We want a fast drift time to ensure our electronics are able to handle the signal. This would also be less demanding on the trigger and usually means less diffusion. The other property to minimize, drift angle, would ensure that our track is discernible from others in the detector at the same time. Along this line is the need to minimize the diffusion in that occurs within the RTPC in order to increase the resolution of the hits. Thus, we need a gas mixture is that is fast, with small drift angle and diffusion properties, but with a high number of primary ionization events to reconstruct the track.

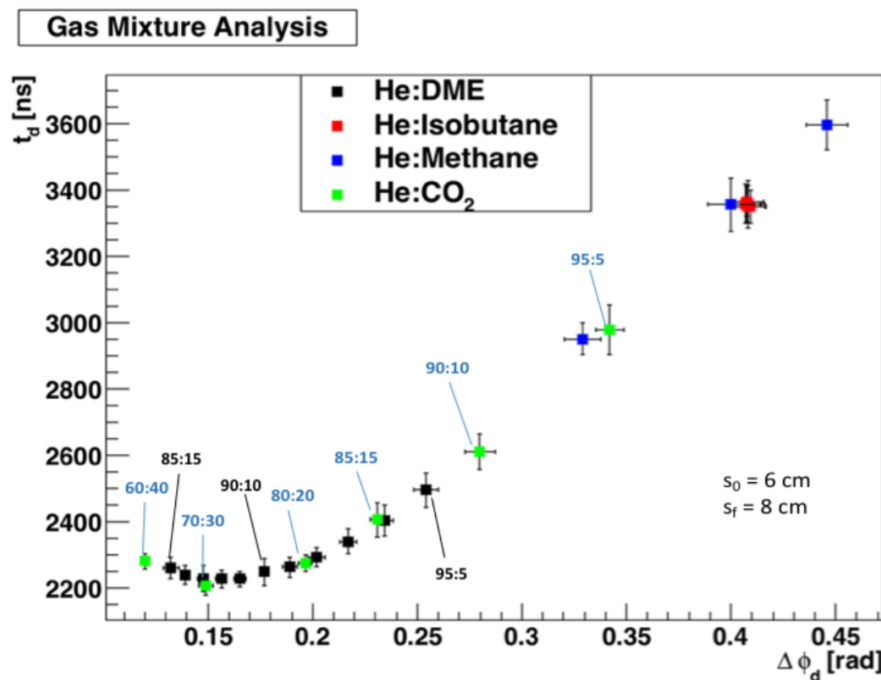


Fig. 27: Drift angle vs drift time for various gas mixtures

The purpose of mixing gases is two-fold. First, there must be a primary gas where primary ionization occurs. Typically this is chosen to be a noble gas such as helium, neon, and argon. A noble gas is usually the primary gas because the outer electron level of the molecule is full, meaning the gas would not interact with the walls of the detector. Also because the outer level is full, the probability of capturing a drift electron is low (i.e. they have a low electron affinity). Second, in order to prevent secondary effects such as photon feedback¹ and field emission², there must exist

¹ Secondary avalanches created from decay through photon emission of excited primary gas atoms.

²Electrons emitted from an electric field.

another gas to act as a quencher. This quencher gas is used to create a stable gas mixture that creates a signal well separated from noise of the electronics.

The first goal is to identify the type of quencher. Fig. 27 shows the drift time as a function of the drift angle of four gas mixtures in a sensitive region containing an electric field of 625 V/cm starting from 6 cm and ending at 8 cm. This electric field corresponds to a potential of -2500 V within the sensitive region, which is high enough to move ionization electrons to the GEMs, but lower than the breakdown potential of the gas (more about this in a few paragraphs). These initial and final radii were chosen to gather results quickly. The error bars on these points are the sigmas of the Gaussian fits of the histogram and represent the diffusion properties of the mixture.

All ratios of He-Isobutane result in almost identical drift angle and drift time. The He-DME starts with a ratio of 85:15 on the far left of Fig. 27 and goes to 100:0 on the far right. The mixture of 87:13 He:DME is at the minimum of the curve. Ideally, as in the original BONuS6 experiment, we could chose this He-DME mixture. However, in an effort to chose a non-flammable gas, we decided to take a look at He-CO₂ mixtures.

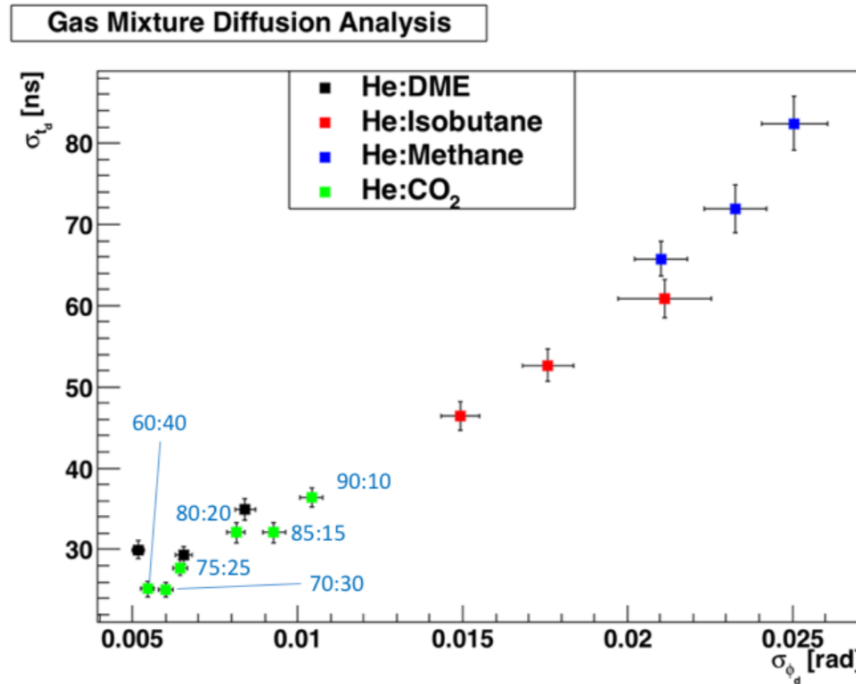


Fig. 28: Diffusion in drift angle vs diffusion in drift time for various gas mixtures

In Fig. 27, the He-CO₂ mixture is in green with the ratios labeled in blue. The

70:30 mixture is at the minimum drift time, which certainly meets the criteria for BONuS12. One of the characteristics that we need to identify during a run is when there may be slight changes in the gas mixture. If we chose to be at the minimum, then identifying when a change occurs would be difficult. This is because while there may be a change in drift angle as the ratio changes, at the minimum there the drift time changes are on the order of nanoseconds. If 80:20 is chosen, then we could more easily identify if a change happens during a run by the noticeable change in both drift angle and drift time. For this reason as well as its non-flammability, the best choice of a gas mixture would be 80%:20% He:CO₂.

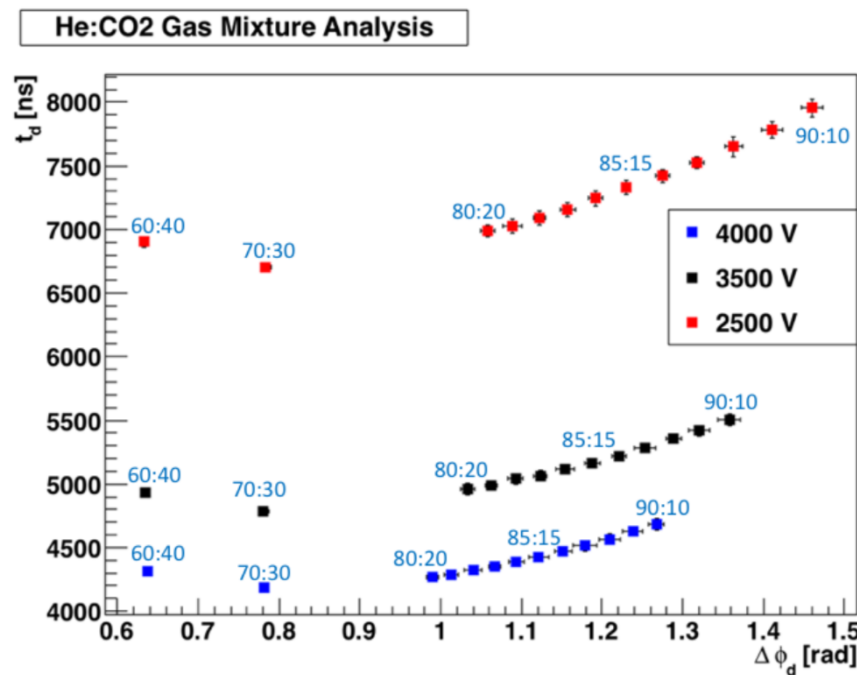


Fig. 29: Drift time versus drift angle for He:CO₂ using various potentials.

Now we must look at reducing diffusion effects for this mixture or at least understand what those effects are for our chosen mixture and potential. If we look at a plot of the diffusion in ϕ (*i.e.* σ_{ϕ_d}) as a function of diffusion in time (σ_{t_d}) as in Fig. 28, we see that the mixtures of He-CO₂ rival those of He-DME for ratios of 80:20-75:25. Given this plot alone, it can be concluded that mixtures below 75:25 of He-CO₂ do better than the He:DME mixtures.

The next step in this optimization is to look at the potential within the sensitive region of the RTPC. Here, note that preliminary experimental studies showed that

the maximum voltage on the cathode would be about -4000 V for He-CO₂. These studies were done with a flat prototype, so if we include that the cathode will be cylindrical, the potential may need to be less. Fig. 29 is a plot of He-CO₂ mixtures for potentials of -2500 V, -3500 V, and -4000 V. Again, the error bars represent the diffusion properties of the mixtures, which comes from the sigma of the Gaussian fit to the histogram. As one would expect, the higher potential, the faster the drift time and the smaller the drift angle.

Given all of this information and the requirements of the detector, we chose a gas mixture of helium-carbon dioxide with a ratio of 80:20 at -3500V. The mixture He-CO₂ meets the requirement of being fast with a small drift angle. For low momentum ions, such as protons in the case of the BONuS12 experiment, reducing multiple scattering is accomplished with low-mass gas mixtures. Thus He-CO₂ is ideal. The CO₂ in the mixture does not serve so much as a quencher, since helium essentially acts as its own quencher, but does limit the diffusion that occurs within the region. In addition, CO₂ is nonflammable.

4.3.5 DRIFT EQUATIONS

By knowing the drift time and drift angles of electrons starting at various values of r and z , we can plot the points and fit the points to an equation. These fit equations can be seen in the plots of t_d vs. r and ϕ_d vs. r (*i.e.* Fig. 30a and Fig. 30b, respectively). We can then use these equations in GEMC to find the drift time and drift angle of a drift electron created at any point along the path of the proton in the sensitive region of the RTPC. In order to speed up simulation efforts, simulation electrons were created at $r = 3$ cm to $r = 7$ cm at 0.5 cm increments and $z = -19$ cm to $z = 19$ cm at 5 cm increments. This give us 81 data points to work with (*i.e.* 9 points per fit line).

The 9 points for each value of z are fit to a second-order polynomial whose coefficients a and b depend on z . This is because the magnetic field changes with z , as shown in Fig. 26, for three values of r that are within the sensitive region of the RTPC. For each of the fit lines, or values of z , we extract the values of a and b for both drift time and drift angle. These values are shown in Fig. 31 and then fit to functions.

The points in Fig. 31 plots are all fit to fourth-order polynomials because of the shape of the magnetic field (see Fig. 26). These extracted functions defining the

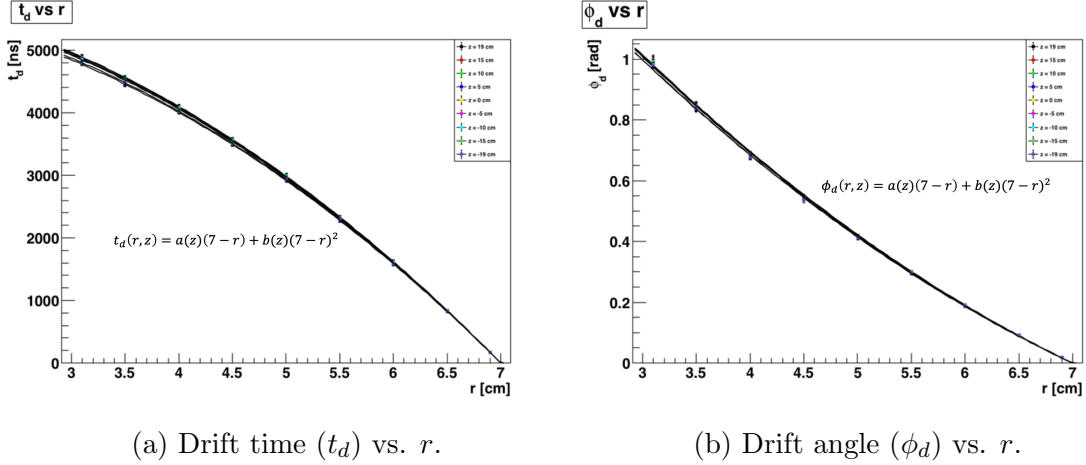
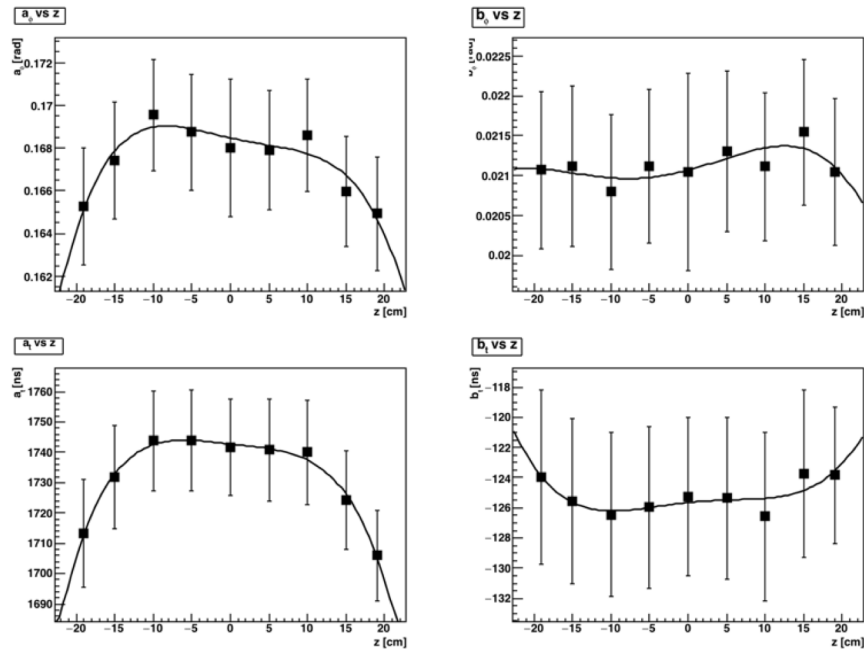


Fig. 30: Plots of drift electron properties.

Fig. 31: Parameters a and b for drift angle (a_ϕ and b_ϕ) and drift time (a_t and b_t).

coefficients a and b for the drift time and drift angle are

$$\begin{aligned}
 a_\phi(z) &= a_{\phi 0} z^4 + a_{\phi 1} z^3 + a_{\phi 2} z^2 + a_{\phi 3} z + a_{\phi 4} \\
 b_\phi(z) &= b_{\phi 0} z^4 + b_{\phi 1} z^3 + b_{\phi 2} z^2 + b_{\phi 3} z + b_{\phi 4} \\
 a_t(z) &= a_{t0} z^4 + a_{t1} z^3 + a_{t2} z^2 + a_{t3} z + a_{t4} \\
 b_t(z) &= b_{t0} z^4 + b_{t1} z^3 + b_{t2} z^2 + b_{t3} z + b_{t4}.
 \end{aligned} \tag{82}$$

These equations go into the `rtpc_hitprocess` class of GEMC. Therefore, when an ionization occurs in the simulation, GEMC uses those equations in Fig. 30b and Fig. 30a to calculate the position of the ionization electron when it reaches the outer edge of the RTPC.

4.4 DMS SIMULATIONS

As we have seen in the previous sections, the drift of the ionization electrons is very sensitive to the gas mixture, temperature, pressure and potential. The Drift-Gas Monitoring System (DMS) had to be designed to measure any fluctuations in those parameters of the gas by way of measuring drift velocity (see Section ??). In order to do that, simulations of the DMS had to be done to optimize the uniformity of the electric field within the drift region as well as the geometry of the chamber itself.

4.4.1 GEOMETRY

The parameters of interest to investigate and optimize were the anode diameter, diameter of the electrodes, and the distances between components. In order to look at these parameters, the geometry of the DMS was implemented into Garfield++, which consisted of its rectangular frame, grounded anode enclosure, anode wire, cathode plate, and field-shaping electrodes.

The first step is to define the gas mixture and geometry of the box used to house all of the DMS components. By using the `Sensor` class in Garfield++, the framework and wires necessary to see the DMS response was built. Then, as seen in the code snippet below, grounded planes were placed along the box.

```
// Setup the gas
MediumMagboltz* gas = new MediumMagboltz();
gas->SetComposition("He",80., "CO2",20.);
gas->SetTemperature(293.);
gas->SetPressure(760.);
gas->EnableDrift();           // Allow for drifting in this medium
gas->PrintGas();

// Build the geometry
GeometrySimple* geo = new GeometrySimple();
```

```

SolidBox* box = new SolidBox(L_x/2., L_y/2., L_z/2., L_x/2., L_y/2.,
                            L_z/2.);
geo->AddSolid(box, gas);

// Make a component with analytic electric field
ComponentAnalyticField* comp = new ComponentAnalyticField();
comp->SetGeometry(geo);

// Create a sensor for readouts
Sensor* sensor = new Sensor();
sensor->AddComponent(comp);

// Create grounded planes at the edges of the box
comp->AddPlaneX(0.,0., "x_min");
comp->AddPlaneX(L_x,0., "x_max");
comp->AddPlaneY(0.,0., "y_min");
comp->AddPlaneY(L_y,0., "y_max");

comp->AddReadout("x_min");
comp->AddReadout("x_max");
comp->AddReadout("y_min");
comp->AddReadout("y_max");

sensor->AddElectrode(comp, "x_min");
sensor->AddElectrode(comp, "x_max");
sensor->AddElectrode(comp, "y_min");
sensor->AddElectrode(comp, "y_max");

```

Next, the anode and ground plate surrounding that wire was defined. The following code snippet shows the anode wire defined by a single declaration.

```

// Anode
comp->AddWire(x_0 + r_a + wall_d/2., L_y/2, dAnode, vAnode, "a", 100.,
                50., 19.3);
comp->AddReadout("a");
sensor->AddElectrode(comp, "a");

```

The ground plate surrounding the anode was constructed from a number of large-diameter grounded wires that were placed to form that shape of that plate, since Garfield++ has a difficulties with these rather complicated structures. The same was done for the cathode plate, which used two layers of wire components. The electrode wires were all placed individually, with one example in the code snippet below.

```
comp->AddWire(dist, L_y/2.+b/2.+(i*s_y), dWire, Ex*(s_1 + (j*s_x)), name,
               100., 50., 19.3);
comp->AddReadout(name);
sensor->AddElectrode(comp, name);
```

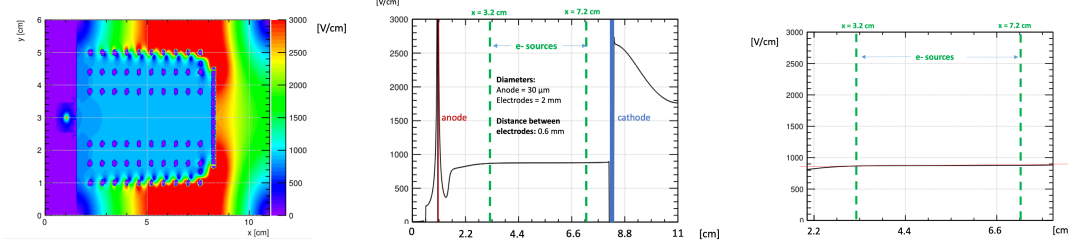
The function `AddWire(double x, double y, double D, double V, string label, double L, double T, double rho)`, places the wire at `x` and `y` with diameter `D`, potential `V`, label of the wire, length `L`, tension `T`, and density `rho` in that order. This placement was repeated 60 times completing 10 rows of electrodes with 6 wires comprising each electrode.

4.4.2 ELECTRIC FIELD

Once the geometries and code were in place, simulations to optimize those geometries were done to optimize the electric field. The primary concern was ensuring near-homogeneity of the electric field within the sensitive region. In order to look at that electric field, we need to look at the field profile along the plane where the anode lies.

Fig. 32a shows the contour map of the field, whose surface contour quantities are on the right legend. The plot in Fig. 32a is made using the `FieldView()` class. The potential from the cathode through to the electrodes was set to mirror what the electric field would be inside the RTPC (*i.e.* 875 V/cm). The profile of the field along the line at $y = 3$ cm is shown in Fig. 32b and Fig. 32c shows a zoom in to between the two sources to ensure its homogeneity (*i.e.* a straight line). These plots are created using the `PlotProfile()` function of the `FieldView()` class.

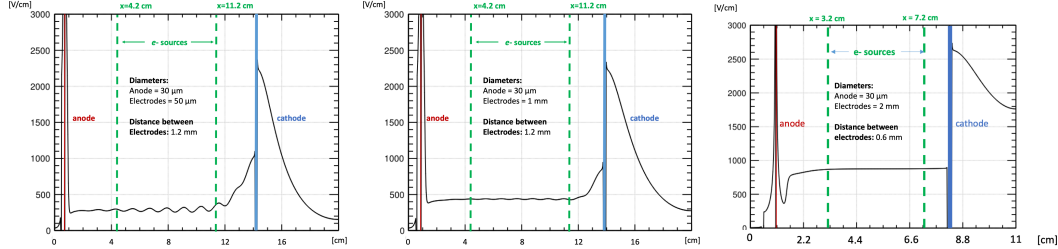
To achieve this straight line indicative of homogeneity, many simulations took place varying the electrode diameter and distance. The progression of these simulations can be seen in Fig. 33, beginning with small diameter electrodes (*i.e.* 50 μm) and a distance of 1.2 mm between each electrode (see Fig. 33a). The small diameter



(a) Electric-field contour map (b) Electric-field profile (c) Zoomed in electric-field along the cross-section in $x-y$ along the plane of the profile to between the two plane. anode. sources.

Fig. 32: Simulations of electric field within the DMS. In the profile plots in (b) and (c), the cathode and anode's locations are denoted as blue and red lines respectively. The sources and PMT's location and subsequent electron beams are pictured as green dotted lines.

coupled with the rather large distance between electrodes creates the large waves of field, which is not at all homogeneous. Fig. 33b shows the field profile with thicker electrodes (*i.e.* 1 mm), but the same separation as Fig. 33a (*i.e.* 1.2 mm). The waves of the field seem to be calmer, but still inhomogeneous.



(a) Electric field profile (b) Electric field profile (c) Electric field profile with electrode separation with electrode separation with electrode separation of 1.2 mm and diameter of 1.2 mm and diameter of 0.6 mm and diameter of 50 μm . 1 mm. 2 mm.

Fig. 33: Simulations electric field profile within the sensitive region of the DMS with various electrode diameters and distances.

Lastly, in Fig. 33c, the electrode diameter was set to 2 mm and the distance between electrodes was decreased to 0.6 mm. The field here in between the sources

is nearly homogeneous. Fig. 32c is zoomed in to that area between sources to verify how flat (*i.e.* homogeneous) the field is there.

Because of these simulations, we were able to identify the frame size, electrode and anode wire diameter, and distances between components. The distance between the cathode and the first set of electrodes was also chosen to be 0.6 mm, which also is the distance from the last electrode to the ground plate.

4.4.3 DRIFT VELOCITY

The last step of the Garfield++ simulations is to determine what we should expect for a drift velocity from the DMS. Just like the physical DMS, the drift velocity is calculated by taking the drift times from ionization electrons created at the lines of the sources that travel to the sources. In the simulations, electrons are started at one of the two areas where the sources would exist. From here the simulation tracks them toward the anode, and a histogram of the drift time is filled.

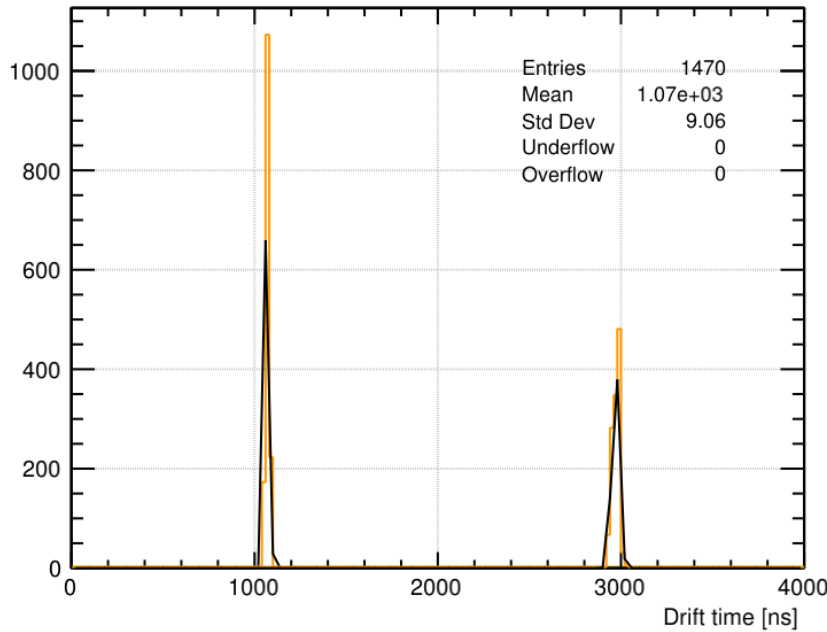


Fig. 34: Simulated drift time for electrons beginning at both the near and far sources from the anode.

Fig. 34 shows the drift times from 20 ionization electrons beginning at locations of both the sources. By taking the means from both Gaussian fits of each collection of drift times with the distance between the two sources (*i.e.* 4 cm), the drift velocity

can be calculated. That drift velocity from Garfield++ simulations is

$$v = \frac{\Delta d}{\Delta t} = \frac{d_f - d_n}{t_f - t_n} = \frac{4 \times 10^4 \mu\text{m}}{2969.90\text{ns} - 1070.75\text{ns}} = 21.06 \mu\text{m/ns}. \quad (83)$$

This gave us an idea what to expect when beginning the data acquisition process.

CHAPTER 5

DATA ANALYSIS

The first production run at JLab’s Hall B after the completion of the 12 GeV upgrade was called Run Group A. It ran over the fall of 2018 and spring 2019 with billions of events and 2 pB of data accumulated. The beam energy for the run was 10.6 GeV on a 5 cm liquid hydrogen target at a current between 5 nA to 75 nA. Because this is the first set of data coming from CLAS12 detectors, it serves as the data from which all important calibration and analysis is done to better understand all subsequent run groups.

This chapter will outline the software tools used for turning raw data into usable data sets, and the calibrations done to correct the raw data. Then we will begin the analysis portion, extracting the inclusive DIS cross section from Run Group A. Here we must make fiducial cuts to eliminate inefficient areas of individual detectors and kinematic cuts to select DIS events. Finally we put the resulting data together into bins of x and y (where $y = \nu/E$) to find the acceptance and calculate the inclusive DIS cross section. The purpose of extracting this cross section is to compare it the well-established Christy-Bosted fits to data.

5.1 CLAS12 OFFLINE SOFTWARE

The raw data coming from each detector first enters into the ReadOut Controller (ROC) and then gets stored in the EVent Input Output (EVIO) format. EVIO is a data format that is designed and maintained by JLab Data Acquisition Group. Once that data is available for off-line use, it requires decoding. Decoding is the process of taking EVIO raw data and converting it to High Output Performance Output (HIPO) format.

The HIPO format provides for a flexible data container structure, and minimizes disk space by utilizing LZ4 data compression (the fastest compression method currently available). In each HIPO file, data is stored as individual records with adjustable size. Each record is compressed, with a tag associated with it, and a pointer to it is stored in the file’s index table. For analysis this provides users with faster analysis by reading portions of the file depending on the final states to be analyzed.

Once the data is in HIPO format, it is ready to be reconstructed and analyzed. The CLAS12 event Reconstruction and Analysis (or CLARA) framework allows users to reconstruct physics events and analyze the files to yield usable physical data. CLARA does this by utilizing a service-oriented architecture to enhance agility, efficiency, and productivity of the software components within the CLARA framework. During the reconstruction process, the raw data from all detectors is taken in and processed by the corresponding packages. The main packages in CLARA are for *geometry, calibration constants, magnetic fields, particle swimming, and plotting/-analysis.*

The geometry tools were created due to the complexity of the CLAS12 subsystem geometries. The library contains primitives that represent all of the lines, planes and shapes of all the detectors. The tools provide methods to track particles through the different volumes for evaluation of track trajectories, such as line-to-surface intersections, ray tracing through objects, and evaluation of the distance of closest approach to a line or surface. Because subsystem parameters can change from run group to run group and sometimes even within a run group, time-dependent geometry variations exist that allows for consistency between simulation, reconstruction, and event visualization packages.

The Calibration Constants Database (CCDB) was originally developed at JLab for the GlueX Experiment in Hall D. It was adopted by CLAS12 group because of its functionality for storing and accessing structured tables. At the decoding stage, file formats change, but also data structures. Signals are converted from hardware notation (*i.e.* crate, slot, channel) to CLAS12 notation (*i.e.* sector, layer, component). Then during reconstruction, the time stamps of these databases are utilized in order to access run-specific constants. The CLAS12 software tools employ an Application Programming Interface (API) that parses CCDB tables to create structured maps of the constants stored in memory by sector, layer, component. This method allows for fast retrieval of only the relevant constants.

Magfield, the magnetic field package for CLARA, consists of binary field maps created from engineering models of the solenoid and torus magnets in CLAS12. These field maps contain a header with meta-data describing field pedigree, its grid coordinate system, and the coordinate system of the field components. Because the field is often accessed within a sequence of points all contained within a single grid, *magfield* uses time-saving software probes to cache nearest neighbors.

To propagate charged particles through the CLAS12 magnetic fields, the *swimmer* package, in parallel with the *magfield* package, is used. Swimmer uses a fourth-order adaptive-size Runge-Kutta integrator with single step advancement achieved by a configurable Butcher tableau advancer. The purpose of swimming particles with this toolkit is to propagate particles to a given plane, to the closest point on a line, or to a given (x , y , z) coordinate. Performance is improved for forward propagation in CLARA by reducing the dimensionality of a state vector that contains the main track parameters, by changing from the path length independent variable to the coordinate along the beamline, which defines the nominal CLAS12 z -axis.

Finally, the plotting and analysis tools can be used for further data calibration, monitoring, and analysis. The toolkit was developed in the Java programming language and the interface is similar the ROOT platform developed at CERN for high-energy physics analysis. The plotting package, called *groot*, allows for histogram and graph creation, filling and manipulation. Plot fitting can be done using the Java-based MINUIT library available in the JHEP repositories.

Once the information about particle tracks is collected, that information is passed to a service called the Event Builder (EB). The EB takes the results from the upstream services and correlates the information from the CLAS12 subsystems. To form charged particles from the data, EB matches geometric coincidences in the distance of closest approach (DOCA) between detector responses and tracks. The event start time is important for all time-based particle identification and is determined from the optimal charged particle candidate in the Forward Detectors with an associated FTOF timing response. The last step in the EB is particle identification. For our purposes, we are really only concerned with e^- identification. This e^- PID is largely done through calorimetry and Cherenkov information. If the measured energy deposition in the ECAL is consistent within 5σ of the expected value of the sampling fraction, and the photoelectron response in the HTCC is consistent with $\beta \approx 1$, then the particle is assigned to be an electron or positron depending on the track curvature in the DC.

5.2 CALIBRATION

Once the raw data is decoded and reconstructed, it can be analyzed. However, initial analysis must be dedicated to detector calibration. Calibration is done for each detector and even for each run so that the experimental quantities like time and

energy are correctly extracted from raw TDC and ADC data. Just as in the RTPC, drift times and distances of electrons in the DC are subject to the properties of the gas (*i.e.* pressure, temperature, gas mixture, etc.). These changes determine calibration constants for the DC, just as they do for the RTPC. TOF calibration constants change with changes in the wires or electronics. The calibrations of individual detectors have been done by a large group of CLAS12 collaborators. Those calibration efforts will be briefly discussed and focused on the detectors relevant to this analysis.

The order of calibrating the detectors was important since some calibrations rely on the proper calibrations of other detectors. The first step was the DC calibration with FTOF time matching. This relied on a crude start time (few ns level) calibration of the FTOF, whose offset requires calibration between the FADC and TDC. Then the data needed to be recooked, which means that it required a run through CLARA again for reconstruction given the new calibration constants. After the recooking, the FTOF was calibrated more precisely with CTOF time matching. Energy calibrations for the FTOF could be done before the DC calibration using crude DC calibration parameters for path length corrections, but ideally done post DC calibration. FTOF timing calibrations employed PID from the Event Builder, and defined the start time using the electron in the EC, positron in the EC, or high-momentum pion in the DC/FTOF. Another recooking was necessary to implement the new calibration constants from CCDB.

Once the DC and FTOF were properly calibrated, CLAS12 subsystems were calibrated. This included CND, CTOF, EC, FT (hodoscope and calorimeter), HTCC, LTCC, and RICH. Timing calibrations for all subsystems relied on PID from the EB and start time from the FTOF. The energy calibrations for the subsystems only employed PID from the EB. Recooking was again necessary after subsystem calibration to update the reconstructed data using the new CCDB parameters. Lastly, the RF calibration was done to capture the overall RF time shifts run by run.

Run	Torus	Solenoid	$\langle i \rangle$ [nA]	E_{beam} [GeV]	Run Range
4903	-100%	-100%	45	10.6	4763-5031
5038	-100%	-100%	45	10.6	5032-5189
5197	-100%	-100%	45	10.6	5190-5285
5306	-100%	-100%	45	10.6	5286-5419

TABLE III: Summary of calibrations done for Run Group A.

The resulting calibrations can be summarized in Table III. The required specifications for calibration were generally met. For the DC, a requirement that $\delta x = 250\text{-}400 \mu\text{m}$ was not met since after calibration $\delta x = 330\text{-}400 \mu\text{m}$. However, for FTOF, $\delta t = 60\text{-}110 \text{ ps}$ (p1b) and after calibration $\delta t = 60\text{-}120 \text{ ps}$ (p1b). For the EC, a requirement that $\sigma_E/E = 10\%/\sqrt{E}$ was met exactly after calibration and the $\langle t_\gamma \rangle < 500 \text{ ps}$ was also met.

5.3 FIDUCIAL CUTS

Each detector has limits where it cannot efficiently detect particles. Near the edges of detectors are particularly vulnerable to inefficient particle detection. The goal of placing fiducial cuts on detectors is to minimize ineffective areas of each detector while maximizing the number of “good” particles we keep.

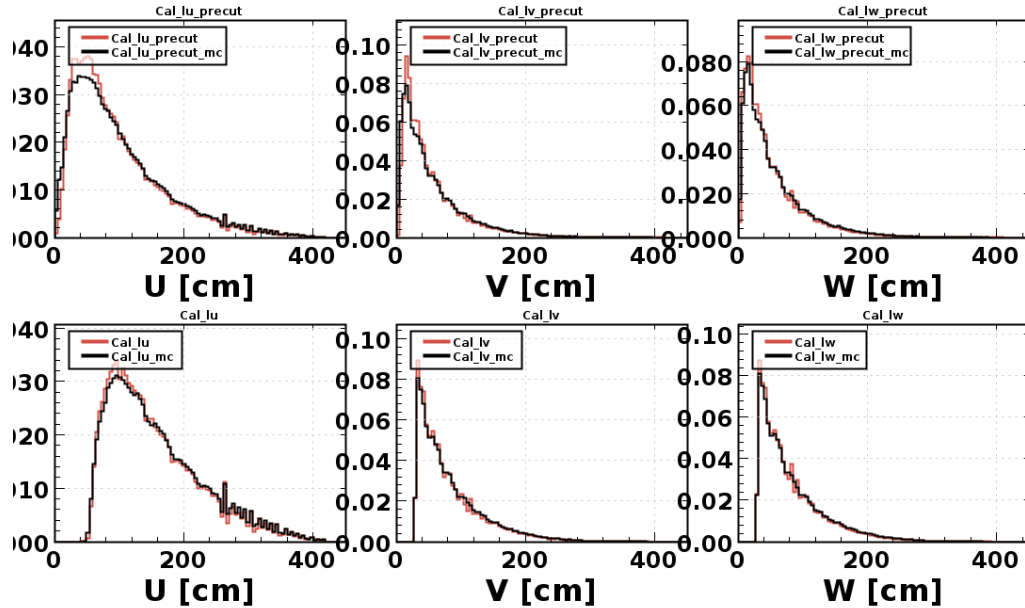


Fig. 35: 1D distributions of the U, V, and W sectors of the PCAL. The uncut histograms are on the top and the bottom histograms contain the cuts: $U < 30 \text{ cm}$, $30 < V < 390 \text{ cm}$, and $30 < W < 390 \text{ cm}$. All plots are normalized to account for any mismatch in total statistics. Red lines are from RGA data and black lines are for the Monte-Carlo (MC) data.

The EC is the detector that we use for determining the electron four-momentum and all kinematics that are calculated from that momentum. When electrons enter the EC they shower and stop. That EM shower is broad, so we have to remove events

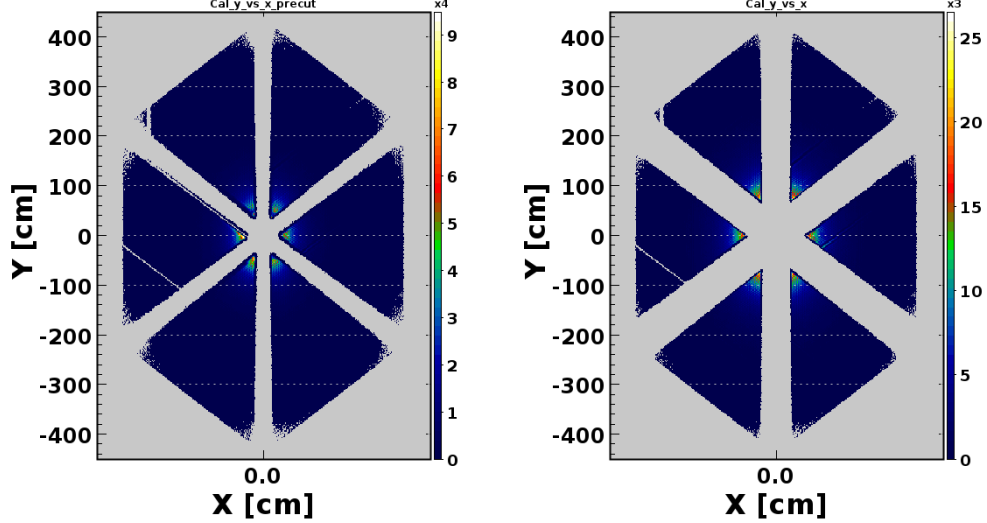


Fig. 36: 2D histograms of the uncut PCAL hits on the left and the 2D histogram containing the fiducial cuts.

close to the edges as showers leak out and the sampling fraction becomes unreliable for e^- PID.

Remember that the EC sector is defined by U, V, and W edges of its triangular shape. We can cut on those edges for the PCAL only and the effects will propagate through to the EC_{inner} (ECin) and EC_{outer} (ECout). The established cuts for the PCAL are $U < 30$ cm, $30 < V < 390$ cm, and $30 < W < 390$ cm. Fig. 35 shows the one-dimensional distributions of the U, V, and W sectors of the PCAL. The uncut histograms are on the top and the bottom histograms contain the cuts that were described. Fig. 36 contains the two-dimensional histograms of the uncut PCAL hits on the left and the 2D histogram containing the fiducial cuts.

5.4 KINEMATIC CUTS

Our goal is to extract the inclusive DIS cross section for the process $ep \rightarrow e'X$, which means that certain constraints must be put on some of the kinematic variables. To isolate DIS events, $W > 2$ GeV and $Q^2 > 1$ GeV². Other *kinematic cuts* must be applied. In order to isolate events that originate at the target, we require $-10\text{cm} < v_z < 10\text{cm}$, where v_z is the z-vertex position of the track. Fig. 37 shows v_z before (left) and after (right) cuts. Because there is no discernible difference between left and right (uncut and cut), it is clear that cuts were made during reconstruction.

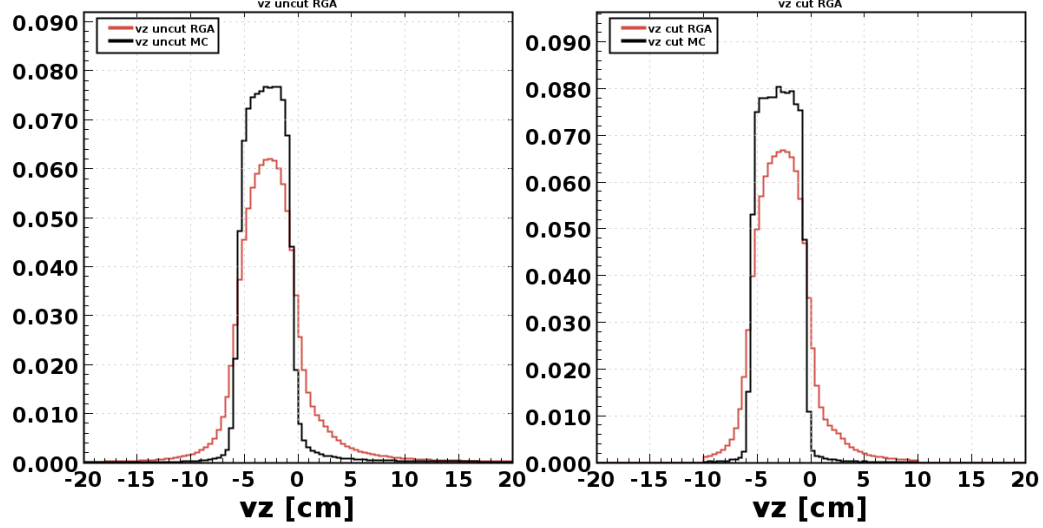


Fig. 37: v_z before and after all described cuts. Red lines are from RGA data and black lines are for the Monte-Carlo (MC) data.

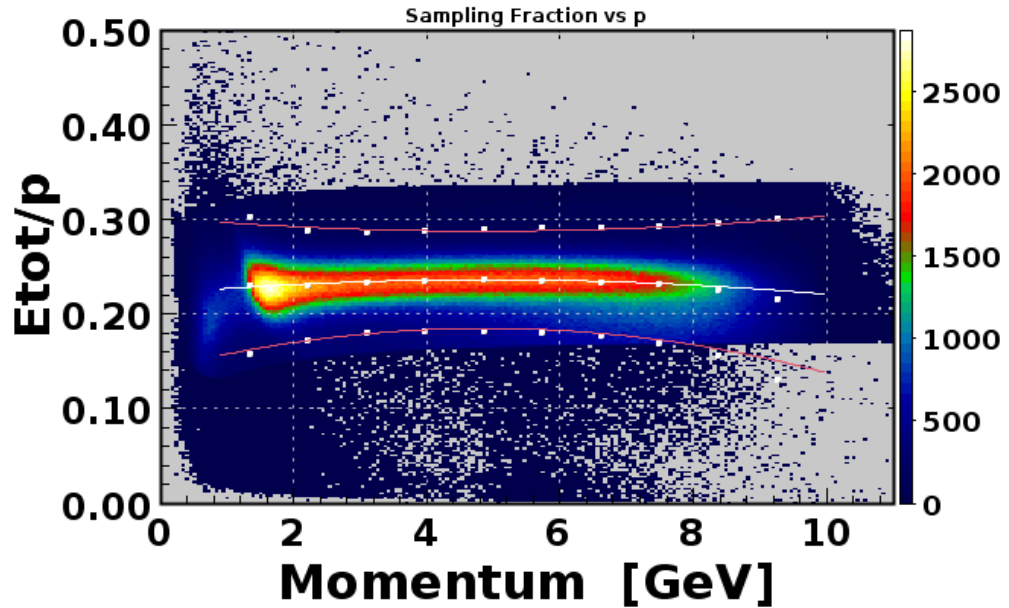


Fig. 38: Slicing and fitting of the sampling fraction to create a 5σ cut.

The last significant kinematic cut occurs on the sampling fraction. The sampling fraction is defined as E_{tot}/p , where E_{tot} is the total energy deposited by the particle in all three layers of the EC and p is the particle's momentum. When the sampling

fraction is plotted vs p , electrons will appear as a band around 0.25 and with a momentum of above 1 GeV to eliminate any minimum ionizing particles like pions. To do this, we take slices of the plot, find the mean and sigma of E_{tot}/p for that slice and cut out anything $\pm 2.5\sigma$. We do this for values along p and fit the points for means and $\pm 2.5\sigma$ to polynomials that we can cut on to isolate electrons.

Because of the Forward Detector's coverage in θ , we need to make sure that $5^\circ < \theta < 40^\circ$ so it falls within that coverage. Fig. 39 shows the uncut kinematic variables and Fig. 40 was created with the kinematic cuts described. Fig. 41 and Fig. 42 shows uncut and cut (respectively) energy distributions for E' , EC, and the number of photoelectrons in the HTCC ($nphe$). The next group of plots Fig. 43-48 shows two-dimensional histograms of various kinematic variables all uncut and after applying all cuts. In Fig. 48 one can clearly see the successful application of the 5σ cut described in the previous paragraph.

The summary of applied cuts is as follows:

- $W > 2$ GeV
- $Q^2 > 1$ GeV 2
- $5^\circ < \theta < 40^\circ$
- PCAL fiducial cuts: $U < 30$ cm, $30 < V < 390$ cm, and $30 < W < 390$ cm
- $-10 < v_z < 10$ cm
- 5σ cut on sampling fraction
- HTCC cut: $nphe > 5$
- EC energy cuts: $E_{PCAL} > 0.06$ GeV, $E_{EC_{in}} > 0.025$ GeV, $E_{EC_{out}} > 0.05$ GeV

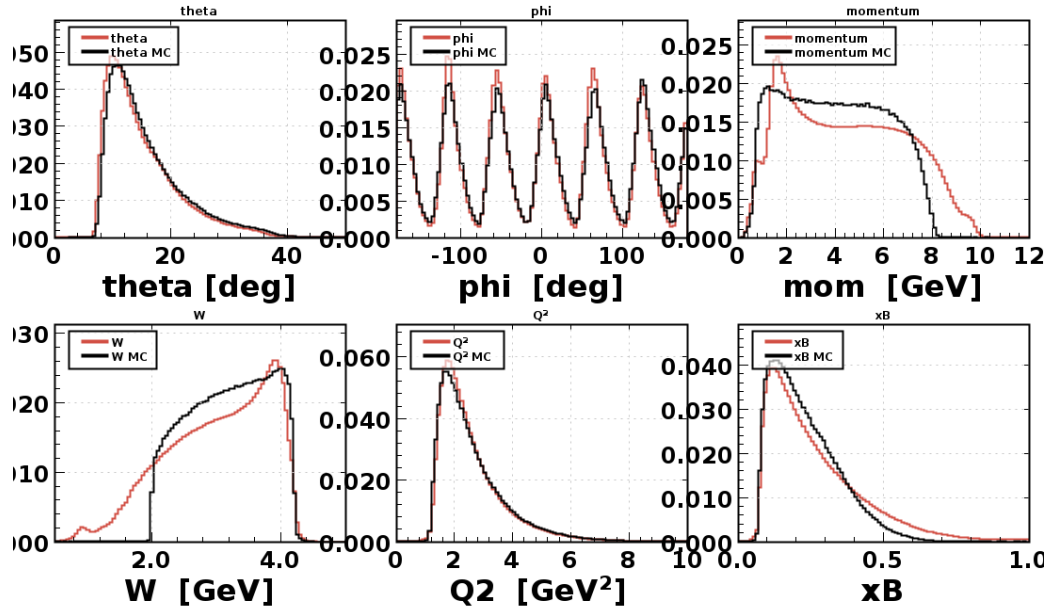


Fig. 39: Kinematics variables before cuts. Red lines are from RGA data and black lines are for the Monte-Carlo (MC) data.

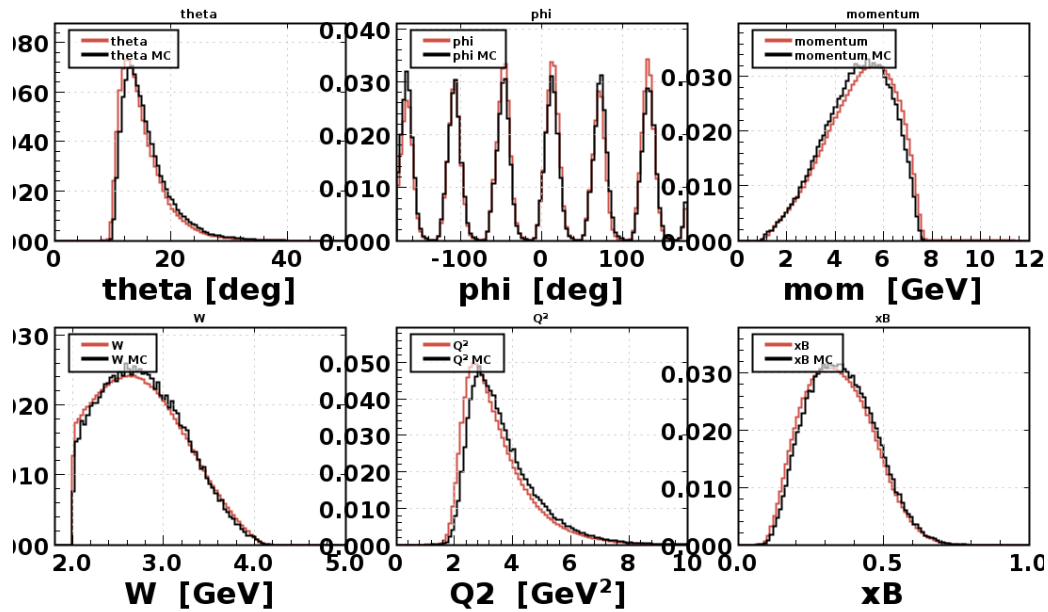


Fig. 40: Kinematics variables after all described cuts. Red lines are from RGA data and black lines are for the Monte-Carlo (MC) data.

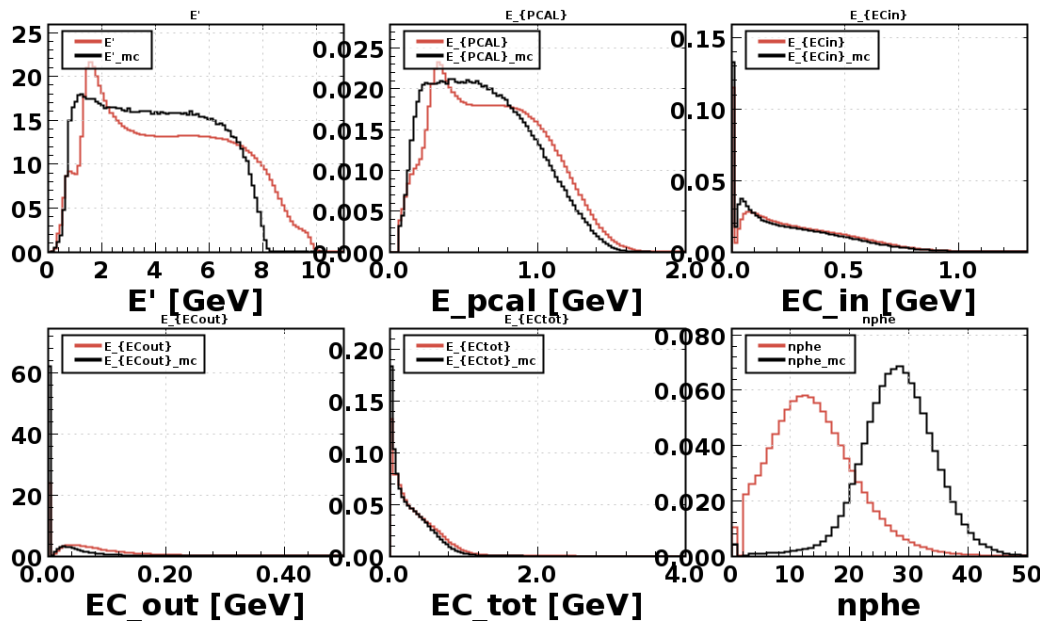


Fig. 41: E' and EC energies before cuts. Red lines are from RGA data and black lines are for the Monte-Carlo (MC) data.

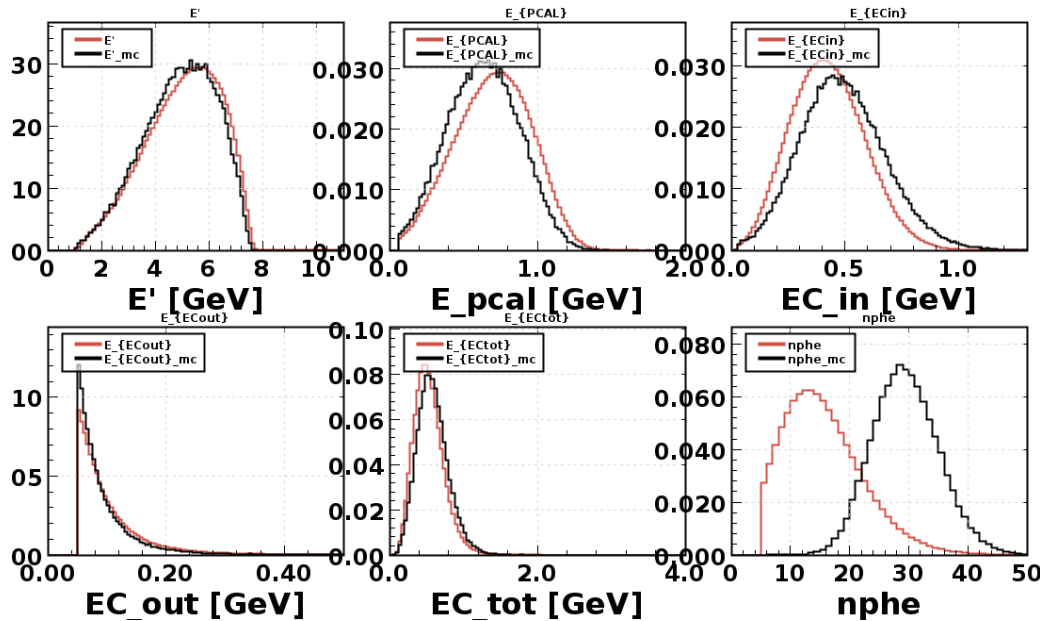


Fig. 42: E' and EC energies after all described cuts. Red lines are from RGA data and black lines are for the Monte-Carlo (MC) data.

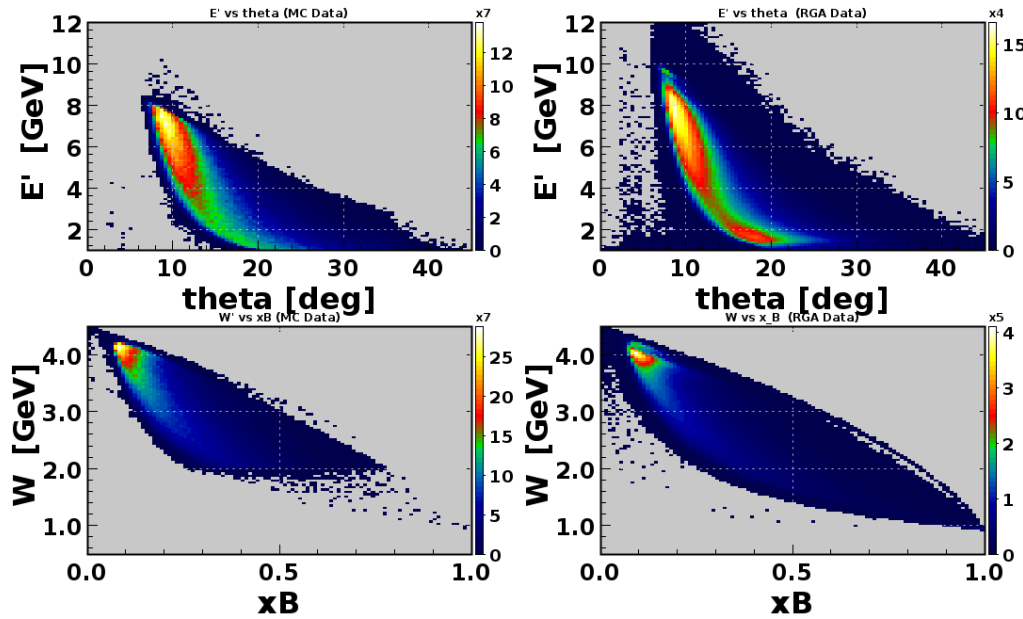


Fig. 43: E' vs. θ and W vs. x_B before cuts.

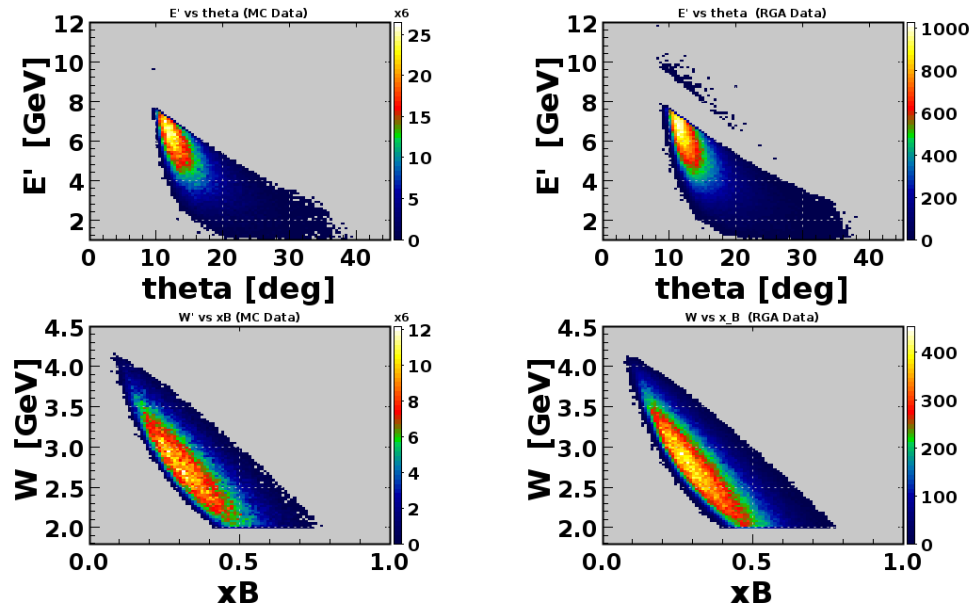


Fig. 44: E' vs. θ and W vs. x_B after all described cuts.

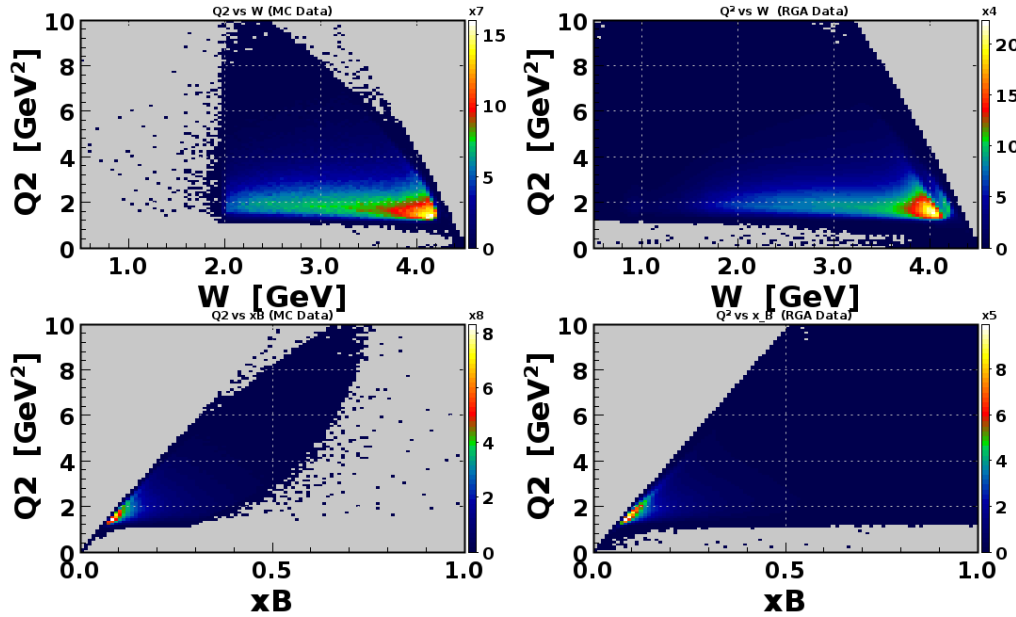


Fig. 45: Q^2 vs. W and Q^2 vs x_B before cuts.

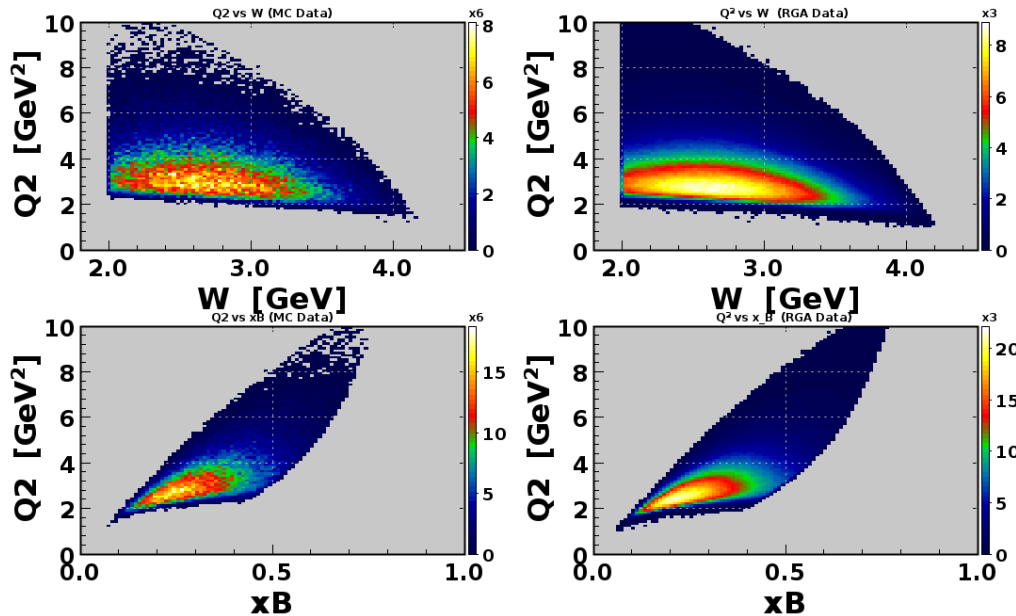


Fig. 46: Q^2 vs. W and Q^2 vs x_B after all described cuts.

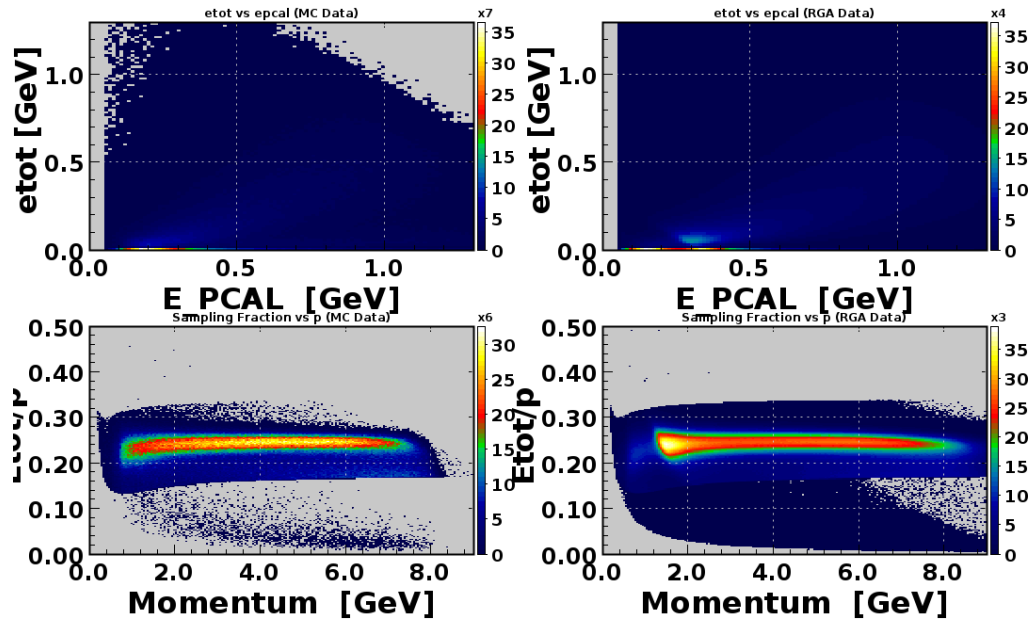


Fig. 47: $E_{EC_{tot}}$ vs E_{PCAL} and Sampling fraction before cuts.

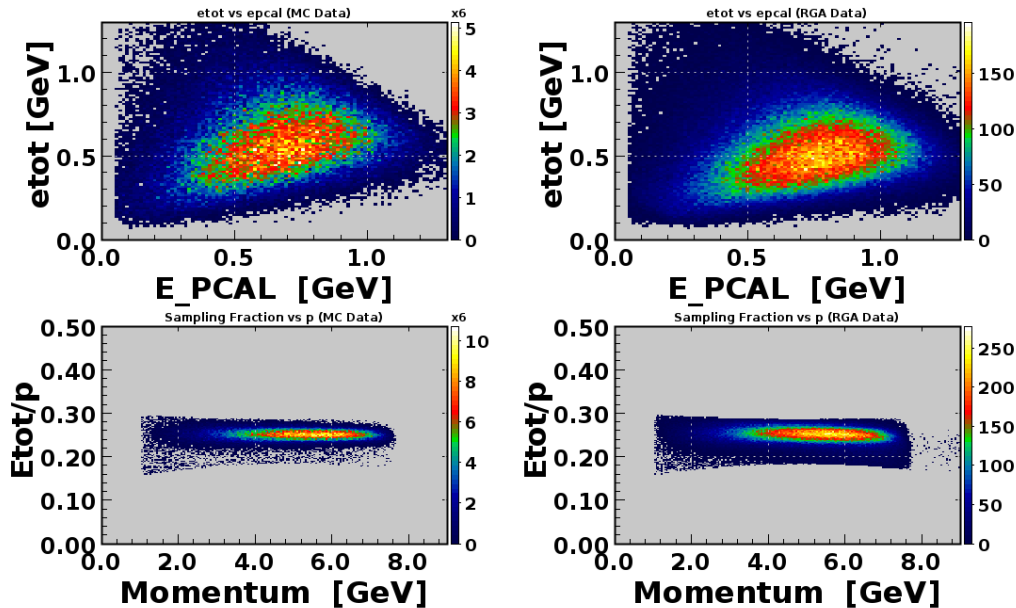


Fig. 48: $E_{EC_{tot}}$ vs E_{PCAL} and Sampling fraction after all described cuts.

5.5 BINNING AND ACCEPTANCE

The data, after kinematic and fiducial cuts, needs to be separated into kinematic bins in order to first obtain the acceptance of the bin and then to extract the cross section for each bin. The acceptance for the bin is defined as

$$A(x, y) = \frac{N_{\text{rec}}(x, y)}{N_{\text{gen}}(x, y)}, \quad (84)$$

where $A(x, y)$ is the acceptance of the bin, $N_{\text{gen}}(x, y)$ is the number of generated events in that bin, and $N_{\text{rec}}(x, y)$ is the number of reconstructed events in that bin. The binning occurs in x (*i.e.* the Bjorken- x scaling variable) and y , which is defined as $y = \nu/E$. This particular binning was done because of the cross section calculation that was done using model by Christy-Bosted, namely:

$$\frac{d^2\sigma}{dxdy} = \frac{4\pi\alpha_{\text{em}}S}{Q^4} \left[xy^2 F_1(x, Q^2) + \left(1 - y - xy\frac{M^2}{S}\right) F_2(x, Q^2) \right], \quad (85)$$

where $S = 2ME$.

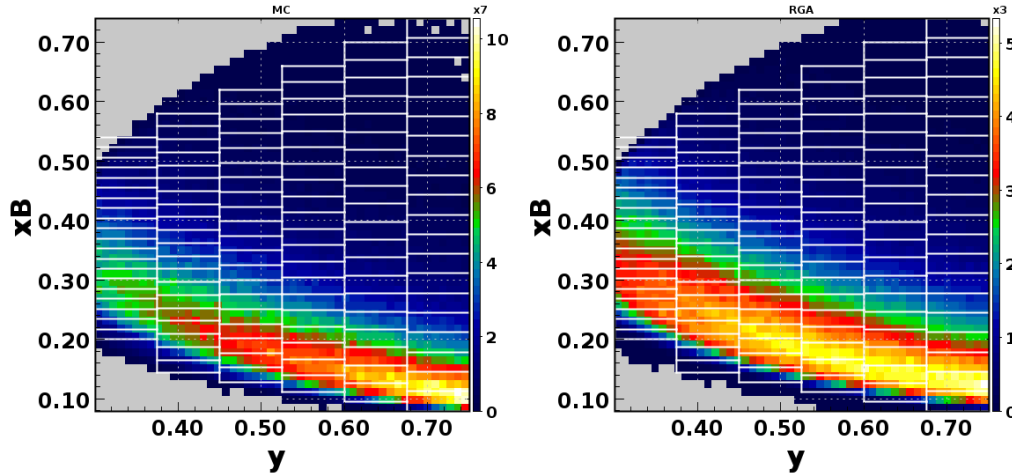


Fig. 49: Binning in the x, y space.

The binning in x and y was done in an attempt to gather equal statistics in each bin. Equal bins were chosen in y because, in the range $0.3 < y < 0.74$, the distribution was relatively flat. In x , however, the shape of the distribution required tuned binning throughout. Table IV outlines the bin size and range for x . Fig. 49 shows the binning in the x, y space.

Figs. 50-52 show the acceptance for each bin. For each bin in y , the value of which is located at the top of each plot, the acceptance is then plotted for each bin in x .

Bin	y Range	x_{\min}	x_{\max}	Δx
1	0.3, 0.375	0.2	0.54	0.17
2	0.375, 0.45	0.144	0.58	0.0218
3	0.45, 0.525	0.128	0.62	0.0246
4	0.525, 0.6	0.112	0.66	0.0274
5	0.6, 0.675	0.096	0.7	0.0302
6	0.675, 0.75	0.08	0.74	0.033

TABLE IV: Summary of binning in x and y .

Ideally the acceptance for all bins would be unity, so it is clear that the acceptance in areas of high and low y is lacking. In Fig. 50 we see that the acceptance is low at $x \rightarrow 0$ and in Fig. 52 acceptance drops as $x \rightarrow 1$.

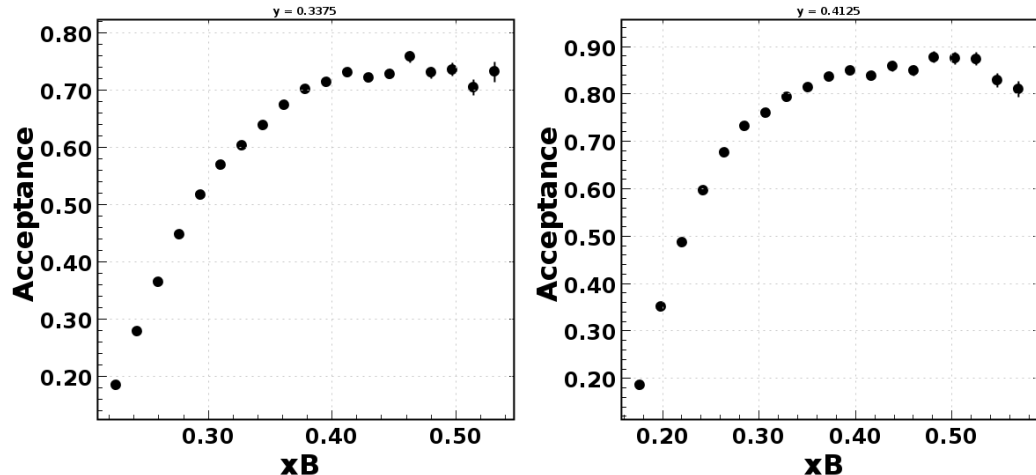


Fig. 50

5.6 FARADAY CUP AND INTEGRATED LUMINOSITY

As will become more evident in the next section, cross section calculations depend on the number of beam electrons accumulated during a particular run. Since that cross section is essentially the probability that a reaction occurs for a given process, it also depends on the number of target nuclei. The *luminosity* (\mathcal{L}) is a value incorporates both accumulated charge and number of target nuclei by expressing the number of beam particles per time multiplied by the number of target nuclei per unit

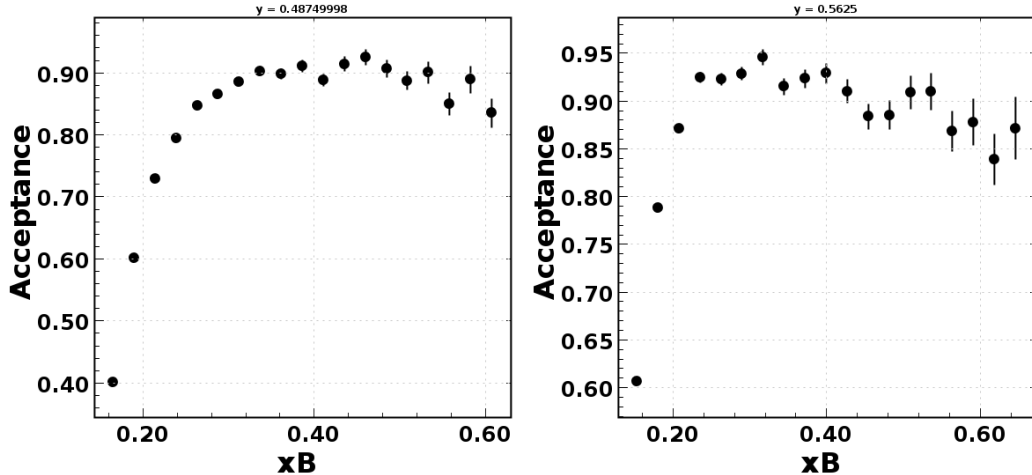


Fig. 51

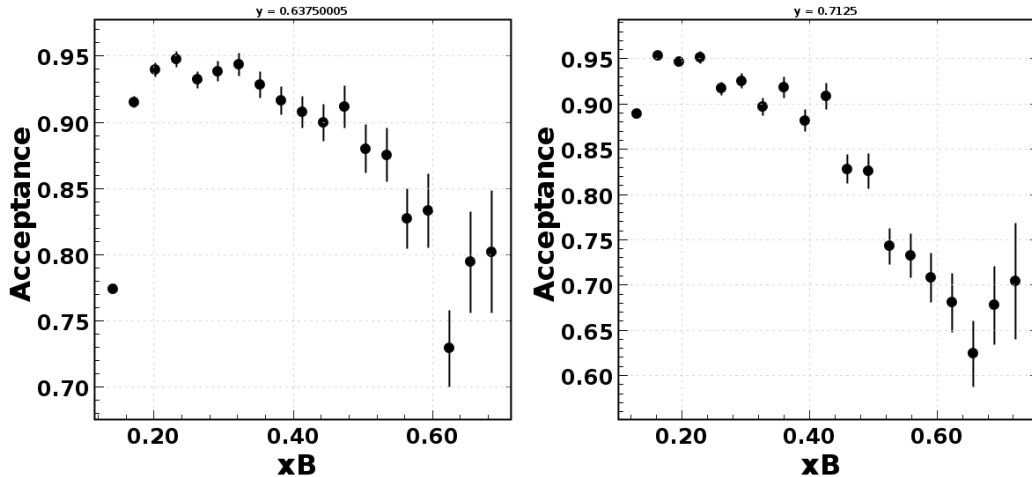


Fig. 52

area. By integrating that luminosity over time, we can recover the total number of beam electrons multiplied by the number of target nuclei per unit area

$$\mathcal{L}_{\text{int}} = \int \mathcal{L} dt = \frac{N_B \times N_{\text{target}}}{A}, \quad (86)$$

where N_B is the total number of incident electrons, N_{target} is the number of target nuclei, and A is the cross-sectional area of the target. This time-integrated luminosity (\mathcal{L}_{int}) depends on calculating N_{target}/A and knowing the total number of electrons incident on the target.

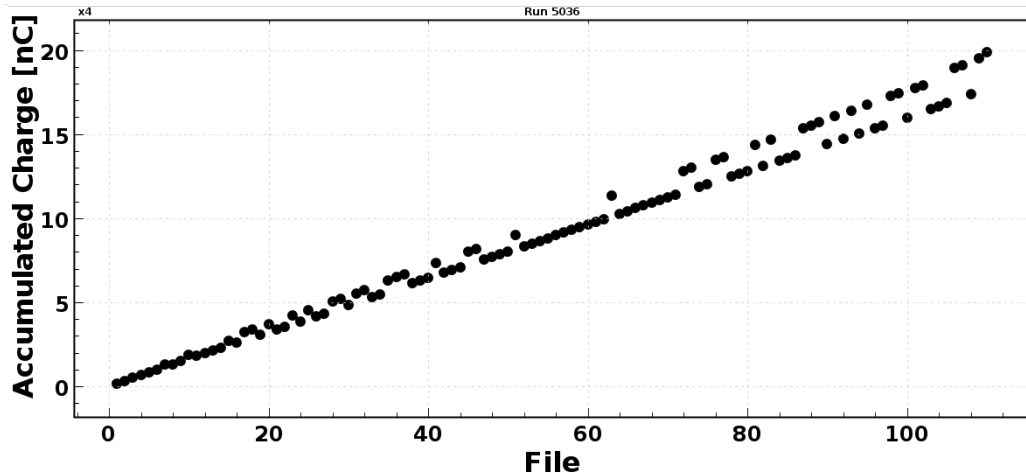


Fig. 53: Accumulated charge vs. file for Run 5036.

Calculating the number of target nuclei per area can be done utilizing the ideal gas law

$$PV = nRT, \quad (87)$$

where P is the target pressure, V is the volume of the target, n is the amount of target material that exists (in moles), R is the gas constant equal to 8.314472 J/K·mol, and T is the target temperature. We can rearrange the equation to get

$$N_{\text{target}} = 2nN_A = \frac{2PVN_A}{RT}, \quad (88)$$

where $N_A = 6.0221 \times 10^{23} \text{ mol}^{-1}$ is Avogadro's number and the "2" comes from there being two hydrogen atoms in the liquid hydrogen target used for Run Group A (RGA). Finally, in order to find N_{target} in terms of the target density ρ , we use the relation

$$n = \frac{m}{M_m} = \frac{PV}{RT} \Rightarrow \rho = \frac{M_m P}{RT} \quad (89)$$

or

$$\frac{P}{T} = \frac{\rho R}{M_m}, \quad (90)$$

where M_m is the molar mass. That results in

$$N_{\text{target}} = \frac{2\rho V N_A}{M_m}. \quad (91)$$

This gives us a time-integrated luminosity

$$\mathcal{L}_{\text{int}} = \frac{2N_B N_A \ell \rho}{M_m}, \quad (92)$$

where ℓ is the length of the target.

The last variable to find is the total number of electrons N_B . We do this by accessing the charge accumulation in the Faraday Cup. The Faraday Cup (FC) is device located at the end of the beam line that catches charged particles, giving access to the total charge during a given period. The FC data is given in nano Coloumbs (nC) integrated over the entire run, where in every nC of charge there are $6.24150636309 \times 10^9$ electrons. Fig. 53 shows that accumulated charge as the number of files for the run 5036. That allows us to get the total number of incident electrons for each run, which is N_B in our integrated luminosity.

5.7 CROSS SECTION

The final step is to actually calculate the differential cross section for each x, y bin. That cross section for experimental data is given by

$$\frac{d^2\sigma}{dxdy} = \frac{N(x, y)}{\mathcal{L}_{\text{int}} A(x, y) \Delta x \Delta y}, \quad (93)$$

where $N(x, y)$ is the number of DIS events in the bin, \mathcal{L}_{int} is the integrated luminosity, $A(x, y)$ is the acceptance of that bin, Δx is the size of the bin in x , and Δy is the size of the y bin. The number of selected inclusive deep inelastic scattering events $N(x, y)$ is calculated as the integral of the particular x, y bin.

Fig. 56 shows the calculated inclusive deep inelastic scattering differential cross sections (on the y-axis) for the values of y (listed as the title of the plots) and Bjorken- x on the x-axis. The open dots are the calculated cross sections from the RGA data. The green band is DIS cross sections calculated from Eq. 85 using Christy-Bosted fits of F_1 and F_2 with associated error and the same values of x and y for that bin. The error on the RGA calculated cross section is

$$\delta \frac{d^2\sigma(x, y)}{dxdy} = \frac{d^2\sigma/dxdy}{\sqrt{N(x, y)}}, \quad (94)$$

where $N(x, y)$ is the integral (or total number of entries) of the x, y bin.

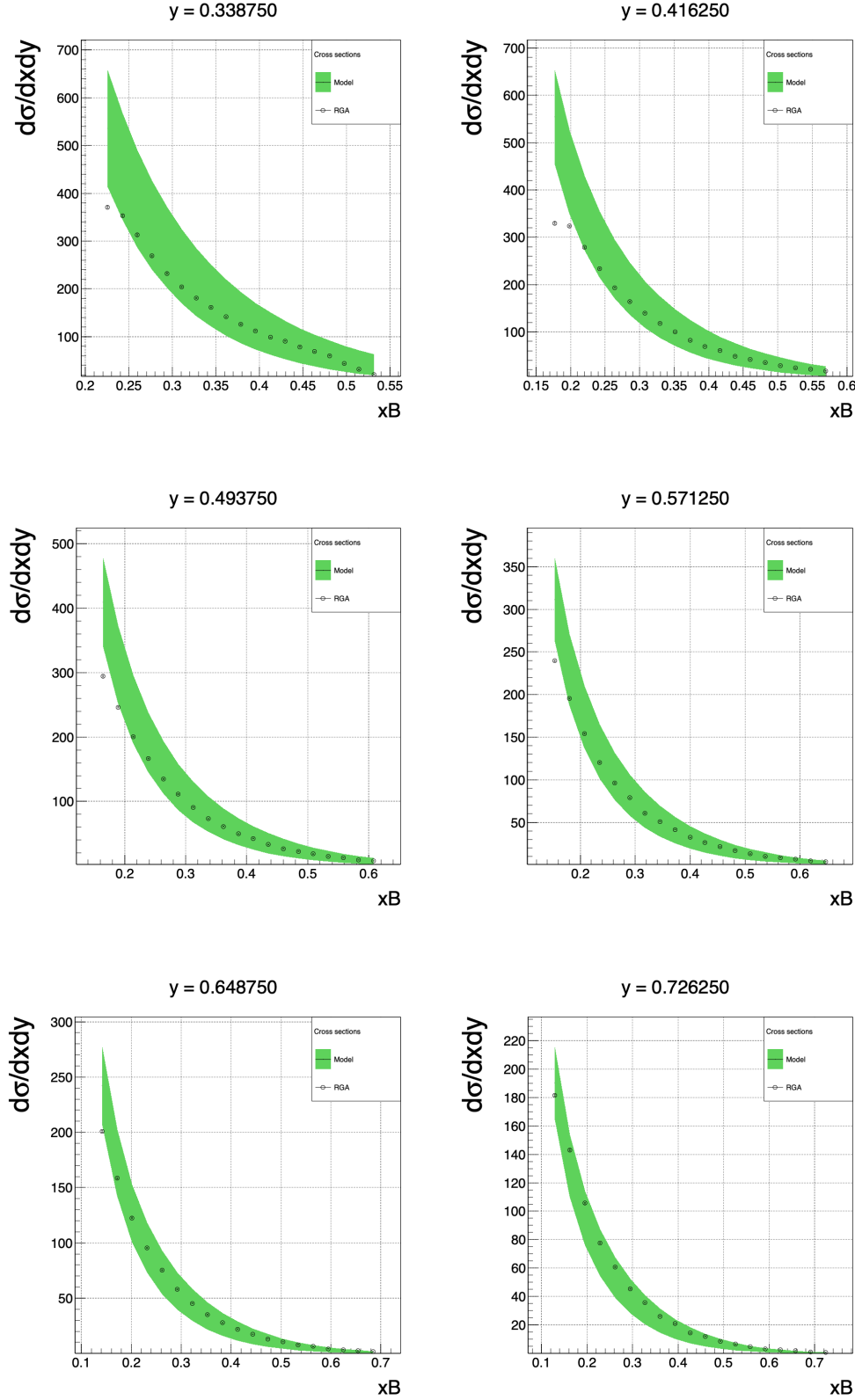


Fig. 56: Plots of inclusive DIS differential cross section vs x_B for various values of y .

CHAPTER 6

RESULTS

At the onset of working on this project, the goal was to simulate, optimize, design, construct, install and run the Radial Time Projection Chamber (RTPC) for the Barely-Offshell Nucleon Structure experiment at 12 GeV (BONuS12). BONuS12 ran successfully from January to March 2020, collecting 3.9 billion triggers and about 2.8 billion triggers with the RTPC. The run was cut short by the COVID19 pandemic, with only half of the data expected to be collected. Because it was always known that data collection would not be done in time for analysis in this work, important analysis on the first experiment (Run Group A) of CLAS12 was done to contribute to the collaboration. This chapter will summarize the results of the RGA data analysis as well as the first monitoring and preliminary analysis plots from BONuS12.

6.1 RGA CROSS SECTION

The inclusive deep inelastic scattering differential cross section (found in Fig. 56) was extracted for $0.06 < x < 0.76$ and $0.3 < y < 0.75$ using data from Run Group A (RGA). The cross section was plotted and compared with the calculated cross section using the fits of F_1 and F_2 in Eq. 85 from Christy-Bosted and Monte-Carlo (MC) generated data. To get a better idea of how well they compare, Fig. 59 shows the ratio of $d\sigma_{\text{RGA}}/d\sigma_{\text{MC}}$, where $d\sigma_{\text{RGA}}$ is the differential cross section from RGA data and $d\sigma_{\text{MC}}$ is the differential cross section from MC data and model fits to F_1 and F_2 . Clearly, the RGA calculated cross section differs from the MC data more so for lower x and y . Calibrations for RGA are still ongoing, which may be the cause of the discrepancy.

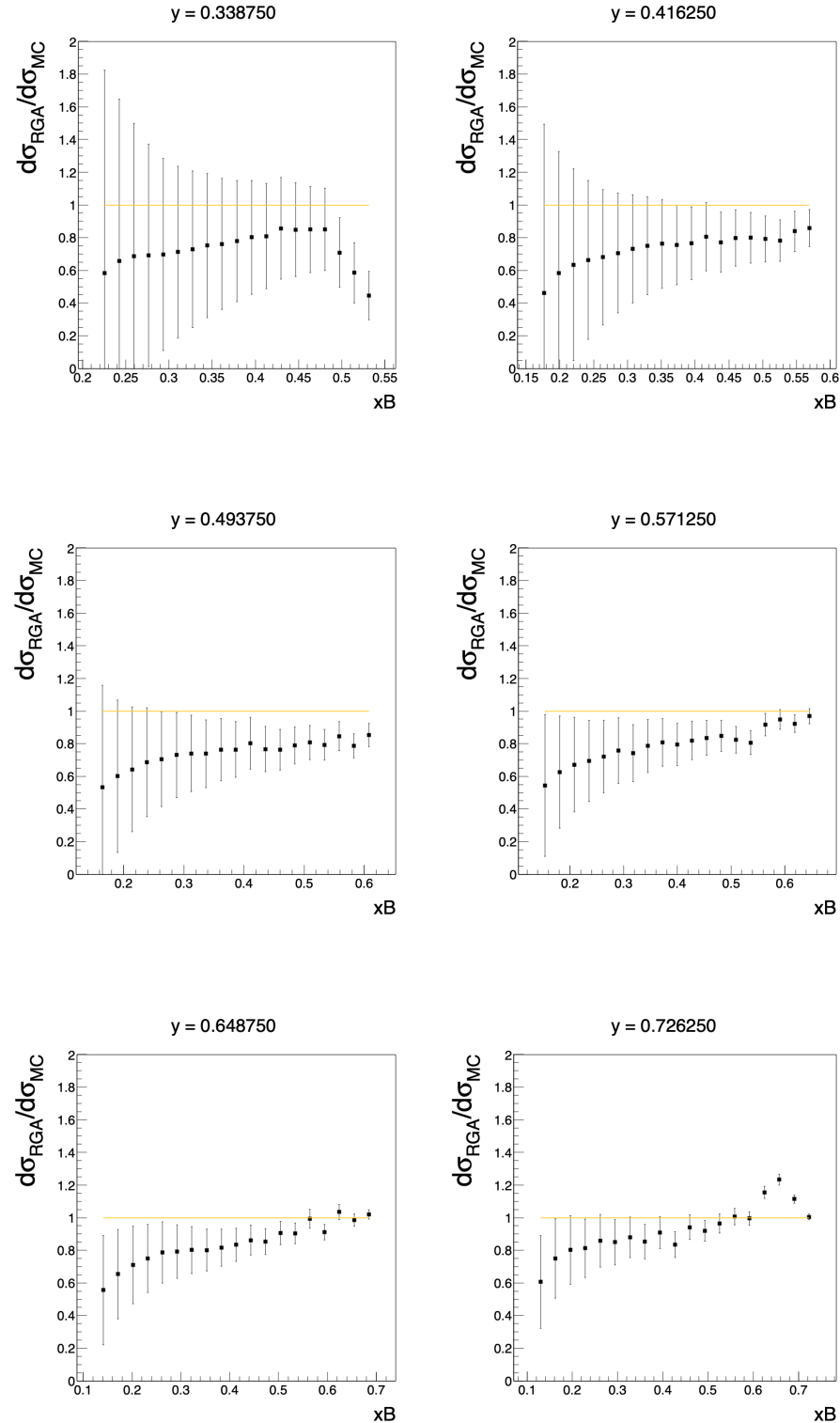


Fig. 59: Graph of the ratio of the differential cross section ratio for RGA data over Model data vs x_B for various values of y .

6.2 BONUS12

During the run time of BONuS12, some adjustment were made and target gases were used. The target was changed from hydrogen ^2H to helium ^3He for calibration and deuterium ^2D for production. At the beginning of Run Group F, of which BONuS12 was apart, the beam energy was set to 1 pass around the accelerator to produce 2.14 GeV energy. This allowed the gathering of data to examine the elastic scattering from protons in hydrogen, a well known process from which we can confirm the accuracy of the incoming data. Once the 2.14 GeV data was gathered, the energy was increased with 5 passes to created 10.4 GeV beam electrons.

Once the 10.4 GeV beam energy reached, it became clear that the RTPC was not operating up to expectations. The number of hits/track and the mean ADC value of those individual hits began to decrease. In order to fix these problems, the potential in the drift region as well the potential differences between each GEM foil was adjusted. The hits/track and mean ADC of the hits would increase for a time (about 6-12 hours), and then those values would decrease again. The magnitude of the magnetic field created by the solenoid was also adjusted. The first runs were at 5T field, and then decreased to 4T. This was in an attempt to decrease the drift angle of the drift electrons, thinking that those electrons were having a difficult time passing through the GEM foils. In all, this RTPC (RTPC1) was in use for 33 days at roughly 50% efficiency. After that time, RTPC1 was replaced with another RTPC that was constructed (RTPC3) during a 5 day replacement period. RTPC3 ran for 3 days before the shutdown.

6.2.1 DMS

During the running of BONuS12, the RTPC gas system ensured that the proper gas flow rate and pressure. Downstream of the RTPC drift gas flow was the Drift-gas Monitoring System (DMS), there to monitor any fluctuations in important gas properties (*e.g* temperature, pressure, gas mixture, etc.). The output of the DMS was TDC whose readings were accumulated in histograms for each channel. Channel 1 (CH1) was the TDC readout for coincidence between an anode signal and signal from PMT near to the anode. Channel 2 (CH2) was the TDC readout for coincidence between an anode signal and signal from PMT far to the anode.

Fig. 60 shows an example of the drift time output for channels 1 and 2 (left and

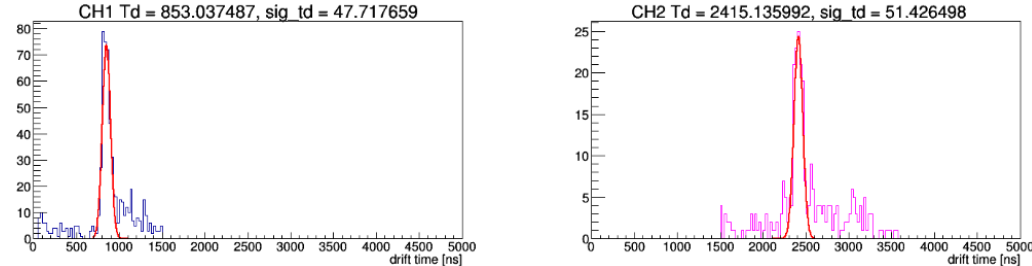


Fig. 60: DMS drift time histograms for CH1 (left) and CH2 (right) on Run 11953.

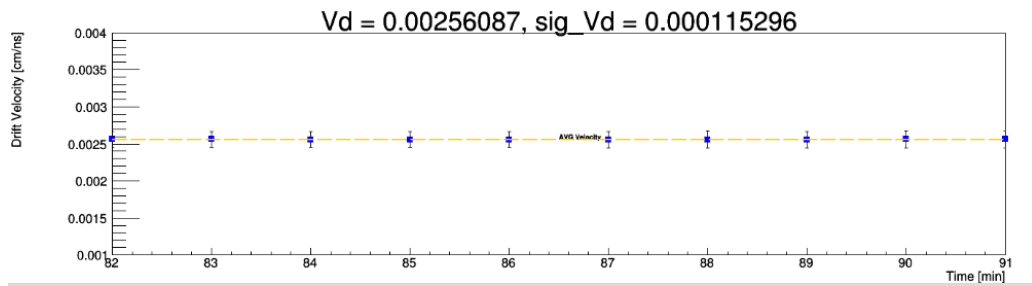


Fig. 61: DMS drift velocity vs. time graph during Run 11953.

right, respectively) for Run 11953. Fig. 61 shows the drift velocity vs. time graph for Run 11953. The orange dotted line is the average velocity for the 10 minutes shown on the plot. These plots were indicative of the majority of runs. The few exceptions occurred for two reasons.

The first reason for deviations from typical DMS output was its sensitivity to the flow rate of the drift gas through the RTPC. If it was too low, not enough gas would flow into the DMS and the number of accumulated statistics would decrease and the peaks in drift time typical of runs (as in Fig. 60) would not appear. This did serve as an advantage when identifying empty gas bottles, however. If the flow rate was high and statistics dropped, it was an indicator that the bottle of drift gas needed to be replaced.

The other reason for deviations from typical DMS output was, of course, variations in the parameters it was designed to monitor. When the ambient pressure decreased, the drift times for each channel would decrease, which meant the drift velocity increased. Fig. 62 shows the channel 1 drift time for each run. Fig. 63 shows the channel 2 drift time for each run, and Fig. 64 shows the DMS pressure for

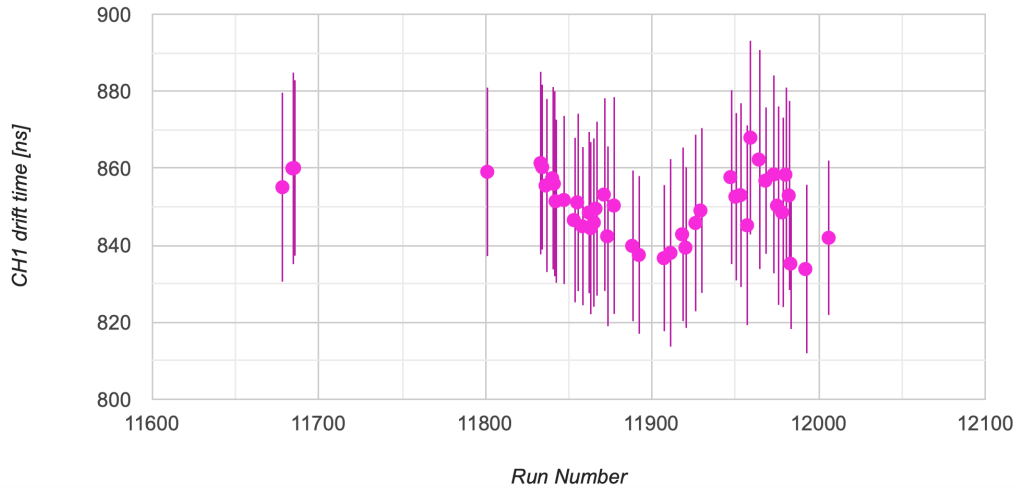


Fig. 62: DMS drift velocity for channel 1 vs. run.

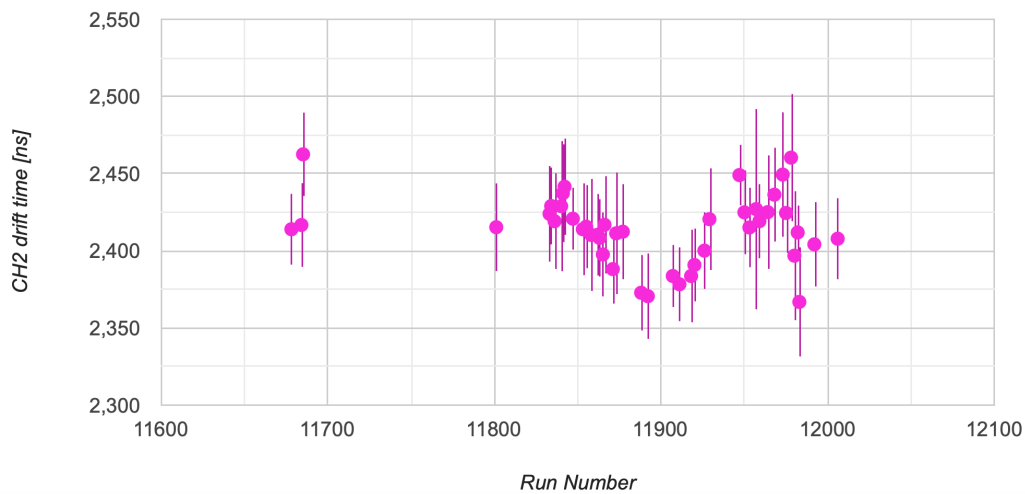


Fig. 63: DMS drift velocity for channel 2 vs. run.

each run. The ambient pressure began to decrease around Run 11847 to a minimum at Run 11918. This corresponds to the decreased drift times visible at the same time, which meant that the DMS was operated successfully. Fig. 65 shows the drift velocity over Run Group F.

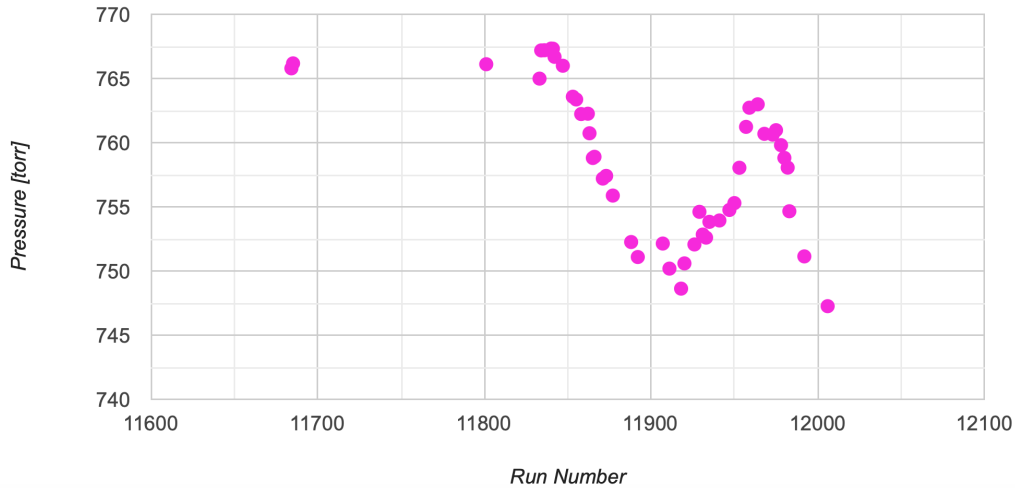


Fig. 64: DMS gas pressure vs. run.

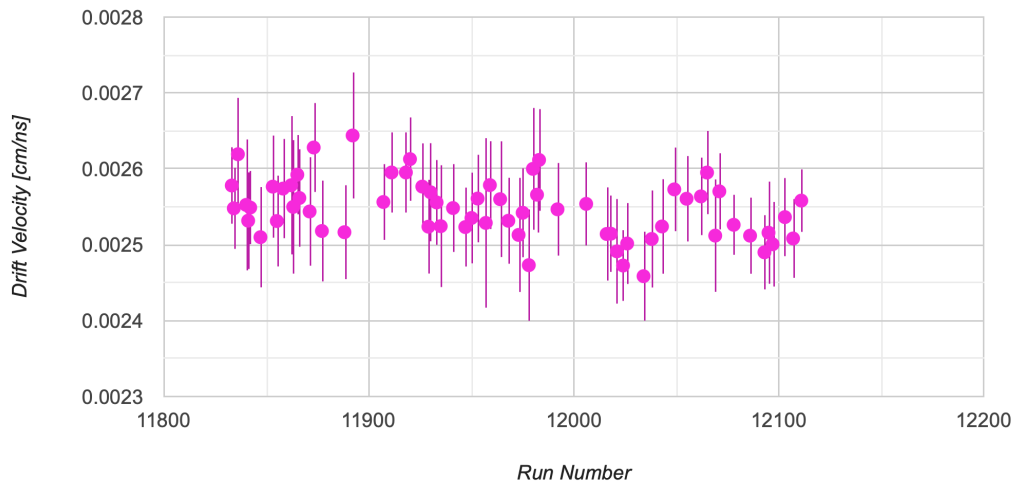


Fig. 65: DMS drift velocity over all RGF runs.

6.2.2 RTPC

The tracking software developed by David Payette for RTPC hit reconstruction was put into use on RGF data as soon as data started flowing in. Fig. 66 shows two examples of reconstructed hits in an event using Version 27 of the reconstruction software for Run 11637, which is a 2.14 GeV run at 5 nA. Fig. 67 shows the reconstructed hits for two events in Run 12240, which is a 10.4 GeV run at 240

nA. This increase in current is the reason there are more tracks per event.

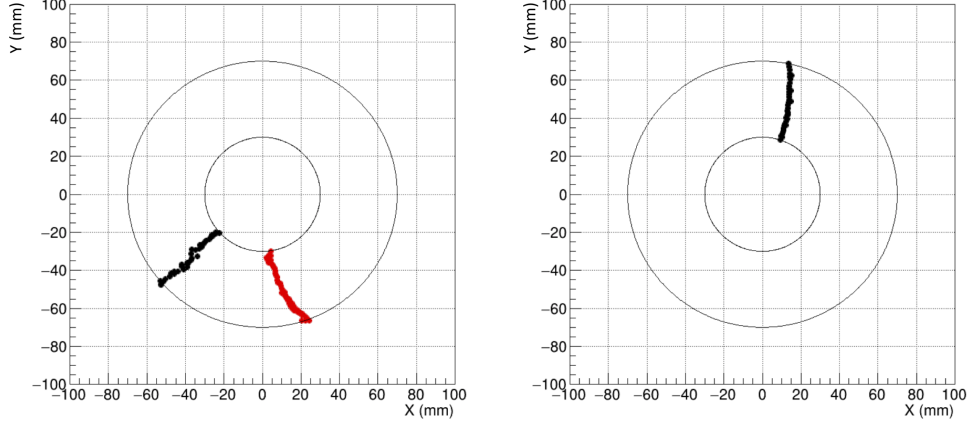


Fig. 66: Two examples of reconstructed hits in an event in the RTPC using Version 27 of the reconstruction software in an Cartesian x, y space for Run 11637 (a 2.14 GeV run). [Courtesy D. Payette.]

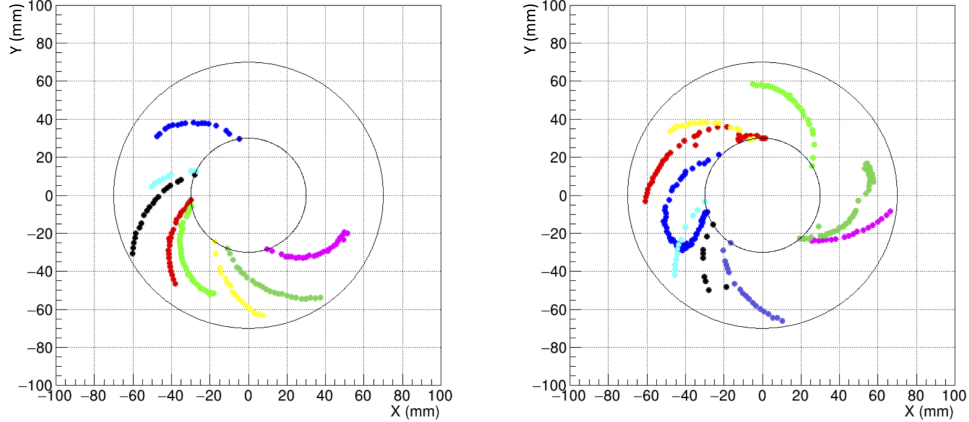


Fig. 67: Two examples of reconstructed hits in an event in the RTPC using Version 26 of the reconstruction software in an Cartesian x, y space for Run 12240 (a 10.4 GeV run). [Courtesy D. Payette.]

The RTPC reconstruction class, which is integrated into CLARA, consists of a few steps necessary for momentum reconstruction that will lead to extraction of the F_2^n/F_2^p structure function ratio. The first is the reconstruction of the hits. This is done using a combination of parameters extracted from Garfield++ and data. The next step is to find possible tracks and disentangle crossing tracks from one another.

Finally, once tracks are identified, a helix fitter is used to recovery the momentum and vertex of the track. A particle with charge q follows a helical path with a uniform magnetic field B with a certain radius R . The momentum of that particle is then

$$p = RqB. \quad (95)$$

Obviously, since the magnetic field is not uniform, the charged particle (in our case, the proton) does not travel in an exact helix. The answer to this problem is something called a Kalman Filter. The Kalman Filter accounts for non-uniform magnetic fields by treating variations in each step. Implementation of the Kalman Filter will likely be done at a later date.

Once the kinematics of the proton tracks are reconstructed from the raw data, that reconstructed data is analyzed to find the “good” proton among the background. This identification in parallel with revisions to the reconstruction code will be an ongoing process. Fig. 68 shows some of the kinematics of the reconstructed protons with one cut on t_{shift} , which is a variable determined from the electron trigger. This cut of $-200\text{ns} < t_{\text{shift}} < 500\text{ns}$ is done in an attempt to isolate protons tracks that occur around the time of an identified electron trigger in the FD.

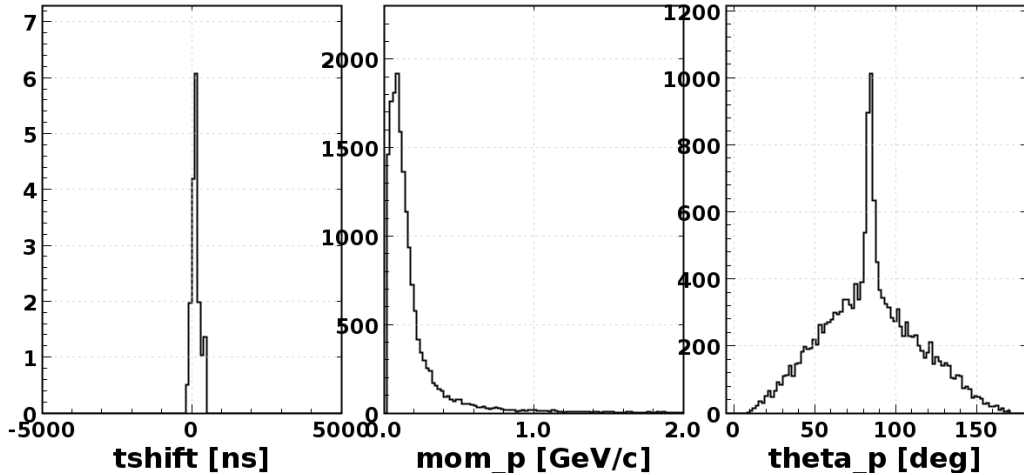


Fig. 68: The time shift (t_{shift}), momentum, and theta (θ) of the reconstructed protons in Run 11637.

Because Run 11637 was a low energy run at 2.14 GeV, it was analyzed in comparison to expected elastic scattering kinematics. For elastic $ep \rightarrow e'p'$ events, the proton momentum is

$$p_{\text{calc}} = \sqrt{Q^2 + \frac{Q^4}{4M_P^2}} \quad (96)$$

and the scattering angle is

$$\theta_{\text{calc}} = \tan^{-1} \left[\frac{1}{\left(1 + \frac{E}{M_p}\right) \tan\left(\frac{\theta_e}{2}\right)} \right], \quad (97)$$

where E is the beam energy and θ_e is the scattering angle of the electron. Fig. 69 shows the 2D distributions of the calculated momentum (“mom_predicted” in the plot) and measured momentum for protons as well as the difference between the predicted and measured values of the momentum for Run 11637. Fig. 70 shows the 2D distributions of the calculated theta (“theta_predicted” in the plot) and measured theta (“theta_measured” in the plot) for protons as well as the difference between the predicted and measured values of theta for Run 11637.

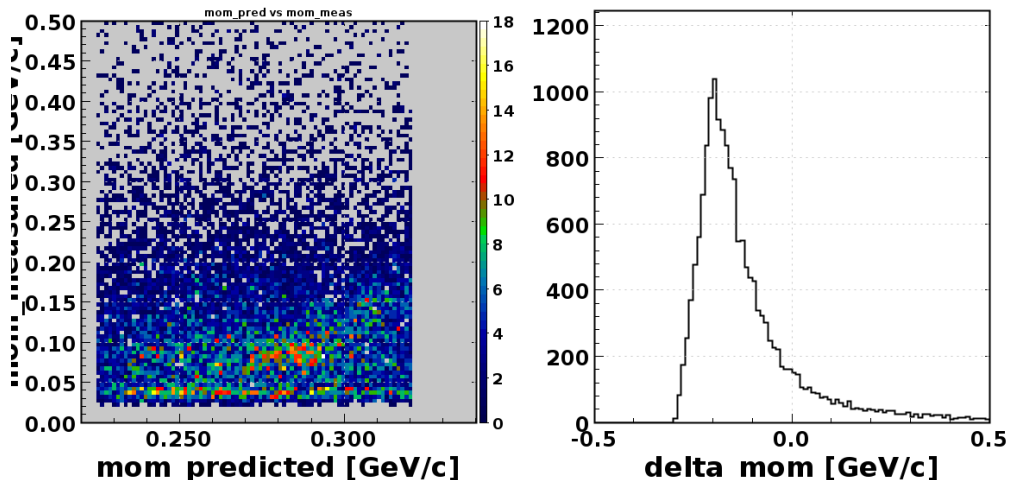


Fig. 69: On the left: 2D distributions of the calculated momentum (“mom_predicted” in the plot) on the x -axis and reconstructed momentum (“mom_measured” in the plot) for protons on the y -axis in Run 11637. On the right: The difference between the predicted and measured values of the momentum for Run 11637.

There are some clear irregularities in the reconstruction of proton kinematics. For example, in Fig. 69, the peak of Δp is around 200 MeV, which should be at zero. Calibrations that focus on recovering accurate kinematics will be ongoing by BONuS12 collaborators until expected results for the calibration runs are achieved. Once acceptable calibration occurs, intensive data analysis to recover the proton momentum will begin and likely continue for years to come. This analysis will lead to an extraction of the F_2^n/F_2^p structure function ratio at higher x than previously accessed, allowing us to know more about the overall structure of the neutron, which was the

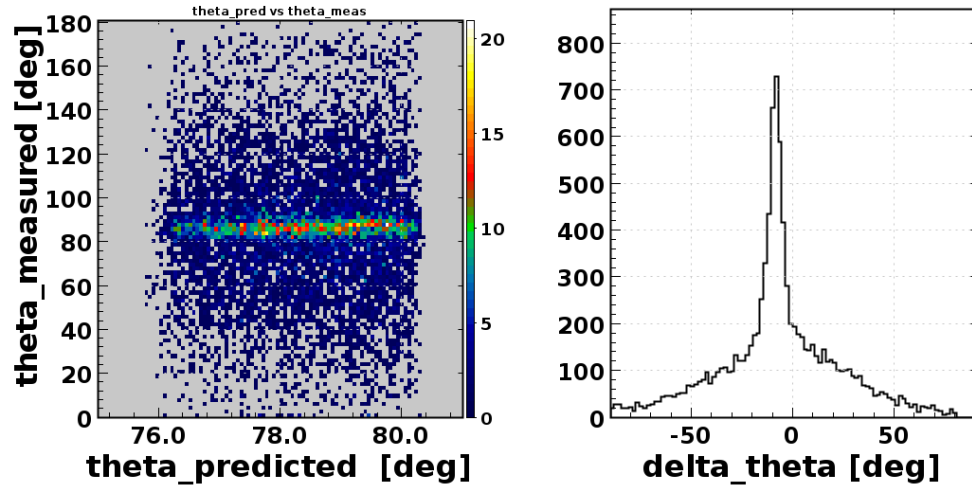


Fig. 70: On the left: 2D distributions of the calculated theta (“theta_predicted” in the plot) on the x -axis and reconstructed theta (“theta_measured” in the plot) for protons on the y -axis in Run 11637. On the right: The difference between the predicted and measured values of theta for Run 11637.

goal of the simulation and development of the Radial Time Projection Chamber for the Barely-offshell Nucleon Structure Experiment at 12 GeV.

REFERENCES

- [1] A. A. *et al.*, “Constraints on large- x parton distributions from new weak boson production and deep-inelastic scattering data,” *Phys. Rev. D*, vol. 93, 2016.
- [2] J. Arlington, “Measurement of the f_2^n/f_2^p , d/u ratios and a=3 emc effect in deep inelastic electron scattering off the tritium and helium mirror nuclei,” *Jefferson Lab PAC37 Proposal*, 2010.
- [3] J. A. *et al.*, “A measurement of the ratio of the nucleon structure function in copper and deuterium,” *Z. Phys. C*, vol. 57, p. 211, 1993.
- [4] J. G. *et al.*, “Measurement of the a-dependence of deep inelastic electron scattering,” *Phys. Rev D*, vol. 49, p. 4348, 1994.
- [5] G. Gilfoyle and K. Sherman, “Geometry update for the electromagnetic calorimeter in CLAS12,” *CLAS12 Note 2014-008*, 2014.
- [6] J. Dalton, *A New system of chemical philosophy*. London, 1808.
- [7] R. Carlitz, “On radiant matter,” *The Popular Science Monthly D*, vol. 16, 1880.
- [8] J. Thomson, “Cathode rays,” *The Electrician*, vol. 39, 1897.
- [9] E. Rutherford, *Radioactive Transformations*. Charles Shribner’s Sons, 1906.
- [10] E. Rutherford, *Radioactive Substances and their radiations*. Cambridge, 1913.
- [11] A. Einstein, “On a heuristic viewpoint concerning the production and transformation of light,” *Annalen der Physik*, vol. 322, 1905.
- [12] B. P. *et al.*, *Particles and Nuclei: An Introduction to Physical Concepts*. Springer, 2008.
- [13] F. Halzen and A. Martin, *Quarks and Leptons: An Introductory Course in Modern Particle Physics*. John Wiley and Sons, 1984.
- [14] J. Bjorken and S. Drell, *Relativistic quantum mechanics*. McGraw-Hill, 1964.
- [15] M. T. *et al.*, “Particle Data Group,” *Phys. Rev. D*, vol. 98, 2018.

- [16] M. T. *et al.*, “Baryon form factors at high Q^2 and the transition to perturbative QCD,” *Phys. Rep.*, vol. 226, 1993.
- [17] F. Close, *An Introduction to Quarks and Partons*. Academic Press, 1979.
- [18] F. Close, “ νW_2 at small ω and resonance form factors in a quark model with broken $SU(6)$,” *Phys. Lett. B*, vol. 43, p. 422, 1973.
- [19] R. Carlitz, “ $SU(6)$ symmetry breaking effects in deep inelastic scattering,” *Phys. Lett. B*, vol. 58, p. 345, 1975.
- [20] N. Isgur, “Violations of $SU(6)$ selection rules from quark hyperfine interactions,” *Phys. Rev. Lett.*, vol. 41, pp. 1269–1272, 1978.
- [21] N. Isgur, “Valence quark spin distribution functions,” *Physical Review D*, vol. 59, p. 034013, 1999.
- [22] G. Farrar and D. Jackson, “Pion and nucleon structure functions near $x = 1$,” *Phys. Rev. Lett.*, vol. 35, p. 1416, 1975.
- [23] S. B. *et al.*, “Perturbative QCD constraints on the shape of polarized quark and gluon distributions,” *Nucl. Phys. B*, vol. 441, pp. 197–214, 1995.
- [24] D. G. *et al.*, “The nuclear emc effect,” *Ann. Rev. Nucl. Part. Sci.*, vol. 45, pp. 337–390, 1995.
- [25] M. Sargsian and M. Strickman, “Model independent method for determination of the DIS structure of free neutron,” *Phys.Lett. B*, vol. 639, p. 223, 2006.
- [26] C. C. *et al.*, “Hadronization and final state interaction effects in semi-exclusive deep inelastic scattering off nuclei,” *Eur. Phys. Jour. A*, vol. 19, pp. 133–137, 2004.
- [27] D. D. *et al.*, “The Continuous Electron Beam Accelerator Facility: CEBAF at the Jefferson Laboratory,” *Annu. Rev. Nucl. Part. Sci. 2001*, vol. 51, pp. 413–450, 2001.

VITA

Nathan M Dzbenksi
Department of Physics
Old Dominion University
Norfolk, VA 23529

TODO: To be updated later!

Typeset using L^AT_EX.